UNIVERSITY OF CALIFORNIA,
IRVINE

Geometric Control Theoretical Analysis of the Nonlinear Unsteady Aerodynamics of Oscillating Wings

DISSERTATION

submitted in partial satisfaction of the requirements
for the degree of

DOCTOR OF PHILOSOPHY

in Mechanical and Aerospace Engineering

by

Laura Pla Olea

Dissertation Committee:
Associate Professor Haithem Taha, Chair
Professor Tryphon Georgiou
Professor Feng Liu

2023

TABLE OF CONTENTS

LIST OF FIGURES

LIST OF TABLES

ACKNOWLEDGMENTS

I would like to start by thanking my advisor, Professor Taha, for his guidance and support throughout these years. He built the foundations of this work and guided me through the many difficulties prevalent in research work. He not only provided me with academic advice and financial support but was also mindful of my professional goals, supporting me in the preparation of my future career.

I am especially grateful to Pete Balsells, the Balsells Fellowship program, and its director, Professor Roger Rangel. They gave me the opportunity to pursue my graduate studies at UCI, an experience that greatly contributed to my academic, professional, and personal growth. I would not be here without their support.

I would like to thank my labmates Nabil Khalifa, Dipan Deb, and Abdelrahman Elmaradny for their help and for making the long working hous more enjoyable with the their company.

To my friends in California, thank you for sharing this experience with me and making me feel at home. Anna Gonzàlez, thank you for keeping me sane and always being there for me. Noelia Cívico, Olga Movilla, Jose Santamaría, Martí Sala, Brandon Esquivias, Edu Mariño, thank you for accompaning me in different parts of this journey. Justin Mulvey, Esther Cookson, and the rest of the climbing group, thank you for being so welcoming. Dr. Andrés Adam, words cannot express how grateful I am for your support. Thank you for being there through the highs and lows.

To my friends back home, Zaruhi Matinyan, Sara Rodríguez, thank you for showing me that some friendships are not affected by distance.

My deepest gratitude goes to my parents for their unconditional support. Thank you for the long videocalls. Thank you for encouraging me to take all the opportunities. Thank you for believing in me, even when I did not.

Finally, I would like to acknowledge the support of the MAE department through fellowships and the William and Ida Melucci Space Exploration and Technology Endowment, and the funding of the Air Force Office of Scientific Research under award number FA9550-19-1-0126, monitored by Dr. Gregg Abate.

VITA

Laura Pla Olea

EDUCATION

Ph.D. in Mechanical and Aerospace Engineering **2023**
University of California, Irvine *Irvine, California, USA*

M.S. in Mechanical and Aerospace Engineering **2019**
University of California, Irvine *Irvine, California, USA*

M.S. in Aeronautical Engineering **2019**
Polytechnic University of Catalonia *Terrassa, Catalonia, Spain*

B.S. in Aerospace Technology Engineering **2017**
Polytechnic University of Catalonia *Terrassa, Catalonia, Spain*

RESEARCH EXPERIENCE

Graduate Student Researcher **2019–2023**
University of California, Irvine *Irvine, California, USA*

TEACHING EXPERIENCE

Teaching Assistant **2020–2023**
MAE 135: Compressible Flow S2023
MAE 130A: Introduction to Fluid Mechanics W2021, F2022
MAE 130B: Introduction to Viscous and Compressible Flows S2020, S2021, W2022
MAE 198: Senior Design Projects F2020
University of California, Irvine *Irvine, California, USA*

WORK EXPERIENCE

Flight Physics Engineering Intern **March 2022–September 2022**
Kittyhawk *Palo Alto, California, USA*

Applied Aerodynamics Intern **June 2023–September 2023**
Zipline *South San Francisco, California, USA*

NOMENCLATURE

Roman symbols

$a_{\perp_{1/2}}$	Normal acceleration at the mid-point
$\hat{a}$	Distance between the pitching axis and the half-chord point normalized by the chord
A_α	Pitching amplitude
b	Airfoil semi-chord
$C(k)$	Theodorsen function
C_C	Chord force coefficient
C_D	Lift coefficient
$C_{D,s}$	Lift coefficient in steady conditions
C_L	Lift coefficient
$C_{L,s}$	Lift coefficient in steady conditions
C_N	Normal force coefficient
C_{N_α}	Slope of the linear regime of the steady normal force coefficient curve
C_v	Vortex strength
$\mathcal{D}$	Drag force
F_S	Suction force
f''	Effective separation point
$\boldsymbol{f}$	Drift vector field
$\boldsymbol{g}_j$	Control vector field
H	Plunging amplitude normalized by the semi-chord
$\dot{h}$	Plunging velocity
k	Reduced frequency
k_{hf}	High-frequency gain
k_S	Suction force parameter
$k_{\dot{\alpha}}$	Rotational coefficient, $k_{\dot{\alpha}} = 4\pi\,(3/4 - \hat{a})$
L	Lift force
m_v	Virtual mass
M	Mach number
q	Non-dimensional pitch rate, $q = 2\dot{\alpha}b/U$
Re	Reynolds number
t	Time
U_j	Amplitude of oscillation of the control input
u_j	Control input
U	Free stream velocity
v	Velocity
W	Wagner function
$\boldsymbol{x}$	state vector
x_0	Quasi-steady point of separation
x_s	Point of separation
$\boldsymbol{y}$	Output

Greek symbols

α	Angle of attack
α_E	Equivalent angle of attack
α_{eff}	Kinematic effective angle of attack, $\alpha_{eff} = \alpha + \arctan\left(\dot{h}/U\right)$
β	Compressibility factor, $\beta = \sqrt{1 - M^2}$
Γ_0	Quasi-steady lift coefficient
ϵ	Small parameter
η	Empirical parameter modeling the viscous effects
ρ	Density
σ	Amplitude of the surging motion normalized by the mean free stream velocity
τ	Non-dimensional time
χ_T	Thrust control parameter
ω	Frequency

Subscripts

$(\cdot)_0$	Quasi-steady
$(\cdot)_C$	Circulatory
$(\cdot)_h$	Plunging
$(\cdot)_{NC}$	Non-circulatory
$(\cdot)_U$	Surging
$(\cdot)_v$	Viscous
$(\cdot)_\alpha$	Pitching

Superscripts

$(\cdot)^f$	Trailing edge separation
$(\cdot)^C$	Circulatory
$(\cdot)^{NC}$	Non-circulatory
$(\cdot)^p$	Attached flow
$(\cdot)^v$	Vortex
$\bar{x}$	Average of x
x^*	Equilibrium point of x

Acronyms

FWMAV	Flapping-wing micro air vehicles
LESP	Leading-edge suction parameter
LEV	Leading-edge vortex
ROM	Reduced-order model

ABSTRACT OF THE DISSERTATION

Geometric Control Theoretical Analysis of the Nonlinear Unsteady Aerodynamics of Oscillating Wings

By

Laura Pla Olea

Doctor of Philosophy in Mechanical and Aerospace Engineering

University of California, Irvine, 2023

Associate Professor Haithem Taha, Chair

More than a million species, including insects, birds and bats, rely on flapping wings to fly. Despite being one of the most common modes of transportation in the animal kingdom, flapping flight has long been an enigma for fluid dynamicists. The complex air motion around moving wings generates an unsteady flow characterized by nonlinear interactions and intricate flow structures. The complexity of these dynamics does not permit an analytical distillation of the physical processes occurring in unsteady flows and, consequently, does not provide a means to predict the flight conditions in which interesting unsteady phenomena may occur. The lack of an analytical systematic method to predict and inspect the characteristics of these higher-order effects may be attributed to a scarcity of tools capable of analyzing nonlinear systems.

Geometric control theory is defined as the application of differential geometry to the study of nonlinear control systems. Its capability to analyze higher-order effects allows for the study of the nonlinear interactions between the inputs of a system, which may lead to symmetry breaking or the generation of motion in an unactuated direction. The present work introduces the potential of geometric control theory in the analysis of unsteady flows, providing a framework for the systematic discovery of nonlinear unsteady phenomena.

This study focuses on the analysis of the mean aerodynamic forces on a wing performing harmonic pitching, plunging, and surging oscillations. The present research introduces a state-space formulation for the aerodynamics of a pitching-plunging-surging wing, which is sufficiently rich to capture the main physical aspects of the flow but efficient and compact to permit an analytical study using gefometric control theory. A combination of averaging and geometric control tools are applied to the dynamical model to derive analytical expressions for the mean aerodynamic forces on the oscillating wing. These average unsteady forces are then compared to their steady couterparts to identify any force generation mechanisms that may appear due to symmetry breaking. Further analysis reveals flight regimes with lift enhancement and drag reduction/thrust generation mechanisms as a product of the unsteady motion.

The same problem is also pursued using a more complex, well-established reduced-order model. The Beddoes-Leishman model for dynamic stall is a condensed state-space model capable of capturing the unsteady aerodynamic forces on an oscillating airfoil, including the contributions of the leading-edge vortex dynamics. Being in a state-space form makes it suitable for a geometric control analysis. The application of the averaging theorem in a geometric control framework permits an analytical study of the averaged dynamics of the unsteady forces. Similarly, the results uncover flight regimes presenting force generation mechanisms leading to lift enhancement and drag reduction.

Chapter 1

Introduction

1.1 Motivation

Researchers have long been interested in reproducing the flight capabilities of insects and birds. Their maneuverability, efficiency, and hovering ability prompted the birth of bio-inspired flapping-wing micro air vehicles (FWMAVs), miniature drones that try to replicate the flight performance of insects using flapping wings [25, 58]. The need for robust, agile aircraft capable of executing sharp course variations over a broad range of speeds prompted several design concepts, such as the MicroBat developed by the California Institute of Technology [63], the dragonfly-inspired DelFly of the Delft University of Technology [19], Harvard's robot fly [45], AeroVironment's Nano Hummingbird [31], or the Quadflapper at the University of California, Irvine [33]. These recent developments in flapping vehicles demonstrate the potential of exploiting the complex dynamics of unsteady flows. However, the continuous development of such designs necessitates a tool capable of (i) explaining the force generation mechanisms behind unsteady regimes, and (ii) predicting the flight conditions at which these phenomena occur.

The onset of classical unsteady aerodynamics formulation may be attributed to Wagner [94], who, in 1925, characterized the time-response of the lift force experienced by a flat plate impulsively started from rest at low angles of attack. A decade later, Theodorsen [88] provided an analytical solution in the frequency domain for the lift and aerodynamic moment of a harmonically pitching and plunging airfoil. The efforts that succeeded in the following years, such as those of Von Kármán and Sears [93], Küssner [34], and Schwarz [72], expanded on Theodorsen's work, focusing on the frequency response of the lift force in harmonically oscillating airfoils. Similarly, in the 1930s, Garrick [20] proposed a model for the thrust force generated by an oscillating airfoil based on Theodorsen's approach. These eminent classical theories, though restricted to small angles of attack, provide valuable insight on the contributions to the unsteady aerodynamic forces, such as the effect of the bound circulation, the wake vortices and the added mass. However, they rely on complex mathematics and do not permit an analytical scrutiny of the equations to predict the flight conditions leading to force generation.

More compact models appeared as a product of the research efforts in aeroelasticity and flight dynamic stability, which saw the need for unsteady aerodynamic representations that could be coupled with structural and control models. Prominent finite-dimensional approximations of unsteady forces are those of Jones [29], Jones [30], Leishman and Nguyen [40], and Peters [59]. Developed under the assumption of small perturbations, the aforementioned models are linear and, therefore, unsuitable for the prediction of the higher-order effects in unsteady flows when the disturbances around the mean flow exceed the small perturbation approximation.

Although not as common as linear representations, there are nonlinear models in the literature developed for the analysis of the dynamics of unsteady flows at high angles of attack. The most prominent ones being the Beddoes-Leishman model for dynamic stall [37–39], which represents the unsteady forces and aerodynamic moment on a two-dimensional airfoil

undergoing dynamic stall, and the Goman-Khrabrov state-space representation of forces and moments on aircraft performing unsteady maneuvers [22].

Despite these theoretical studies, it is in experimental efforts where the richness of unsteady flows becomes palpable. In the 1960s throughout the 1980s, studies in dynamic stall recorded an increment in the lift force when an airfoil performed a dynamic maneuver near stall [12, 23, 35, 47, 49, 66]. Recent computational and experimental work focused on the flow structures inducing lift enhancement, such as the leading-edge vortex (LEV) and the wake behind the airfoil [3, 15–17, 65, 66, 91, 92]. On the other hand, experimental studies in oscillatory airfoils unveiled the symmetry breaking phenomenon. When oscillating an airfoil, the lift and drag forces are also oscillatory in nature, and intuition infers that the average of these forces may correspond to the same forces registered at the mean angle of oscillation. However, plenty of examples in the literature report an increment or reduction in the aerodynamic forces when an airfoil is oscillated past a certain frequency [17, 20, 24, 41, 65–67], uncovering a force generation mechanism breaking the expected symmetry in forces. Such phenomenon has been recorded in non-aerodynamic applications as well, for instance, in Loumes' impedance pump [44], in which zero-mean transverse oscillations of an elastic tube generate a net flow rate. Nonetheless, a relevant example in the literature is the study of a plunging flat rectangular wing in a still fluid performed by Vandenberghe *et al.* [89]. When the wing oscillated past a threshold frequency, the rectangular plate spontaneously moved forward, revealing the existence of a thrust generation mechanism.

Therefore, the fluid dynamics community has, so far, relied on experimental observations to uncover the rich dynamical behaviors of unsteady aerodynamics. This abundance in experimental work contrasts with the lack of theoretical efforts to provide a foundation for the systematic discovery of these unintuitive force generation mechanisms. Such scarcity in analytical models may be attributed to the lack of appropriate analysis tools. Unsteady regimes are defined by higher-order flow interactions, and a theoretical study of these mechanisms

requires a mathematical tool that does not neglect the nonlinear processes occurring in the flow. The present study introduces geometric control theory as a potential tool to reconcile the imbalance between theoretical and experimental work, providing a framework for the analysis and discovery of known and yet-to-be-known unsteady phenomena.

Geometric control theory was first developed in the 1970s, when Brockett [6–9] and Sussmann [73–75] combined differential geometry and control theory. Seeking a method to study nonlinear dynamical systems evolving on *manifolds* or curvy spaces, Brockett and Sussmann referred to the mathematical formulation of differential geometry and, especially, Lie algebra [5]. Instead of neglecting higher-order effects, geometric control theory thrives on nonlinearities, analyzing the nonlinear interactions occurring within a system that may lead to the generation of forces in unactuated directions or symmetry breaking. The versatility of such a theory becomes apparent in its broad range of application, from motion planning and control in robotics [11, 51, 52], to spacecraft attitude control and stabilization [18, 70, 95, 96], to airplane maneuverability near stall [26, 28, 79] and more recently, to bio-inspired flight [27, 50, 80, 86, 87].

The nonlinear nature of geometric control theory hints at its suitability as an analysis tool of the higher-order effects witnessed in unsteady flows. Moreover, its analytical nature permits the development of a heuristic framework for the systematic analysis and discovery of the rich phenomena behind unsteady aerodynamics. However, to the author's knowledge, our efforts were the first to apply such theory to fluid mechanics [60, 61, 76, 81].

1.2 Research objectives

The main objective of this study is to show the potential of geometric control theory as a heuristic approach to (i) systematically discover force generation mechanisms in unsteady

flows and (ii) discern the physical processes behind them. To do so, the present work focuses on the application of such theory in the prediction of the average aerodynamic forces on a harmonically pitching-plunging wing.

The utilization of geometric control theory requires the reformulation of the oscillating wing as a reduced-order model (ROM) in the form of a control system. Thus, the first objective of this study is the development of an analytical ROM that is (i) rich enough to capture the main physics of the flow, including higher-order effects, and (ii) efficient and compact to permit an analytical study of the results in a geometric control framework. The goal of this ROM is not the reconstruction of the entire flow field around the airfoil, but the dynamics of some outputs of interest, in this case, the lift and drag forces.

The model is then analyzed using a combination of the averaging theorem and geometric control theory to find a qualitative expression for the mean lift and drag forces, and the point of separation. This reformulation of the averaging theorem in a geometric control framework ensures that the nonlinear effects of zero-mean oscillations are not neglected in the averaging process. The equations for the mean lift, drag, and point of separation are compared to their steady counterparts to uncover the possible enhancement or reduction of the mentioned variables due to symmetry breaking. The expressions are further analyzed to dissect the causes behind the observed force generation mechanisms. Such observations may provide an understanding of the conditions leading to symmetry breaking and serve as the foundation for the prediction of these nonlinear processes.

Therefore, this work is of analytical nature, with no interest in the obtainment of the quantitative mean values of the lift and drag forces and the point of separation. The aim of this study is the identification of trends in the flow that may lead to force generation mechanisms, which can then be further scrutinized with experimental observations or computational simulations.

As a further demonstration of the potential of geometric control theory as a systematic tool for the discovery of force generation mechanisms in fluid systems, the aforementioned averaging analysis is likewise applied to a more another complex problem: dynamic stall. To do so, this study focuses on the well-established ROM of Beddoes and Leishman [4, 38, 39]. The Beddoes-Leishman model for dynamic stall presents characteristics similar to the previous model, making it amenable to geometric control theory: it captures the unsteady higher-order aerodynamic effects of dynamic stall in a compact form. The analysis of the mean lift and drag forces using the Beddoes-Leishman model presents a contrasting insight on the effect of symmetry breaking at larger amplitudes of oscillation.

Finally, the study ends with an analysis of the effect of a surging harmonic motion on a wing. The previously derived ROM is modified to include the effect of the surging motion, along with the pitching and plunging oscillations. The averaging analysis determines the average lift force of a wing performing these three oscillatory motions. The results reveal force generation mechanisms of different nature than those observed for the pitching and plunging motions.

1.3 Thesis overview

The following thesis is structured in six different chapters

- **Chapter 1** outlines the motivation and objectives of the work.
- **Chapter 2** introduces the foundations of unsteady aerodynamics through the classical theories of Theodorsen and Wagner. The same chapter follows with the introduction of two different ROMs, starting with the derivation of a new ROM for a pitching and plunging wing and ending with an overview of the Beddoes-Leishman model for dynamic stall.

- **Chapter 3** briefly describes the analytical tools of geometric control theory used in the following chapters.

- **Chapter 4** shows the application of averaging and geometric control theory to the previously developed ROM. The analysis follows with the calculation of the mean lift and drag forces and point of separation.

- **Chapter 5** implements the aforementioned averaging analysis to the Beddoes-Leishman model to characterize the mean lift and drag forces.

- **Chapter 6** reformulates the developed ROM to include the effect of the surging motion on the oscillating wing and studies its influence on the mean lift force.

- **Chapter 7** summarizes the work presented in the study and offers suggestions on future work.

Chapter 2

Unsteady aerodynamics

The present chapter introduces the two main classical aerodynamics theories. Theodorsen and Wagner built the foundations of unsteady aerodynamics, greatly influencing the theories in unsteady flows that followed. In this section, Theodorsen's [88] classical theory is introduced first, following his derivation of the lift force experienced by an oscillating airfoil in the frequency domain. The chapter continues with Wagner's [94] pivotal work, presenting the time-evolution of the lift force on an impulsively started airfoil.

Following the derivation of these mathematically complex theories, the chapter introduces two reduced-order models (ROMs) studying the same problem of an oscillating wing. The chapter presents the development of a new ROM that is rich enough to capture the main nonlinearities of unsteady flows while sufficiently compact to permit an analytical study of the results in a geometric control framework. Such model is designed for wings oscillating at low amplitudes and flying at low Reynolds numbers.

The last section of the chapter presents the Beddoes-Leishman model for dynamic stall. This ROM is more complex than the previously introduced model and focuses on the dynamic stall phenomenon. As such, the model places great importance on the processes leading to

dynamic stall, especially, on the modeling and effects of the leading-edge vortex (LEV).

2.1 Theodorsen

In 1935, Theodor Theodorsen published his work on the frequency response of the lift force of an oscillatory wing . His ground-breaking study, became the starting point of many unsteady aerodynamics theories that followed, such as those of von Kármán and Sears [93], Küssner [34], and Schwarz [72].

Theodorsen studied the aerodynamic forces on a wing with three degrees of freedom: pitching, plunging, and aileron flapping [88]. In his formulation, Theodorsen considered non-stationary potential flow and small oscillations about the position of equilibrium. Likewise, Theodorsen approximated the wake behind the airfoil to be in the direction of the free stream velocity, neglecting any deformation with time. Making use of the no-penetration boundary condition, the Kutta condition, and Kelvin's theorem of conservation of circulation, Theodorsen described the lift response of the airfoil under harmonic motion.

In his derivation of the velocity potentials describing the flow around the airfoil, Theodorsen separated the contributions to the unsteady lift in two classes

- Non-circulatory lift: Determined by the instantaneous acceleration of the airfoil, the non-circulatory lift does not generate any net circulation.
- Circulatory lift: Similar to the lift force described in steady aerodynamics, the circulatory lift accounts for the bounded circulation of the airfoil. However, in unsteady flows, the wake induces a surface of discontinuity behind the airfoil that contributes to the circulatory lift.

The sections that follow provide a further explanation of both contributions to the lift force

as well as a thorough derivation of the described forces.

2.1.1 Non-circulatory lift

In classical potential theory, the calculation of forces on an airfoil is usually attained by replacing the mentioned airfoil with vortices, which generate the circulation needed to induce lift. As the name suggests, the non-circulatory lift requires flow singularities that do not generate circulation. Hence, in this case, the airfoil is modeled as a set of sources and sinks.

To simplify the problem, the complex geometry of the wing is approximated to a flat plate of chord $c = 2b$. As previously mentioned, the flat plate has three degrees of freedom: pitching motion, plunging motion, and aileron flapping. Given the focus of this work on the pitching and plunging motions, the following derivation does not consider the flapping aileron. Fig. 2.1a shows a scheme of the problem.

The resolution of the potential flow around the airfoil proceeds by making use of conformal mapping, employing the Joukowsky transform to replace the airfoil by a cylinder of diameter $2b$, as shown in Fig. 2.1b. In this transformation, the original airfoil is defined in the complex z-plane, in which the coordinates are defined as $z = x + iy$. After the application of the Joukowsky transform, the airfoil becomes a cylinder in the ξ-plane, where $\xi = \chi + i\eta$. The following calculations are performed in the ξ-plane.

As previously mentioned, in potential flow, solids are defined as a series of singularities, such as vortices, sources, or sinks. Since the derivation of the non-circulatory lift cannot have circulation-generating vortices, the present analysis relies on sources and sinks. As indicated in Fig. 2.1b, a source of strength q is positioned on the surface of the cylinder at (χ_1, η_1), and a sink of strength $-q$ is likewise placed at the cylinder surface at $(\chi_1, -\eta_1)$. However, the strengths $q(\varphi)$ of the source and the sink are a function of their angular position φ. As

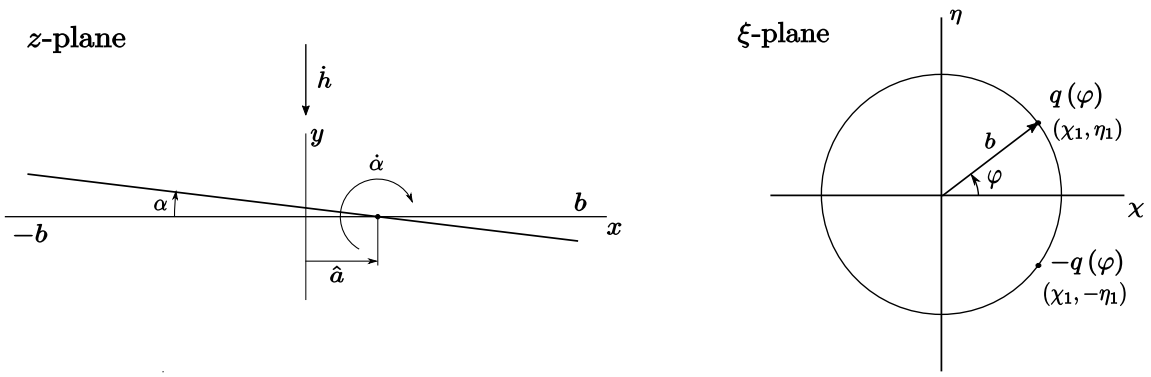

(a) Parameters of a pitching-plunging airfoil in the complex z-plane.

(b) Conformal representation of the airfoil by a cylinder in the ξ-plane.

Figure 2.1: Transformation of a flat plate in the z-plane into a circle in the ξ-plane [60].

such, the complex potential $F_{NC}(\xi, \varphi)$ of a source-sink pair located at an angular position $(\varphi, -\varphi)$ is

$$F_{NC}(\xi,\varphi) = \frac{q(\varphi)\frac{b}{2}d\varphi}{2\pi}\left[\ln\left(\xi - \frac{b}{2}\mathrm{e}^{i\varphi}\right) - \ln\left(\xi - \frac{b}{2}\mathrm{e}^{-i\varphi}\right)\right] \tag{2.1}$$

The complex velocity generated by the source-sink pair at a point located at $\xi = \chi + i\eta$ is

$$\bar{w}_{NC}(\xi,\varphi) = \frac{dF_{NC}}{d\xi} = \frac{q(\varphi)\frac{b}{2}d\varphi}{2\pi}\left[\frac{1}{\xi - \frac{b}{2}\mathrm{e}^{i\varphi}} - \frac{1}{\xi - \frac{b}{2}\mathrm{e}^{-i\varphi}}\right] \tag{2.2}$$

The complicated equation of the complex velocity is simplified using polar coordinates, such that $\xi = r\mathrm{e}^{i\theta}$. After some mathematical manipulations

$$\bar{w}_{NC}(r,\theta,\varphi) = \frac{q(\varphi)\frac{b^2}{4}d\varphi}{2\pi}\mathrm{e}^{-i\theta}\frac{2i\sin\varphi}{r^2\mathrm{e}^{i\theta} - \frac{b}{2}r2\cos\varphi + \frac{b^2}{4}\mathrm{e}^{-i\theta}} = \mathrm{e}^{-i\theta}\left(v_r - iv_\theta\right) \tag{2.3}$$

where r is the distance of the point of study from the origin of coordinates, and θ is the angle of this point with respect to the χ axis.

The equation can be further simplified by defining the real and imaginary parts of the denominator as $R(\theta,\varphi) = r^2 + \frac{b^2}{4}\cos\theta - br\cos\varphi$ and $I(\theta) = \left(r^2 - \frac{b^2}{4}\right)\sin\theta$, respectively.

With this new interpretation, the normal and tangential velocities are obtained with the definition $\bar{w}_{NC} = \mathrm{e}^{-i\theta}(v_r - iv_\theta)$. The normal and tangential velocities generated by the source-sink pair at a point located at a distance r from the origin with an angle θ are

$$v_{\theta_{NC}}(r,\theta,\varphi) = -\frac{q(\varphi)\frac{b^2}{4}\sin\varphi R(\theta,\varphi)d\varphi}{\pi\left(R^2+I^2\right)} \tag{2.4}$$

$$v_{r_{NC}}(r,\theta,\varphi) = \frac{q(\varphi)\frac{b^2}{4}\sin\varphi I(\theta,\varphi)d\varphi}{\pi\left(R^2+I^2\right)} \tag{2.5}$$

The derived velocities are those generated by a source of strength $q(\varphi)$ located at (χ_1, η_1) and a sink of strength $-q(\varphi)$ placed at $(\chi_1, -\eta_1)$. Nonetheless, this source-sink pair does not define a cylinder in potential flow. Since the airfoil and the cylinder are continuous surfaces, they cannot be described using a single source and a sink. Instead, the definition of a continuous surface in potential flow requires a continuous distribution of singularities. In this case, the upper half of the cylinder is constructed using a distribution of sources and the lower half with a distribution of sinks. In this case, the complex velocities generated by this distribution of sources and sinks are the integral of Eq. (2.4) and Eq. (2.4) over the whole cylinder, with $\varphi \in [0, \pi]$

$$v_{\theta_{NC}}(\theta) = -\frac{1}{2\pi}\int_0^\pi \frac{q(\varphi)\sin\varphi d\varphi}{\cos\theta - \cos\varphi} \tag{2.6}$$

$$v_{r_{NC}}(\theta) = \frac{q(\theta)}{2} \tag{2.7}$$

During this mathematical derivation, the source strength distribution $q(\varphi)$ has remained

undefined. The no-penetration boundary condition is applied to the cylinder surface to find the value of $q(\phi)$. The no-penetration boundary condition states that the normal velocity of the flow on the surface of the cylinder has to be equal to the normal velocity of the cylinder wall, or $v_\perp = v_{motion}$. In other words, the flow cannot permeate the surface of the cylinder.

Since the airfoil is performing pitching and plunging oscillations, as seen in Fig. 2.1a, the velocity at the airfoil surface is

$$v_{motion}(x) = -U\sin\alpha - \dot{h}\cos\alpha - \dot{\alpha}\,(\hat{x} - \hat{a}) \tag{2.8}$$

where U is the free stream velocity, α the angle of attack, $\dot{h}$ the plunging velocity, $\hat{x}$ the position of the point of interest normalized by the chord and $\hat{a}$ the position of the pitching axis with respect to the airfoil midpoint. Applying the no-penetration boundary condition, the source distribution is found

$$q(\theta) = 2v_{r_{NC}} = 4v_{motion}(\theta)\sin\theta = 4\left[-U\sin\alpha - \dot{h}\cos\alpha - \dot{\alpha}\,(b\cos\theta - a)\right]\sin\theta \tag{2.9}$$

Inserting Eq. (2.9) into Eq. (2.6), the tangential velocity at the cylinder surface is obtained

$$v_{\theta_{NC}}(\theta) = 2\left[\left(U\sin\alpha + \dot{h}\cos\alpha - \dot{\alpha}\hat{a}\right)\cos\theta + \frac{\dot{\alpha}b}{4}\cos(2\theta)\right] \tag{2.10}$$

Since, in potential flow, the tangential and radial velocities are derived from a potential

$$\begin{aligned} v_\theta &= \frac{1}{r}\frac{\partial\phi}{\partial\theta} \\ v_r &= \frac{\partial\phi}{\partial r} \end{aligned} \tag{2.11}$$

the potential of the cylinder is calculated from Eq. (2.10) to be

$$\phi_{NC}(\theta) = -\frac{b}{2}\int_0^{\pi} v_{\theta_{NC}}(\varphi)d\varphi = b\left[\left(U\sin\alpha + \dot{h}\cos\alpha - \dot{\alpha}\hat{a}\right)\sin\theta + \frac{\dot{\alpha}b}{4}\sin(2\theta)\right] \quad (2.12)$$

Knowing the non-circulatory potential of the cylinder, the unsteady Bernoulli equation is applied to find the pressure at the cylinder surface

$$p - p_{\infty} = -\rho\left[U_{\infty}\frac{\partial\phi}{\partial x} + \frac{\partial\phi}{\partial t}\right] \quad (2.13)$$

where p is the pressure, p_{∞} the pressure of the free stream, and ρ the density of the flow. Therefore, the integration of this pressure field due to non-circulatory contributions provides the expression of the non-circulatory lift

$$l_{NC} = 2\rho\left[\int_{-\frac{b}{2}}^{\frac{b}{2}}\frac{\partial\phi}{\partial t}dx + U_{\infty}\left(\phi_{TE} - \phi_{LE}\right)\right] \quad (2.14)$$

where ϕ_{TE} and ϕ_{LE} are the velocity potentials at the trailing edge and the leading edge respectively. Assuming small perturbations and the velocity potential at the trailing edge to be equal to zero, and substituting the values of the velocity potentials in Eq. (2.12) to Eq. (2.14), the non-circulatory lift is obtained

$$l_{NC} = \pi\rho b^2\left(U\dot{\alpha} + \ddot{h} - \ddot{\alpha}\hat{a}\right) \quad (2.15)$$

which can be further simplified to

$$l_{NC}(t) = -m_v a_{\perp_{1/2}}(t) \quad (2.16)$$

The non-circulatory lift is proportional to the instantaneous acceleration of the airfoil at the midpoint. This acceleration is multiplied by the term $m_v = \pi\rho b^2$, known as the added or

virtual mass, and is equivalent to the mass of a cylinder of air of radius b. Therefore, the non-circulatory lift represents the force required to accelerate the flow around the airfoil. In vacuum, the force required to move the airfoil is equal to its mass times its acceleration. However, when the airfoil is surrounded by air, the force needed to move the airfoil is bigger because it is not only necessary to accelerate the structure but also to accelerate the mass of air around it. The non-circulatory lift is this extra force needed to accelerate the added mass of air.

Eq. (2.16) also reveals the instantaneous nature of the force. Given its algebraic definition, the non-circulatory lift does not present any lag. Any motion of the airfoil will instantaneously lead to a variation in the non-circulatory lift; the force will not require any time to accommodate to the changes in the airfoil motion.

2.1.2 Circulatory lift

The second contribution to the lift force is the circulatory lift. This force is similar to the lift defined in steady aerodynamics, which accounts for the circulation that builds around the airfoil. However, under unsteady conditions, the circulatory lift also includes the effect of the wake behind the airfoil. This section describes the impact of the addition of vortices to the distribution of sources and sinks defined in the previous section to characterize the cylinder. The following calculations are also performed on the cylinder in the ξ-plane.

To account for the circulation effects in the airfoil, a vortex of strength Γ is added behind the cylinder to model the wake of the airfoil. To satisfy Kelvin's theorem of the conservation of circulation, another vortex of strength $-\Gamma$ is added, bounded to the cylinder. However, the addition of these singularities changes the distribution of velocities in the flow, which may disrupt the no-penetration boundary condition. To ensure the normal velocity at the cylinder surface is still equal to its motion, the positions of the bounded and wake vortices

need to satisfy the condition

$$d = \frac{b^2}{4X} \tag{2.17}$$

where d and X are the locations of the bounded and wake vortices, respectively, with respect to the center of the cylinder. Fig. 2.2 shows a schematic of the positions of the bounded and wake vortices.

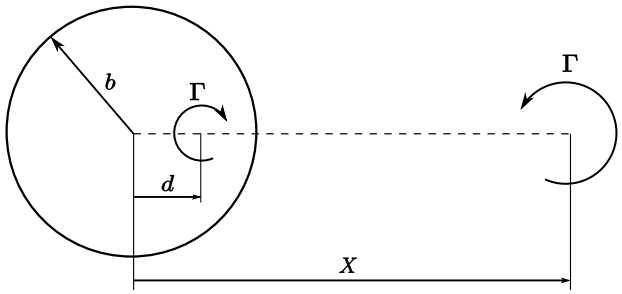

Figure 2.2: Location of the bounded and wake vortex [60].

Having determined the location of the vortices, their strength can be found with the application of the Kutta condition. In other words, the tangential velocity at the trailing edge of the cylinder has to be equal to zero or, equivalently, the tangential velocity due to circulatory effects and the tangential velocity due to non-circulatory effects have to be equal in magnitude but of opposite sign

$$v_{\theta_{NC}}(\theta = 0) + v_{\theta_C}(\theta = 0) = 0 \tag{2.18}$$

To calculate the tangential velocity due to the vortices, it is necessary to define the complex potential of a vortex located at $(d, 0)$ combined with a vortex at $(X, 0)$

$$F_C = \frac{\Gamma}{2\pi i}\left[\ln(\xi - X) - \ln(\xi - d)\right] \tag{2.19}$$

and, following the derivation of the previous section, the tangential velocity due to the

circulation is obtained

$$v_{\theta_C}(\theta) = -\frac{\Gamma}{b\pi}\frac{X^2 - \frac{b^2}{4}}{X^2 + \frac{b^2}{4} - bX\cos\theta} \tag{2.20}$$

The combination of the tangential velocities in Eq. (2.6) and Eq. (2.20) with the Kutta condition in Eq. (2.18) gives an equation for the circulation distribution of the wake. The transformation of this equation from the cylinder domain to the airfoil domain using the Joukowsky transformation $z = \xi + \frac{b^2}{\xi}$ leads to the equation

$$-2v_{3/4} - \frac{1}{\pi b}\int_b^\infty \gamma_w(z,t)\sqrt{\frac{z+b}{z-b}}dz = 0 \tag{2.21}$$

where $v_{3/4}$ is the velocity at the three-quarter chord point, and γ_w is the unknown vortex distribution of the wake. Similar to the case of the sources and the sinks, the surface discontinuity of the wake is not represented by a single vortex but by a continuous distribution of vortices extending from b, the airfoil trailing edge, to ∞. The upper limit of the integral is set to infinity to account for the accumulated effects of the wake over time. Eq. (2.21) is obtained under the assumption that the wake is in the direction of the free stream and does not deform over time [88]. The validity of this assumption generates discussion among the community.

Under the small angle approximation $\alpha_{3/4} = -\frac{v_{3/4}}{U}$, Eq. (2.21) can be expressed as a function of the angle of attack at the three-quarter point $\alpha_{3/4}$. Such arrangement leads to Wagner's equation [94]

$$\int_b^\infty \gamma_w(z,t)\sqrt{\frac{z+b}{z-b}}dz = 2\pi\alpha_{3/4}(t)Ub = \Gamma_0(t) \tag{2.22}$$

where Γ_0 is the quasi-steady circulation of the airfoil, which is defined as the value that the circulation would take if it developed instantaneously. In other words, Γ_0 is the value of the

circulation in steady conditions evaluated at the flight conditions at time t.

As previously shown in the derivation of the non-circulatory lift, the integration of the tangential velocity in Eq. (2.20) results in the velocity potential of the circulatory flow

$$\phi_c(\theta) = \frac{\Gamma}{\pi}\left[\frac{\pi}{2} - \arctan\left(\sqrt{\frac{z+b}{z-b}}\sqrt{\frac{1-\cos\theta}{1+\cos\theta}}\right)\right] \tag{2.23}$$

which, in combination with the unsteady Bernoulli equation of Eq. 2.13, leads to the calculation of the circulatory lift

$$l_C(t) = \rho\int_b^\infty \frac{\gamma_w(z,t)z}{\sqrt{z^2-b^2}}dz \tag{2.24}$$

Given the similitude between Wagner's equation for the quasi-steady circulation (Eq. (2.22)) and the expression of the circulatory lift in Eq. (2.24), the latter is multiplied and divided by Γ_0 in the following way

$$l_C(t) = l_C(t)\frac{\Gamma_0}{\Gamma_0} = \rho U\Gamma_0(t)\frac{\int_b^\infty \frac{\gamma_w(z,t)z}{\sqrt{z^2-b^2}}dz}{\int_b^\infty \gamma_w(z,t)\sqrt{\frac{z+b}{z-b}}dz} = l_0(t)\frac{\int_b^\infty \frac{\gamma_w(z,t)z}{\sqrt{z^2-b^2}}dz}{\int_b^\infty \gamma_w(z,t)\sqrt{\frac{z+b}{z-b}}dz} \tag{2.25}$$

where l_0 is the quasi-steady lift, the lift coefficient under static conditions, given by the Kutta-Joukowsky theorem as

$$l_0 = \rho U\Gamma_0 \tag{2.26}$$

Due to the unknown vortex distribution of the wake γ_w, Eq. (2.25) does not have a general analytical solution. Nonetheless, the circulatory lift can be resolved for certain cases, such as harmonic oscillations [88]. For a pitching motion, the angle of attack at the three-quarter

code takes the form

$$\alpha_{3/4} = \bar{\alpha} \mathrm{e}^{i\omega t} \tag{2.27}$$

where ω is the frequency of oscillation. The assumption of a non-deforming wake parallel to the free stream implies that a harmonic motion of the angle of attack translates to a harmonic motion with the same frequency for the vortex distribution of the wake

$$\gamma_w(z,t) = \overline{\gamma_w(z)} \mathrm{e}^{i\omega t} \tag{2.28}$$

Therefore, combining the harmonic motion of Eq. (2.28) with the definition of the circulatory lift in Eq. (2.25), one obtains the equation of the circulatory lift derived by Theodorsen [88]

$$l_C(t) = l_0(t) C\left(k\right) \tag{2.29}$$

where $C\left(k\right)$ is the Theodorsen function, which depends on the reduced frequency $k = \frac{\omega b}{U}$. $C(k)$ is defined using Hankel functions of the second kind of order n, $H_n^{(2)}$, or modified Bessel functions of second kind of order n, K_n

$$C(k) = \frac{H_1^{(2)}(k)}{H_1^{(2)}(k) + jH_0^{(2)}(k)} = \frac{K_1(jk)}{K_1(jk) + K_0(jk)} \tag{2.30}$$

Therefore, according to Eq. (2.29), the circulatory lift of a wing following a sinusoidal motion with small amplitude, is equal to the quasi-steady lift L_0 multiplied by a modulation function $C(k)$ [88]. The Theodorsen function attenuates the lift response as a function of the reduced frequency, as pictured in Fig. 2.3a. In the steady case, $C(k)$ is real and equal to unity, but its value decreases with the reduced frequency. For high values of k, the magnitude of the

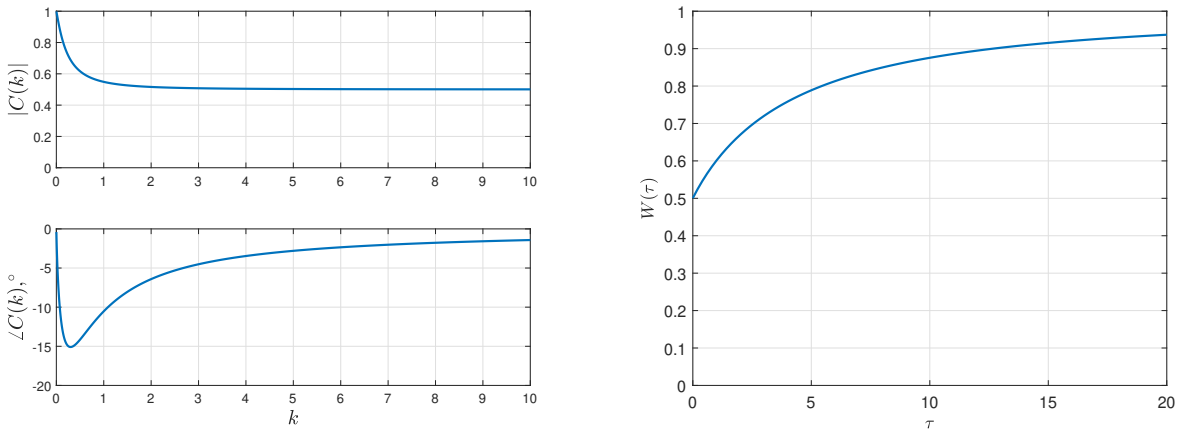

(a) Theodorsen function.

(b) Wagner function.

Figure 2.3: Magnitude and phase of the frequency response (Theodorsen) function and step response (Wagner) function of the circulatory lift.

Theodorsen function is $\|C(k)\| = 1/2$. Thus, a change in the angle of attack prompts an instantaneous lift force equal to half of its steady value. This rapid generation of force does not correspond to the behavior of physical systems, revealing a limitation in Theodorsen's work [82, 84].

2.2 Wagner

A decade before Theodorsen published his theory, Wagner [94] solved the time response of the lift force on a flat plate due to a step change in the angle of attack or in the free stream. This section derives Wagner's work from the results of Theodorsen. This derivation is different from that in Wagner's original work, but provides a better understanding of the connection between Theodorsen and Wagner's work.

The Theodorsen function provides the unsteady lift under harmonic motion, but the theory presents some constraints. First, the results are in the frequency domain, giving only the steady state response of the lift. Therefore, the steady state of the lift force remains unsolved.

Second, Theodorsen's theory is limited to harmonic motion. Both of these limitations may be addressed by resolving the lift response in the time domain.

In a flat problem under pitching motion, similar to the one in Fig. 2.1a, the angle of attack is a function of time $\alpha(t)$. The calculation of the circulatory lift using Theodorsen's Eq. (2.29) requires a frequency-domain representation of $\alpha_{3/4}(t)$, obtained with the application of the Fourier transform

$$\alpha_{3/4}(\omega) = \int_{-\infty}^{\infty} \alpha_{3/4}(t) \mathrm{e}^{-i\omega t} dt \tag{2.31}$$

Once the frequency response of the angle of attack is known, the circulatory lift is calculated using Theodorsen's equation (Eq. (2.29))

$$l_C(\omega) = \rho U^2 b 2\pi \alpha_{3/4}(\omega) C\left(k\right) \tag{2.32}$$

The inverse Fourier transform of Eq. (2.32) results in the time-domain response of the circulatory lift

$$l_C(t) = \frac{1}{2\pi} \int_{-\infty}^{\infty} l_C(\omega) \mathrm{e}^{i\omega t} d\omega \tag{2.33}$$

Up to this point, $\alpha_{3/4}(t)$ has remained an undefined function of time. However, to solve Wagner's problem of the lift response in a flat plate due to a step change, $\alpha_{3/4}(t)$ needs to be defined in the following way

$$\alpha_{3/4}(t) = \begin{cases} \alpha & t \geq 0 \\ 0 & t < 0 \end{cases} \tag{2.34}$$

The Fourier transform of the angle of attack at the three-quarter point reveals the expression

in the frequency domain

$$\alpha_{3/4}(\omega) = \frac{\alpha}{i\omega} \tag{2.35}$$

The insertion of Eq. (2.35) into the equation for the circulatory lift in Eq. (2.33) uncovers the time-response of the circulatory lift generated on a flat plate due to a step change in the angle of attack

$$l_C(t) = \rho U^2 b 2\pi\alpha \frac{1}{2\pi} \int_{-\infty}^{\infty} \frac{C\,(k)}{k} dk = l_0 \int_{-\infty}^{\infty} \frac{C\,(k)}{k} dk \tag{2.36}$$

or, in a simplified manner

$$l_C(t) = l_0 W\,(\tau) \tag{2.37}$$

where $W(\tau)$ is the Wagner function, expressed as a function of the non-dimensional time $\tau = \frac{Ut}{b}$ and represented in Fig. 2.3b. The comparison of Eq. (2.37) with Theodorsen's in Eq. (2.29) reveals that both, Wagner and Theodorsen, define the unsteady circulatory lift as the multiplication of the quasi-steady lift by a modulation function: the Theodorsen function in the frequency domain, and the Wagner function in the time domain. In fact, both functions constitute a Fourier pair [21].

Wagner's function accounts for the lag between the step change in angle of attack and the time at which the lift reaches the corresponding steady lift value at that angle of attack. That is, a change in the angle of attack does not instantaneously generate a lift force equivalent to its steady value at that angle of attack. The lift needs some time to build up to its final steady value. Wagner's function describes the dynamics of this transient response. However, as shown in Fig. 2.3b, Wagner's function presents the same non-physical behavior observed in Theodorsen's: a step change in the angle of attack instantaneously prompts a

force equivalent to half of the steady lift.

Unlike Theodorsen's, Wagner's function does not have an analytical expression. The function, as Wagner defined it, is characterized by the integral [94]

$$W(\tau) = \int_0^\tau \mu(\sigma) \frac{1 + \tau - \sigma}{\sqrt{(1 + \tau - \sigma)^2 - 1}} d\sigma \tag{2.38}$$

where μ is governed by the equation

$$\int_0^\tau \mu(\sigma) \sqrt{\frac{2 + \tau - \sigma}{\tau - \sigma}} d\sigma = 1 \tag{2.39}$$

The lack of an analytical expression complicates the use of Wagner's equation. Such complexity prompted the apparition of several approximations, the most common ones defining $W(\tau)$ with exponential functions. Some prevailing approximations are those of Jones [29] and Jones [30], which define Wagner's function as

$$W(\tau) = 1 - A_1 \exp(-b_1 \tau) - A_2 \exp(-b_2 \tau) \tag{2.40}$$

where the values of the constants A_1, A_2, b_1, and b_2 are listed in Table 2.1.

	A_1	A_2	b_1	b_2
Jones [29]	0.165	0.335	0.0455	0.3
Jones [30]	0.165	0.335	0.041	0.32

Table 2.1: Constants defining the exponential approximations of the Wagner function.

2.3 Reduced-order modeling of the unsteady aerodynamics

The classical unsteady aerodynamics theories presented in the previous sections rely on complex mathematical formulation, making the calculation of unsteady aerodynamic loads lengthy and tedious. In contrast, ROMs offer an approximation to the resolution of the unsteady forces in a compact form. This section presents the derivation of a ROM for a pitching and plunging wing oscillating at low Reynolds numbers, starting with a definition of the problem to be formulated, followed by its derivation. The developed model is later analyzed in a geometric control framework in Chapter 4.

2.3.1 Problem statement

The application of geometric control theory requires the formulation of an oscillating wing as an efficient dynamical system [84]. In other words, this control theory necessitates a system that is rich enough to capture the main physics of the system, including the nonlinearities within unsteady flows, but at the same time compact to permit an analytical distillation of the results. As such, one of the main objectives of this work is the development of a ROM capable of predicting the unsteady forces on an oscillating wing in a form that is amenable to geometric control theory.

The purpose of this section is the derivation of a ROM describing the unsteady forces in a pitching-plunging wing in a constant free stream U, as seen in Figure 2.4. The pitching angle α is defined positive when pitching up, and the plunging displacement h is positive in the downward direction.

In other words, this study seeks to find a physics-based control system in the form of a

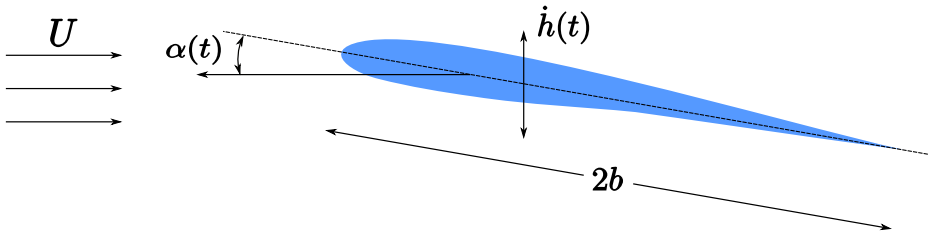

Figure 2.4: Schematic diagram of a pitching-plunging airfoil in a free stream [81].

nonlinear state-space model, such as the one in Eq. (3.1), representing the dynamics of the unsteady lift and drag forces and separation point over the wing. Given the compactness of the model, the purpose of the ROM is not a reconstruction of the flow field around the wing, but a derivation of the dynamics of the lift force $\mathcal{L}(t)$, drag force $\mathcal{D}(t)$, and separation point $x_S(t)$.

The ROM is derived to take the following form

$$\begin{aligned} \dot{\boldsymbol{x}}(t) &= \boldsymbol{f}(\boldsymbol{x}(t)) + \boldsymbol{g}_\alpha(\boldsymbol{x}(t))\ddot{\alpha}(t) + \boldsymbol{g}_h(\boldsymbol{x}(t))\ddot{h}(t) \\ \boldsymbol{y}(t) &= [L(t) \quad \mathcal{D}(t) \quad x_s(t)]^T \end{aligned} \tag{2.41}$$

where $\boldsymbol{x}$ is the vector that contains all the states of the system, and $\boldsymbol{y}$ is the vector of output variables; in this case, the lift, drag and point of separation. The vectors $\boldsymbol{g}_\alpha$ and $\boldsymbol{g}_h$ are the control vector fields associated with the pitching and plunging inputs.

The control inputs of the system are $\ddot{\alpha}$ and $\ddot{h}$, the pitching and plunging accelerations, respectively. The definition of a proper dynamical system requires the model to avoid any direct dependence on the derivatives of the inputs. Therefore, since the aerodynamic forces depend on the velocities and accelerations, the accelerations are chosen to be the inputs of the system. If the inputs of the system were the position or velocities, the dynamical equations would depend on the derivatives of those inputs, preventing the formulation of a proper dynamical system.

2.3.2 State-space model for the unsteady aerodynamics

The ROM developed in this section is based on the state-space model formulated by Taha *et al.* [77] to compute the unsteady lift of a pitching wing. The model is also derived in [60, 81].

Circulatory lift dynamics

The first step in the development of a state-space model for the unsteady aerodynamic forces is the derivation of the lift dynamics. To do so, the model refers to the definition of the circulatory lift according proposed in the classical theory of Wagner [94], as derived in Section 2.2

$$L_C(\tau) = L_0 W(\tau) = \rho U^2(\tau) b C_{L,s} W(\tau) = 2\pi\rho U^2(\tau) b \alpha(\tau) W(\tau) \tag{2.42}$$

where W is the Wagner function, which depends on the non-dimensional time τ

$$\tau = \frac{2}{c}\int_0^t U(s)ds \tag{2.43}$$

Note that this definition of the non-dimensional time accounts for a time-varying $U(t)$. Although the problem presented in Section 2.3.1 concerns a wing in a constant free stream, the following derivation of the circulatory lift accounts for a time-varying free stream to present a general formulation for a ROM valid for any arbitrary wing motion. However, the assumption of a constant free stream is applied at the end of the derivation to obtain a ROM suitable for the problem defined in Section 2.3.1.

Eq. (2.42) is the solution of the circulatory lift due to a step change in the angle of attack. However, this work is interested in the derivation of a ROM capable of capturing the dynam-

ics of the unsteady forces for different types of pitching and plunging motions, without being restricted to step functions. As such, the Duhamel principle is applied to Wagner's equation to extend the lift response to an arbitrary input. Thus, the circulatory lift is the superposition of the indicial time response on the first instant of motion and the time-variation of the input variable [77]

$$L_C(\tau) = 2\pi\rho U^2(\tau) b \left(\alpha(0) W(\tau) + \int_0^\tau \frac{d\alpha(0)}{d\tau} W(\tau - \sigma) d\sigma \right) \tag{2.44}$$

The input variable in Eq. (2.44) is the angle of attack α. However, Wagner's function represents the indicial response due to a step change in the angle of attack but also to other aerodynamic inputs, such as the velocity of the wing. Therefore, the equation could be defined with any other input. According to potential flow theory, lift appears due to the circulation, and moreover, lift is linearly dependent on the circulation. Hence, the present model relies on the quasi-steady circulation Γ_0 as the input of the system defining the circulatory lift [77]

$$L_C(\tau) = 2\pi\rho U^2(\tau) b \left(\Gamma_0(0) W(\tau) + \int_0^\tau \frac{d\Gamma_0(0)}{d\tau} W(\tau - \sigma) d\sigma \right) \tag{2.45}$$

The quasi-steady circulation is defined as the static value of the circulation at any time instant. Given the nature of the pitching motion, in this study the circulations accounts for the translational and rotational effects of the wing in the form

$$\Gamma_0(t) = U(t) b C_{L,s}(\alpha(t)) + b^2 k_{\dot{\alpha}} \dot{\alpha}(t) \tag{2.46}$$

where $k_{\dot{\alpha}} = 4\pi \left(\frac{3}{4} - \hat{a} \right)$ is a coefficient depending on the location of the pitching axis normalized by the chord $\hat{a}$ and measured from the center of the wing. As presented in Eq. (2.46), the quasi-steady circulation depends on the curve of the steady lift coefficient $C_{L,s}$. However, no assumptions are made in the form of the steady lift coefficient; $C_{L,s}$ represents

an arbitrary static $C_L - \alpha$ curve defined by the user. Therefore, $C_{L,s}$ can take any desired form, from the conventional linear lift coefficient $2\pi\alpha$ to any nonlinear function derived from theoretical analyses, numerical, or experimental data.

Given the lack of an analytical expression for the Wagner function, the manipulation of Eq. (2.45) is not trivial. However, as described in Section 2.2, Jones [29] and Jones [30] approximated the Wagner function with an exponential representation

$$W(\tau) = 1 - A_1 \exp(-b_1\tau) - A_2 \exp(-b_2\tau) \tag{2.47}$$

where A_1, A_2, b_1, and b_2 are constants determined by Jones [29] and Jones [30].

Reformulating Eq. (2.45) with the dimensional time t

$$L_C(t) = \rho U(t) \left(\Gamma_0(0) W(t) + \int_0^t \frac{d\Gamma_0(s)}{d\tau} W(t-s) ds \right) \tag{2.48}$$

and integrating the second term by parts, the following expression is obtained

$$\begin{aligned} L_C(t) &= \rho U(t) \left(\Gamma_0(0) W(t) + \Gamma_0(t) W(t-t) - \Gamma_0(0) W(t-0) - \int_0^t \Gamma_0(s) \frac{dW(t-s)}{ds} ds \right) \\ &= \rho U(t) \left(\Gamma_0(t) W(0) - \int_0^t \Gamma_0(s) \frac{dW(t-s)}{ds} ds \right) = \rho U(t) \Gamma_{eff} \end{aligned} \tag{2.49}$$

where the inclusion of Jones approximation of the Wagner function (Eq. (2.47)) leads to the derivative

$$\begin{aligned} &\frac{dW(t-s)}{ds} = \frac{dW(\tau-\sigma)}{d\sigma} \left(\frac{d\sigma}{ds} \right) \\ &= -\left[A_1 b_1 \exp\left(-b_1(\tau-\sigma)\right) + A_2 b_2 \exp\left(-b_2(\tau-\sigma)\right) \right] \left(\frac{U(s)}{b} \right) \\ &\quad = -\frac{U(s)}{b} \left[A_1 b_1 \exp\left(-\frac{b_1}{b} \int_s^t U(s) ds \right) + A_2 b_2 \exp\left(-\frac{b_2}{b} \int_s^t U(s) ds \right) \right] \end{aligned} \tag{2.50}$$

or in a more compact form, with summation on the repeated indices

$$\frac{dW(t-s)}{ds} = -A_i \frac{b_i}{b} U(s) \exp\left(-\frac{b_i}{b}\int_s^t U(s)ds\right), \quad i = 1,2 \tag{2.51}$$

Consequently, the effective circulation Γ_{eff} of Eq. (2.49) is given by

$$\Gamma_{eff}(t) = (1 - A_1 - A_2)\Gamma_0(t) + x_i(t), \quad i = 1,2 \tag{2.52}$$

where the states are the solutions of the nonlinear differential equation

$$\dot{x}_i = \frac{b_i U(t)}{b}(-x_i(t) + A_i\Gamma_0(t)), \qquad i = 1,2 \tag{2.53}$$

with the initial condition $x_i(0) = 0$. Therefore, as shown in Eq. (2.53), the circulatory lift can be obtained through the resolution of a two-state dynamical system in which the quasi-steady circulation is the input. The number of states comes from the two-pole approximation of the Wagner function given by Eq. (2.47). However, if a more accurate approximation is to be used, the number of states will increase. Therefore, the number of states is completely arbitrary, and the system in Eq. (2.53) can be generalized to include any number of states. Hence, the dynamics of the circulatory lift are given by

$$\begin{aligned} \dot{\boldsymbol{x}}_C(t) &= [\boldsymbol{A}]_{nxn} U(t) \boldsymbol{x}_c(t) + [\boldsymbol{B}]_{nx1} U(t)\Gamma_0(t) \\ L_C(t) &= \rho U(t)\left([\boldsymbol{C}]_{1xn}\boldsymbol{x}_c(t) + [D]_{1x1}\Gamma_0(t)\right) \end{aligned} \tag{2.54}$$

where $\boldsymbol{x}_c \in \mathbb{R}^n$ represents all the internal aerodynamic states that model the lift dynamics, and the matrices $\boldsymbol{A}$, $\boldsymbol{B}$ and $\boldsymbol{C}$ depend on the characteristics of the wing and the flow. The parameter $D = k_{hf}$ is the high-frequency gain of the system (the magnitude of the output at infinite frequency, the instantaneous response of the system), and the quasi-steady circulation Γ_0 is the input of the system.

For a constant free stream, such as the problem of study, U can be absorbed into matrices $\boldsymbol{A}$ and $\boldsymbol{B}$, leading to the system

$$\begin{aligned} \dot{\boldsymbol{x}}_C(t) &= [\boldsymbol{A'}]_{nxn}\boldsymbol{x}_c(t) + [\boldsymbol{B'}]_{nx1}\Gamma_0(t) \\ L_C(t) &= \rho U(t)\left([\boldsymbol{C}]_{1xn}\boldsymbol{x}_c(t) + [D]_{1x1}\Gamma_0(t)\right) \end{aligned} \tag{2.55}$$

Non-circulatory lift dynamics

As derived in section 2.1 (Eq. (2.16)), the non-circulatory lift is the multiplication of the virtual mass times the normal acceleration at the half-chord point. Nonetheless, Theodorsen's derivation only applies to small angles of attack. To account for higher α's, the following formulation is needed

$$L_{NC} = -m_v a_{\perp_{1/2}}(t)\cos\alpha(t) \tag{2.56}$$

where $m_v = \rho\pi b^2$ is the virtual mass, and the normal acceleration for a pitching-plunging wing is

$$a_{\perp_{1/2}}(t) = \frac{d}{dt}\left(U(t)\sin\alpha(t) + \dot{h}(t)\cos\alpha(t) - \hat{a}b\dot{\alpha}(t)\right)$$

where $\hat{a}b$ is the distance between the hinge location and the half-chord point. Eq. (2.56) indicates a direct dependence between the lift (output of the system) and the accelerations (input). Nonetheless, it is preferable for the output to only depend on the states $\boldsymbol{x}$ and not on the inputs. Moreover, Taha and Rezaei [83] found that viscosity induces a phase lag between the normal acceleration and the non-circulatory lift. As such, the effect of viscosity

can be modeled into the system through the state x_v

$$\begin{aligned} \dot{x}_v(t) &= -\frac{x_v(t)}{\tau_v} + \frac{a_{\perp_{1/2}}(t)}{\tau_v} \\ L_{NC}(t) &= m_v x_v(t) \cos\alpha(t) \end{aligned} \tag{2.57}$$

where τ_v is the time constant governing the dynamics of the non-circulatory lift. These dynamics only appear when viscosity is taken into account, causing a phase lag in the generation of non-circulatory lift. Eq. (2.57) is not necessary when considering potential flow.

Drag dynamics

Aside from the lift force, another interesting variable in flow phenomena is the drag force. The pressure drag is given by

$$\mathcal{D}(t) = L(t)\tan\alpha(t) - F_S(t) \tag{2.58}$$

where $L = L_C + L_{NC}$ is the total lift force, and F_S is the suction force. The first component of the drag is the projection of the resultant force N (when there is no leading-edge suction) in the direction parallel to the flow. In fact, without leading-edge suction, the lift and drag forces are given by $N\cos\alpha$ and $N\sin\alpha$ respectively.

The second contribution is the suction force derived by Garrick [20]

$$F_S(t) = 2\pi\rho b\left[v_{3/4}(t)C(k) - \frac{b}{2}\dot{\alpha}(t)\right]^2 \tag{2.59}$$

where $v_{3/4}$ is the normal velocity at the three-quarter chord point and $C(k)$ is the Theodorsen function in terms of the reduced frequency k. The suction force is always positive, and since its contribution to the drag force is negative (Eq. (2.58)), it decreases the drag force. As

such, the suction force points to a possible reduction in the drag force due to unsteady motion.

As seen in Eq. (2.59), the suction force depends on the Theodorsen function and, therefore, on the circulatory lift dynamics. This dependence is further evident when after the following algebraic manipulation. The quasi-steady speed at the three-quarter chord point can be expressed through the quasi-steady circulation as $v_{3/4} = \Gamma_0/(2\pi b)$. Therefore, the unsteady three-quarter chord point velocity $v_{3/4}C(k)$ can be replaced by the dynamics of the unsteady Γ_0

$$F_S(t) = k_S \rho b \left[\frac{\boldsymbol{C}\boldsymbol{x}_c(t) + D\Gamma_0(t)}{2\pi b} - \frac{b}{2}\dot{\alpha}(t) \right]^2 \tag{2.60}$$

where k_S is a parameter of the suction force that depends on the conditions of the flow. For potential flow, $k_S = 2\pi$, as seen in Garrick's Eq. (2.59).

Separation point dynamics

In ideal conditions, the flow is constantly attached to the wing surface and leaves the wing smoothly at the trailing edge. In real viscous flows, as the angle of attack increases, the flow separates from the top surface, creating a low pressure region behind it [2]. Consequently, when separation occurs, there is a high increase in the drag force and a reduction in lift. Hence, the prediction of the separation phenomenon is of high interest to aerodynamicists.

In steady flows, there are several approaches to define the location of the separation point. Given the velocity profile around the wing, Thwaites [**?**] computes the point of separation through a series of integral expressions. However, this model is not applicable in this case because the velocity profile is unknown. Another well-known model is Kirchhoff's, in which

the lift coefficient changes as a function of the point of separation

$$C_{L,s}(\alpha) = 2\pi \sin\alpha \left(\frac{1+\sqrt{x_0}}{2}\right)^2 \tag{2.61}$$

where x_0 is the location of the separation point under steady conditions normalized by the chord, and $2\pi \sin\alpha$ is the theoretical expression of the lift curve when there is no separation. Therefore, if the static lift coefficient is known for a certain angle of attack, the position of the separation point can be determined from Eq. (2.61).

For unsteady flows, the separation point is calculated with the state-space model developed by Goman and Khrabrov [22] for a pitching wing. The unsteady effects are the result of two phenomena. The first one accounts for the quasi-steady effects, such as the delay of the circulation or the convection of the boundary layer. This delay is assumed to be proportional to the rate of variation of the angle of attack $\dot{\alpha}$. As such, the quasi-steady variation of the separation point is modeled as an argument shift $x_0\left(\alpha - \tau_2\dot{\alpha}\right)$, with τ_2 being the time-delay constant.

The second effect comes from the transient aerodynamics that cannot be defined as quasi-steady. This group includes the disturbances in the flow that occur without a change in the angle of attack. These disturbances cause a build up from the conditions before the perturbation to the steady state conditions after the perturbation. It is modeled as a first order lag with the relaxation constant τ_1. Thus, the dynamics of the unsteady point of separation are

$$\dot{x_s}(t) = -\frac{x_s(t)}{\tau_1} + \frac{x_0\left(\alpha(t) - \tau_2\dot{\alpha}(t)\right)}{\tau_1} \tag{2.62}$$

Final state-space model

The model derived above works for a two-dimensional pitching wing in a time-varying free stream. However, the problem of study is the representation of a pitching and plunging wing in a constant free stream. As such, the following equations neglect any time dependence in U. On the other hand, the application of the model to a pitching-plunging wing requires any dependence on the angle of attack α to be replaced by the effective angle of attack $\alpha_{eff} = \alpha + \arctan\frac{\dot{h}}{U}$ to account for the plunging motion. Thus, the quasi-steady circulation of Eq. (2.46) becomes

$$\Gamma_0(\alpha, \dot{\alpha}, \dot{h}) = UbC_{L,s}\left(\alpha(t) + \arctan\frac{\dot{h}(t)}{U}\right) + b^2 k_{\dot{\alpha}}\dot{\alpha}(t) \tag{2.63}$$

Eq. (2.63) is introduced in the final model, obtained with the combination of the equations derived in the previous sections. As a result, the ROM for a pitching-plunging wing in a constant free stream is given by

$$\frac{d}{dt}\begin{pmatrix} \boldsymbol{x}_c \\ x_v \\ x_s \\ \alpha \\ \dot{\alpha} \\ \dot{h} \end{pmatrix} = \begin{pmatrix} \boldsymbol{A}\boldsymbol{x}_c + \boldsymbol{B}\Gamma_0\left(\alpha, \dot{\alpha}, \dot{h}\right) \\ -\frac{1}{\tau_v}\left[x_v + \left(U\cos\alpha - \dot{h}\sin\alpha\right)\dot{\alpha}\right] \\ -\frac{1}{\tau_1}\left[x_s - x_0\left(\alpha + \arctan\frac{\dot{h}}{U} - \tau_2\dot{\alpha}\right)\right] \\ \dot{\alpha} \\ 0 \\ 0 \end{pmatrix} + \begin{pmatrix} \mathbf{0}_{nx1} \\ \frac{ab}{\tau_v} \\ 0 \\ 0 \\ 1 \\ 0 \end{pmatrix} u_\alpha + \begin{pmatrix} \mathbf{0}_{nx1} \\ \frac{\cos\alpha}{\tau_v} \\ 0 \\ 0 \\ 0 \\ 1 \end{pmatrix} u_h \tag{2.64}$$

where $\boldsymbol{x} = \left[\boldsymbol{x}_c, x_v, x_s, \alpha, \dot{\alpha}, \dot{h}\right]$ is the state vector of dimension $n+5$, the vector containing all the internal states of the system. The inputs are $u_\alpha = \ddot{\alpha}$ and $u_h = \ddot{h}$, the pitching and plunging accelerations, respectively. The outputs of the system are the lift force, the drag

force, and the location of the point of separation, which are written as follows

$$\begin{aligned} L(t) &= \rho U \left(\boldsymbol{C}\boldsymbol{x}_c(t) + D\Gamma_0 \left(\alpha, \dot{\alpha}, \dot{h} \right) \right) \\ D(t) &= L(t) \tan \alpha(t) - k_s \rho b \left(\frac{\boldsymbol{C}\boldsymbol{x}_c(t) + D\Gamma_0(t)}{2\pi b} - \frac{b}{2}\dot{\alpha}(t) \right)^2 \\ x_s(t) &= x_s(t) \end{aligned} \tag{2.65}$$

2.4 Beddoes-Leishman model for dynamic stall

The ROM derived in Section 2.3.2 proves the efficacy of a compact form in the description of the dynamics of unsteady flows. Nonetheless, the model serves as a general representation of the unsteady aerodynamics problem and is not applicable to the study of specific phenomena such as dynamic stall. In fact, the ROM of the previous section is capable of capturing the effects of the standing LEV appearing in pitching wings at low Reynolds numbers. However, in dynamic stall, the LEV separates from the leading edge, convecting downstream along the airfoil and detaching from the wing as it reaches the trailing edge. Such effect, essential in the description of the dynamic stall phenomenon, is not captured by the model in Section 2.3.2. Therefore, the present section provides a description of the Beddoes-Leishman model [37–39], a ROM focused on modeling the processes undergone by an airfoil experimenting dynamic stall, including the LEV and its effect on the aerodynamic forces.

In the 1980s, Beddoes and Leishman derived a ROM to calculate the loads on the blades of a helicopter rotor under dynamic stall. The Beddoes-Leishman model [37–39] reproduces the dynamical behavior of a two-dimensional airfoil pitching about the quarter-chord point and undergoing dynamic stall using state-space formulation. Given the motion of the airfoil, this ROM predicts the unsteady lift and drag forces and pitching moment experienced by the airfoil. The model consists of a set of first order ordinary differential equations (ODE's) divided in four different subsystems, each of them representing a distinct aspect of the unsteady flow

behavior. The model describes the dynamic stall phenomenon as the combination of four different features: (i) attached flow, (ii) dynamic stall onset, (iii) trailing edge separation, and (iv) vortex induced dynamic stall. The combination of these subsystems, which are related in a nonlinear way such that the input of one block is the output of the previous one, characterizes the lift and drag coefficients, and moment coefficient experienced by the airfoil.

2.4.1 Attached flow

The first aspect of the flow described by the Beddoes-Leishman model is the unsteady aerodynamic response under attached flow conditions. To do so, the model refers to the Jones [29] and Jones [30] state-space approximation of Wagner's theory [94], which formulates the indicial response for the unsteady circulatory lift (Section 2.2). However, given the compressibility effects present in the rotor aircraft studied by Beddoes and Leishman, Wagner's solution is generalized in terms of the Mach number [37–39]. Similarly, the indicial response for the non-circulatory lift is obtained from piston theory. The combination of these resulting indicial functions is used to describe the attached flow response, given by the state-space system

$$\dot{\boldsymbol{x}}_{1\to4} = \boldsymbol{A}\boldsymbol{x}_{1\to4} + \boldsymbol{B}\begin{Bmatrix} \alpha_{eff} \\ \\ q \end{Bmatrix} \tag{2.66}$$

$$C_N^p = \boldsymbol{C}\boldsymbol{x}_{1\to4} + \boldsymbol{D}\begin{Bmatrix} \alpha_{eff} \\ \\ q \end{Bmatrix} \tag{2.67}$$

where $\boldsymbol{x}_{1\to4}$ is the vector that contains the first four states of the attached flow module, C_N^p is the normal force coefficient under attached flow conditions, and $q = \frac{2\dot{\alpha}b}{U}$ is the non-dimensional pitch rate. That is, the dynamical system characterizing the attached flow response (Eq. (2.66), (2.67)) consists of two inputs: the effective angle of attack α_{eff} and the pitch rate q, and one output: the normal force coefficient under attached flow conditions C_N^p. The effective angle of attack combines the contributions of the pitching angle and the plunging velocity

$$\alpha_{eff}(t) = \alpha(t) + \arctan\frac{\dot{h}(t)}{U} \tag{2.68}$$

The matrices $\boldsymbol{A}$, $\boldsymbol{B}$, $\boldsymbol{C}$, and $\boldsymbol{D}$ depend on the Mach number M and the characteristics of the airfoil as described by the equations below

$$\begin{aligned}
\boldsymbol{A} &= -\text{diag}\left[b_1\left(\frac{\beta^2 U}{b}\right), b_2\left(\frac{\beta^2 U}{b}\right), \frac{1}{K_\alpha T_I}, \frac{1}{K_q T_I}\right] \\
\boldsymbol{B} &= \begin{bmatrix} 1 & 1 & 1 & 0 \\ 0.5 & 0.5 & 0 & 1 \end{bmatrix}^T \\
\boldsymbol{C} &= \begin{bmatrix} C_{n_\alpha}\left(\frac{\beta^2 U}{b}\right) A_1 b_1 & C_{n_\alpha}\left(\frac{\beta^2 U}{b}\right) A_2 b_2 & \frac{4}{M}\left(\frac{-1}{K_\alpha T_I}\right) & \frac{1}{M}\left(\frac{-1}{K_\alpha T_I}\right) \end{bmatrix} \\
\boldsymbol{D} &= \begin{bmatrix} 4/M & 1/M \end{bmatrix}
\end{aligned} \tag{2.69}$$

where $\beta = \sqrt{1-M^2}$ is the compressibility factor, C_{N_α} is the slope of the linear regime of the normal force coefficient curve, and $T_I = 2b/V_s$, where V_s is the sound speed. The parameters K_α and K_q depend on the flight conditions

$$\begin{aligned}
K_\alpha &= \frac{\kappa_\alpha}{(1-M) + 0.5\beta^2 C_{N_\alpha} M^2 (A_1 b_1 + A_2 b_2)} \\
K_q &= \frac{\kappa_q}{(1-M) + \beta^2 C_{N_\alpha} M^2 (A_1 b_1 + A_2 b_2)}
\end{aligned} \tag{2.70}$$

Data Source	A_1	A_2	b_1	b_2	κ_α	κ_q
Boeing	0.636	0.364	0.339	0.249	0.77	0.70
ARA	0.625	0.375	0.310	0.312	1.00	1.00
NASA	0.482	0.518	0.684	0.235	0.72	0.70
Consolidated data	0.918	0.082	0.366	0.102	0.85	0.73

Table 2.2: Coefficients of derived indicial lift approximations as obtained from different data sources. Consolidated data combines the data from all the listed sources [36].

The parameters A_1, A_2, b_1, b_2, κ_α, and κ_q are constants associated with the airfoil indicial response. They are obtained from curve-fitting of experimental data, and their value may change depending on the flight conditions. Table 2.2 lists the values of the constants as obtained from different experimental data, and Table 2.3 summarizes the testing parameters of each data source. Refer to [36] for a more detailed overview.

The attached flow normal coefficient C_N^p accounts for the circulatory and non-circulatory responses of the airfoil. The circulatory component of the normal coefficient is described by the first two states, and is defined as

$$C_N^C(t) = C_{N_\alpha}\alpha_E(t) \tag{2.71}$$

where α_E is the equivalent angle of attack

$$\alpha_E(t) = \beta^2 \left(\frac{U}{b}\right)(A_1 b_1 x_1 + A_2 b_2 x_2) \tag{2.72}$$

The original formulation of the Beddoes-Leishman model [37–39] describes the attached flow with eight states. However, but states $\boldsymbol{x}_{5\to 9}$ characterize the pitching moment associated with the attached flow response. Since moment calculation is outside the scope of this study, these states have been excluded. Nonetheless, the following sections maintain the original notation of the Beddoes-Leishman model for the remaining states, creating a gap in the numbering system.

Data Source	Airfoil	M	k
Boeing	NACA 0012, NACA 23010	$0.2 - 0.6$	≤ 0.72
ARA	NACA 0012	$0.3 - 0.75$	≤ 0.25
NASA	NACA 64A010	$0.5 - 0.8$	≤ 0.3

Table 2.3: Testing parameters of the data sources [36].

2.4.2 Stall onset

One of the most critical aspects in the modeling of dynamic stall is the identification of the conditions leading to the onset of leading-edge separation. The literature includes successful criteria such as the leading-edge suction parameter (LESP) criterion, proposed by Ramesh, Gopalarathnam and their colleagues [53, 64, 68]. In contrast to the LESP criterion, in the Beddoes-Leishman model, leading-edge separation occurs at the attainment of a critical leading-edge pressure. Since the leading-edge pressure and the normal force coefficient are related, the criterion is implemented by defining a critical normal force coefficient C_{N_1} instead, which corresponds to the critical pressure for separation onset [38]. In other words, instead of modeling the leading-edge pressure and verifying if it surpasses a critical value, we implement the condition such that there is no separation as long as the normal force coefficient is lower than C_{N_1}. However, in unsteady conditions there is a lag in C_N with respect to the motion of the wing. Similarly, there is a lag in the leading-edge pressure response with respect to the normal force coefficient. These dynamics are represented with a first-order lag given by the state x_9

$$\dot{x}_9 = -\frac{x_9}{T_P} + \frac{C_N^p(t)}{T_P} \tag{2.73}$$

$$C_N'(t) = x_9 \tag{2.74}$$

where the Mach-dependent time constant T_P is determined empirically. The input of the system is the attached normal force coefficient C_N^p, which exemplifies the recursive structure of the Beddoes-Leishman model, where the output of one differential equation is the input of the next one.

The output coefficient $C'_N(t)$ represents a substitute value on which to apply the dynamic stall criterion. The flow remains attached for $C'_N(t) < C_{N_1}$, and leading-edge separation is initiated when $C'_N(t)$ exceeds C_{N_1}.

2.4.3 Trailing edge separation

The effect of trailing edge separation on the aerodynamic force coefficients is modeled using Kirchhoff's theory [38, 39]

$$C_N = C_{N_\alpha} \left(\frac{1 + \sqrt{x_0}}{2} \right)^2 \alpha \tag{2.75}$$

where $x_0 \in [0, 1]$ is the separation point normalized by the chord, where $x_0 \simeq 0$ indicates fully separated flow and $x \simeq 1$ implies separation near the trailing edge. The variation of the separation point with the angle of attack is modeled modeled with the empirical relation [38]

$$x_0 = \begin{cases} 1 - 0.3 \exp\left(\frac{\alpha - \alpha_1}{S1}\right) & \text{if } \alpha < \alpha_1 \\ 0.04 + 0.66 \exp\left(\frac{\alpha_1 - \alpha}{S2}\right) & \text{if } \alpha > \alpha_1 \end{cases} \tag{2.76}$$

where α_1 is the angle at which the location of the separation point is $x_0 = 0.7$, and S_1 and S_2 are empiric constants that define the stall characteristic.

In the Beddoes-Leishman model, the lag in trailing edge separation is modeled assuming a first order lag in trailing edge separation

$$\dot{x}_{10} = -\frac{x_{10}}{T_f} + \frac{x_0\left(\frac{x_9}{C_{N_\alpha}}\right)}{T_f} \tag{2.77}$$

$$f''(t) = x_{10} \tag{2.78}$$

where f'' is the effective separation point, and T_f is an empirical time constant dependent on the Mach number.

The normal force coefficient due to trailing edge separation C_N^f is computed according to Kirchoff's theory in Eq. (2.75)

$$C_N^f(t) = C_{N_\alpha}\left(\frac{1+\sqrt{f''}}{2}\right)^2 \alpha_E(t) \tag{2.79}$$

Similarly, the force in the tangential direction, or chord force, is the projection of the normal force in the horizontal direction

$$C_C(t) = \eta C_{N_\alpha}\alpha_E^2\sqrt{f''} \tag{2.80}$$

Since viscous effects prevent the pressure distribution from realizing the chord force that could be obtained in potential flow, η serves as an empiric parameter, obtained from static data, that permits the modeling of viscous effects in the flow.

2.4.4 Dynamic stall

The dynamic stall phenomenon is characterized by the formation of a vortex near the leading edge of the airfoil [3, 12, 32, 47, 48, 92]. The vortex grows in size and strength until it separates from the leading edge and convects downstream over the top surface of the airfoil. According to the Beddoes-Leisman model, vortex detachment occurs when the absolute value of $C'_N(t)$ exceeds C_{N_1} [38, 39]. At this point, the non-dimensional counter τ_v is established, marching uniformly according to the non-dimensional time Ut/b while the LEV starts to grow and accumulate circulation. After a time interval T_{vl} the vortex reaches the trailing edge its contribution to the lift force vanishes.

The convection process of the leading-edge vortex is described by the differential state equations

$$\dot{x}_{11} = -\frac{x_{11}}{T_v} + \frac{\dot{C}_v}{T_v} \tag{2.81}$$

$$C_N^v(t) = x_{11} \tag{2.82}$$

where the input of the system is $\dot{C}_v$, a measure of the vortex strength. It is the rate of change of the parameter C_v, and its evolution over time is modeled as

$$C_v = \begin{cases} C_N^C \left[1 - \left(\frac{1+\sqrt{f''}}{2}\right)^2\right] & \text{for } \tau_v \leq 2T_{vl} \\ 0 \quad \text{for } \tau_v > 2T_{vl} \end{cases} \tag{2.83}$$

The output of the differential equation is the vortex contribution to the normal force coefficient $C_N^v(t)$.

2.4.5 Total aerodynamic response

The total normal force coefficient under dynamic stall conditions encompasses all the contributions listed in the previous sections. It is the sum of the normal force coefficients due to trailing edge separation, the LEV contribution, and the non-circulatory or added mass effects

$$C_N(t) = C_N^f(t) + C_N^v(t) + C_N^p(t) - C_N^C(t) \tag{2.84}$$

The lift and drag coefficients are the projection of the normal and chord force coefficients in the directions perpendicular and tangential to the flow, respectively

$$\begin{aligned} C_L(t) &= C_N(t)\cos\alpha(t) + C_C(t)\sin\alpha(t) \\ C_D(t) &= C_N(t)\sin\alpha(t) - C_C(t)\cos\alpha(t) \end{aligned} \tag{2.85}$$

Chapter 3

Geometric control theory

Geometric control theory is a mathematical theory combining differential geometry and control theory. Developed by Brockett [6–9] and Sussmann [73–75] in the 1970s, this theory was adopted in the study of dynamical systems evolving on *manifolds* or curvy spaces. The integration of differential geometry in the study of these nonlinear systems proved essential for performing calculations on these curvy spaces.

The interest in geometric control theory lies on the exploitation of nonlinear interactions within systems. The integration of higher-order effects allows for the study of unintuitive phenomena, such as the generation of motion in unactuated directions, the unconventional force generation via symmetry breaking due to high-frequency oscillatory inputs, or the stabilization of mechanical systems due to high-frequency periodic forcing (vibrational control theory).

This chapter introduces the fundamental concepts required to gain an understanding of geometric control theory and applies these concepts to the study of dynamical systems. The objective is the demonstration of the potential of geometric control theory as a tool for the analysis of nonlinear interactions within a system.

3.1 Unconventional force generation

Consider the nonlinear, finite-dimensional dynamical system

$$\dot{\boldsymbol{x}}(t) = \boldsymbol{f}\left(\boldsymbol{x}(t)\right) + \sum_{j=1}^{m} \boldsymbol{g}_j\left(\boldsymbol{x}(t)\right) u_j(t) \tag{3.1}$$

where x is a state vector evolving on an n-dimensional manifold $\mathcal{M}^n$, $\boldsymbol{f}$ is the drift vector field (uncontrolled dynamics of the system), and $\boldsymbol{g}_j$'s are the control vector fields corresponding to the control inputs u_j's. For instance, in a driftless system ($\boldsymbol{f} = \boldsymbol{0}$) we move along the vector $\boldsymbol{g}_j$ by turning off all the inputs except u_j.

However, according to geometric control theory, it is possible to generate motion in a prescribed direction, even when there is no direct actuation in that said direction. We may generate forces in that unactuated direction through the specific manipulation of our control inputs. In other words, geometric control theory gives us additional directions in which to move along. These directions are determined by *Lie bracket* operations between control vector fields. The Lie bracket between the control vector fields $\boldsymbol{g}_j$ and $\boldsymbol{g}_k$ is computed as [11]

$$\left[\boldsymbol{g}_j, \boldsymbol{g}_k\right] = \frac{\partial \boldsymbol{g}_k}{\partial \boldsymbol{x}} \boldsymbol{g}_j - \frac{\partial \boldsymbol{g}_j}{\partial \boldsymbol{x}} \boldsymbol{g}_k \tag{3.2}$$

If the resulting Lie bracket $\left[\boldsymbol{g}_j, \boldsymbol{g}_k\right]$ is linearly independent with respect to the two control vector fields that generated it $\boldsymbol{g}_j$ and $\boldsymbol{g}_k$, geometric control theory states that we can move in the new direction given by this Lie bracket. In other words, through the adequate manipulation of the control inputs u_j and u_k one can generate motion along an unactuated direction with no direct control authority. Essentially, the Lie bracket provides us with a new direction of actuation, one that cannot be obtained with linear control theory. Motion along this direction can be realized through an out-of-phase periodic signal of the control

inputs u_j and u_k [42, 43, 52].

3.2 Periodic excitation

The application of geometric control theory to averaging theory [10, 90] allows for the analysis of systems with periodic forcing. These two theories, in combination with chronological calculus [1], capture the higher-order effects characteristic of nonlinear systems that are usually neglected by direct averaging [46].

Given a system such as Eq. (3.1), for small-amplitude high-frequency oscillatory inputs $u_j = \omega U_j \cos(\omega t)$, the averaged dynamics of the system according to geometric control theory are

$$\dot{\bar{\boldsymbol{x}}} = \boldsymbol{f}\left(\bar{\boldsymbol{x}}\right) - \sum_{j,k=1}^{m} \frac{U_j U_k}{4} \langle \boldsymbol{g}_j : \boldsymbol{g}_k \rangle \left(\bar{\boldsymbol{x}}\right) \tag{3.3}$$

where the over-bar indicates an averaged quantity, and $\langle \boldsymbol{g}_j : \boldsymbol{g}_k \rangle$ is the *symmetric product* between the input vectors $\boldsymbol{g}_j$ and $\boldsymbol{g}_k$

$$\langle \boldsymbol{g}_j : \boldsymbol{g}_k \rangle = \langle \boldsymbol{g}_k : \boldsymbol{g}_j \rangle \triangleq \left[\boldsymbol{g}_j, [\boldsymbol{f}, \boldsymbol{g}_k]\right] = \left[\boldsymbol{g}_k, \left[\boldsymbol{f}, \boldsymbol{g}_j\right]\right] \tag{3.4}$$

From Eq. (3.3), we can infer the difference between the application of direct averaging and geometric control theory. Since the inputs are oscillatory, a direct application of averaging theory would have led to an averaged system in which the contribution of the inputs would have been neglected. Hence, the last term in Eq. (3.3) would be canceled. However, the inclusion of nonlinear terms leads to an additional contribution to the averaged system. Therefore, geometric control theory states that high-frequency zero-mean oscillations may modify the averaged dynamics of the system. That is, periodic inputs may lead to net

motion, and their effects are on the averaged dynamics are represented by the symmetric product.

3.3 Averaging analysis of a high-frequency, high-amplitude periodically forced nonlinear system

This section presents a generalization of the concept mentioned in the previous Section 3.2. We start with the definition of the Averaging theorem.

Theorem 3.1 (Averaging theorem)**.** *Consider the following nonlinear time periodic (NLTP) system written in averaging-canonical form [46]*

$$\dot{\boldsymbol{x}} = \epsilon \boldsymbol{X}(\boldsymbol{x}, t, \epsilon) \tag{3.5}$$

where ϵ is a small parameter such that $0 < \epsilon << 1$, and the vector field $\boldsymbol{X}$ is T-periodic in t. The averaged system corresponding to Eq. (3.5) is

$$\dot{\bar{\boldsymbol{x}}} = \epsilon \bar{\boldsymbol{X}}\left(\bar{\boldsymbol{x}}\right) \tag{3.6}$$

where $\bar{\boldsymbol{X}}\left(\bar{\boldsymbol{x}}\right) = \frac{1}{T}\int_0^T \boldsymbol{X}(\boldsymbol{x}, \tau, 0)d\tau$.

1. *If $\boldsymbol{x}(0) - \bar{\boldsymbol{x}}(0) = \mathcal{O}(\epsilon)$, then there exist $b, \epsilon^* \in \mathbb{R}^+$ such that $\boldsymbol{x}(t) - \bar{\boldsymbol{x}}(t) = \mathcal{O}(\epsilon)$ for all $t \in [0, b/\epsilon]$ and for all $\epsilon \in (0, \epsilon^*)$.*

2. *If the origin $\bar{\boldsymbol{x}} = 0$ is an exponentially stable equilibrium of system (3.5) and if $\boldsymbol{x}(0) - \bar{\boldsymbol{x}}(0) = \mathcal{O}(\epsilon)$, then there exists an ϵ^* such that $\boldsymbol{x}(t) - \bar{\boldsymbol{x}}(t) = \mathcal{O}(\epsilon)$ for all $t \geq 0$ and for all $\epsilon \in (0, \epsilon^*)$. Furthermore, system 3.5 has a unique, exponentially stable, T-periodic solution $\boldsymbol{x}_T(t)$ such that $||\boldsymbol{x}_T(t)|| \leq k\epsilon$ for some $k \in \mathbb{R}^+$.*

Assume a nonlinear system subject to high-amplitude, high-frequency periodic forcing in the form

$$\dot{\boldsymbol{x}}(t) = \boldsymbol{f}(\boldsymbol{x}(t)) + \frac{1}{\epsilon} G\left(\boldsymbol{x}(t), \frac{t}{\epsilon}\right) \tag{3.7}$$

The averaging theorem cannot be directly applied to Eq. (3.7). Since $\boldsymbol{f}$ and $\boldsymbol{G}$ are not of the same order, the system is not in the averaging-canonical form of Eq. (3.5) and the direct application of the averaging theorem could lead to incorrect results. Thus, the system necessitates a more rigorous averaging technique; the Variation of Constants (VOC) formula usually provides a remedy for this issue [46, 54–57, 69]. It allows decomposing the system (3.7), which is not directly amenable to the averaging theorem to 2 systems each of which is amenable to the form 3.5. .

Theorem 3.2. *If $\boldsymbol{G}$ is a T-periodic, zero-mean vector field, and f and G are both continuously differentiable, the averaged dynamical system corresponding to Eq. (3.7) is written as*

$$\dot{\bar{\boldsymbol{x}}}(t) = \bar{\boldsymbol{F}}\left(\bar{\boldsymbol{x}}(t)\right) \tag{3.8}$$

where $\bar{\boldsymbol{F}}\left(\bar{\boldsymbol{x}}(t)\right) = \frac{1}{T}\int_0^T \boldsymbol{F}\left(\boldsymbol{x}(t), \tau\right) d\tau$, and F is the pullback of f along the flow $\Phi_t^{\boldsymbol{G}}$ of the time-varying vector field $\boldsymbol{G}$.

With the chronological calculus formulation of Agrachev and Gamkrelidze [1, 11], for a time-invariant $\boldsymbol{f}$ and a T-periodic $\boldsymbol{G}$, the pullback can be written in terms of iterated Lie brackets of f and g as follows

$$\boldsymbol{F}\left(\boldsymbol{x}(t), t\right) = f\left(\boldsymbol{x}(t)\right) + \boldsymbol{\mathcal{G}}\left(\boldsymbol{x}(t), t\right) \tag{3.9}$$

where

$$\boldsymbol{\mathcal{G}}(\boldsymbol{x}(t),t)=\sum_{k=1}^{\infty}\int_0^t\cdots\int_0^{s_{k-1}}\left(ad_{\boldsymbol{G}(\boldsymbol{x}(t),s_k)}\ldots ad_{\boldsymbol{G}(\boldsymbol{x}(t),s_1)}\boldsymbol{f}\left(\boldsymbol{x}(t)\right)\right)ds_k ds_1 \tag{3.10}$$

where $ad_{\boldsymbol{G}}\boldsymbol{f}=[\boldsymbol{G},\boldsymbol{f}]$.

Chapter 4

Geometric control averaging of the unsteady aerodynamics

The main objective of this work is the application of geometric control theory to the study of unsteady aerodynamics. In particular, this research aims to utilize geometric control theory to uncover any force generation mechanisms that may appear on a harmonically oscillating wing.

The present chapter analyzes the reduced-order model (ROM) derived in Section 2.3.2 in a geometric control framework. The model, representing a pitching and plunging wing, is in the form of the nonlinear dynamical system in Eq. (3.1), making it amenable to geometric control theory. The analysis starts with the averaging of the system dynamics using a geometric control approach. This study leads to the derivation of analytical expressions for the average lift and drag forces and the average location of the point of separation. These mean unsteady values are compared to their steady counterparts to reveal any lift enhancement or drag reduction mechanisms that may occur on the wing due to unsteady motion. The analytical nature of the work permits a distillation of the causes behind the

unsteady generation of forces. This meticulous analysis provides an understanding of the conditions leading to symmetry breaking.

The reader is reminded of the qualitative nature of the study. This research does not provide a quantitative assessment of the unsteady forces. The objective is the prediction of regimes at which force generation mechanisms may appear. This work serves as a guide to identify trends in the flow that may induce force generation mechanisms through symmetry breaking. These trends may be later further analyzed with computational simulations or experimental work.

4.1 Problem definition

The application of geometric control theory requires the definition of the problem of study as a ROM. The model needs to be rich enough to capture the higher-order effects occurring in unsteady flows, but also compact to permit an analytical study of the results. The ROM of a pitching-plunging wing (pictured in Fig. 2.4) derived in Section 2.3.2 satisfies both characteristics. The dynamical model representing the wing takes the form derived in Eq. (2.64), repeated below for clarity

$$\frac{d}{dt}\begin{pmatrix} \boldsymbol{x}_c \\ x_v \\ x_s \\ \alpha \\ \dot{\alpha} \\ \dot{h} \end{pmatrix} = \begin{pmatrix} \boldsymbol{A}\boldsymbol{x}_c + \boldsymbol{B}\Gamma_0\left(\alpha, \dot{\alpha}, \dot{h}\right) \\ -\frac{1}{\tau_v}\left[x_v + \left(U\cos\alpha - \dot{h}\sin\alpha\right)\dot{\alpha}\right] \\ -\frac{1}{\tau_1}\left[x_s - x_0\left(\alpha + \arctan\frac{\dot{h}}{U} - \tau_2\dot{\alpha}\right)\right] \\ \dot{\alpha} \\ 0 \\ 0 \end{pmatrix} + \begin{pmatrix} \mathbf{0}_{nx1} \\ \frac{ab}{\tau_v} \\ 0 \\ 0 \\ 1 \\ 0 \end{pmatrix} u_\alpha + \begin{pmatrix} \mathbf{0}_{nx1} \\ \frac{\cos\alpha}{\tau_v} \\ 0 \\ 0 \\ 0 \\ 1 \end{pmatrix} u_h \quad (4.1)$$

where $\boldsymbol{x} = \left[\boldsymbol{x}_c, x_v, x_s, \alpha, \dot{\alpha}, \dot{h}\right]$ is the state vector of the system. The pitching and plunging accelerations $u_\alpha = \ddot{\alpha}$ and $u_h = \ddot{h}$, respectively, are the inputs of the system; the outputs of the model are the lift force, the drag force, and the location of the point of separation, described in Eq. (2.65) and repeated below for clarity

$$\begin{aligned} L(t) &= \rho U \left(\boldsymbol{C}\boldsymbol{x}_c(t) + D\Gamma_0\left(\alpha, \dot{\alpha}, \dot{h}\right)\right) \\ D(t) &= L(t)\tan\alpha(t) - k_s\rho b\left(\frac{\boldsymbol{C}\boldsymbol{x}_c(t) + D\Gamma_0(t)}{2\pi b} - \frac{b}{2}\dot{\alpha}(t)\right)^2 \\ x_s(t) &= x_s(t) \end{aligned} \tag{4.2}$$

Given the qualitative nature of the study, some of the parameters of the model are treated as bookkeeping parameters in this symbolic analysis. For example, a term that is proportional to m_v implies a contribution due to virtual or added mass effects, or a term including $C'_{L,s} = \frac{\partial C_{L,s}}{\partial \alpha}$ points to a dependence on the static curve slope. The specific values of these parameters are irrelevant to the qualitative analysis of this research.

This work focuses on the average aerodynamic forces on a wing performing zero-mean harmonic pitching and plunging oscillations. The oscillatory motion of the pitching angle α (defined as positive pitching up) and the plunging displacement h (positive downward) are defined by

$$\alpha(t) = \alpha^* - A_\alpha\cos(\omega t) \text{ and } h(t) = -Hb\cos(\omega t + \phi) \tag{4.3}$$

where α^* is the mean pitching angle, A_α the pitching amplitude, H the plunging amplitude normalized by the half-chord length, ω the frequency of oscillation, and ϕ the phase difference between both motions. Thus, the inputs of they system, the pitching and plunging accelerations, are obtained by differentiating twice the oscillations in Eq. (4.3)

$$u_\alpha = \ddot{\alpha} = \omega^2 A_\alpha\cos(\omega t) \text{ and } u_h = \ddot{h} = \omega^2 Hb\cos(\omega t + \phi) \tag{4.4}$$

This study focuses on finding the average dynamics of the unsteady lift, drag and separation point under high-frequency small-amplitude oscillations at high angles of attack in a high velocity free stream. The described conditions define the order of the main parameters in the problem

$$A_\alpha = \mathcal{O}(\epsilon), \quad H = \mathcal{O}(\epsilon), \quad \omega = \mathcal{O}\left(\frac{1}{\epsilon}\right), \quad U = \mathcal{O}\left(\frac{1}{\epsilon}\right) \quad \Rightarrow k = \frac{\omega b}{U} = \mathcal{O}(1) \tag{4.5}$$

with k being the reduced frequency and ϵ a small parameter. The order of the parameters indicates the terms that are more prevalent in the equations: terms of order ϵ^2 may be neglected with respect to terms of order ϵ.

4.2 Averaging of the unsteady aerodynamics model

The inclusion of the system inputs in Eq. (4.4) in the ROM (4.1) leads to

$$\dot{\boldsymbol{x}}(t) = \boldsymbol{f}(\boldsymbol{x}(t)) + [A_\alpha \boldsymbol{g}_\alpha(\boldsymbol{x}(t)) \cos(\omega t) + Hb\boldsymbol{g}_h(\boldsymbol{x}(t)) \cos(\omega t + \phi)] \tag{4.6}$$

which, with the scaling of the parameters defined in Eq. (4.5), is simplified to

$$\dot{\boldsymbol{x}}(t) = \boldsymbol{f}(\boldsymbol{x}(t)) + \frac{1}{\epsilon} G\left(\boldsymbol{x}(t), \frac{t}{\epsilon}\right) \tag{4.7}$$

The resulting system is a high-frequency, high-amplitude, nonlinear time-varying system in the form of Eq. (3.7). If direct averaging was to be performed, the contribution of the pitching and plunging motions to the average dynamics would be neglected due to the zero mean of the cosine signals. Thus, it is necessary to apply the averaging technique described in Section 3.3. The application of chronological calculus and averaging to the ROM (4.1)

leads to the average dynamics of the system

$$\frac{d}{dt}\begin{pmatrix} \bar{\boldsymbol{x}}_c \\ \bar{x}_v \\ \bar{x}_s \\ \bar{\alpha} \\ \bar{\dot{\alpha}} \\ \bar{\dot{h}} \end{pmatrix} = \begin{pmatrix} \boldsymbol{A}\bar{\boldsymbol{x}}_c + \boldsymbol{B}\Gamma_0\left(\bar{\alpha}, \bar{\dot{\alpha}}, \bar{\dot{h}}\right) \\ -\frac{1}{\tau_v}\left[\bar{x}_v + \left(U\cos\bar{\alpha} - \bar{\dot{h}}\sin\alpha\right)\bar{\dot{\alpha}}\right] \\ -\frac{1}{\tau_1}\left[\bar{x}_s - x_0\left(\bar{\alpha} + \arctan\frac{\bar{\dot{h}}}{U} - \tau_2\bar{\dot{\alpha}}\right)\right] \\ \bar{\dot{\alpha}} \\ 0 \\ 0 \end{pmatrix} + \begin{pmatrix} \bar{\boldsymbol{\mathcal{G}}}_{nx1}\left(\bar{\alpha}\right) \\ \bar{\mathcal{G}}_{n+1}\left(\bar{\alpha}\right) \\ \bar{\mathcal{G}}_{n+2}\left(\bar{\alpha}\right) \\ 0 \\ 0 \\ 0 \end{pmatrix} + \mathcal{O}\left(\epsilon^3\right) \tag{4.8}$$

where $\bar{\boldsymbol{\mathcal{G}}}_{nx1}\left(\bar{\alpha}\right)$ are the first n components of the vector field $\boldsymbol{\mathcal{G}}$ averaged over one cycle of motion, and $\bar{\mathcal{G}}_{n+1}\left(\bar{\alpha}\right)$ and $\bar{\mathcal{G}}_{n+2}\left(\bar{\alpha}\right)$ are the $(n+1)$-th and $(n+2)$-th entries, respectively. These indicated components are the only non-zero entries, and they depend only on the angle of attack. Since the pullback is defined as an infinite series of integrals (Eq. (3.10)), in these calculations the series are truncated after the order $\mathcal{O}\left(\epsilon^2\right)$.

According to the averaging theorem, the properties of an original nonlinear time-periodic system may be inferred from the equilibrium of the averaged dynamics of such system. As such, once the average dynamics of ROM (2.64) are obtained, the equilibrium of the averaged system is calculated. To do so, the left hand side of the averaged dynamics in Eq. (3.3) is set to zero, and the system is solved for $\boldsymbol{x}^*$ that satisfies the equation

$$\mathbf{0} = \bar{\boldsymbol{f}}\left(\boldsymbol{x}^*\right) + \bar{\boldsymbol{\mathcal{G}}}\left(\boldsymbol{x}^*\right) \tag{4.9}$$

Since the last three components of the vector field $\bar{\boldsymbol{\mathcal{G}}}$ are zeros, the equilibrium of the last two states $\dot{\alpha}$ and $\dot{h}$ is automatically satisfied; and the $\bar{\alpha}$ equilibrium equation indicates that $\dot{\alpha}^* = 0$. As a simplification of the equations, since the equilibrium of $\dot{h}$ is automatically satisfied, its value is taken to be zero, $\dot{h}^* = 0$. The mean angle of attack α^* is kept arbitrary, to study the effect of the angle of attack on the average dynamics. As such, the equilibrium

values of the states of the system are

$$\begin{aligned} \boldsymbol{x}_c^* &= -\boldsymbol{A}^{-1}\left(\bar{\boldsymbol{\mathcal{G}}}_{nx1}\left(\alpha^*\right) + \boldsymbol{B}UbC_{L,s}\left(\alpha^*\right)\right) \\ x_v^* &= \frac{Hb\omega}{\tau_v}\cos\alpha\sin\phi \\ x_s^* &= x_0\left(\alpha^*\right) + \tau_1\mathcal{G}_{n+2}\left(\alpha^*\right) \end{aligned} \tag{4.10}$$

Once the equilibrium point $\boldsymbol{x}$ of the averaged dynamics is known, the average values of the output values can be obtained. Since the relationship between the lift, drag, and separation point and the states $\boldsymbol{x}$ is nonlinear, their average is not simply the substitution of the equilibrium values into their expressions. For example, the average lift force is not $L\left(\boldsymbol{x}^*\right)$. Instead, the states are defined using a first order approximation of the form $x_i(t) = x_i^* + A_{x_i}\cos\left(\omega t + \phi_i\right)$. With this approximation, the outputs of the function $y_m\left(\boldsymbol{x}\right), m \in \left(L, \mathcal{D}, x_s\right)$ are expanded around $\boldsymbol{x}^*$ in a multi-variable Taylor series expansion

$$\begin{aligned} y_m &= \sum_{n_1=0}^{\infty}\cdots\sum_{n_d=0}^{\infty}\frac{\left(x_1 - x_1^*\right)^{n_1}\ldots\left(x_d - x_d^*\right)^{n_d}}{n_1!\ldots n_d!}\left(\frac{\partial^{n_1+\cdots+n_d}y_m}{\partial x_1^{n_1}\ldots\partial x_d^{n_d}}\right)\left(\boldsymbol{x}^*\right) \\ &= y_m\left(\boldsymbol{x}^*\right) + \sum_{i=1}^{n+5}\frac{\partial y_m\left(\boldsymbol{x}^*\right)}{\partial x_i}\left(x_i - x_i^*\right) + \frac{1}{2!}\sum_{i=1}^{n+5}\sum_{q=1}^{n+5}\frac{\partial^2 y_m\left(\boldsymbol{x}^*\right)}{\partial x_i\partial x_q}\left(x_i - x_i^*\right)\left(x_q - x_q^*\right) + \ldots \end{aligned} \tag{4.11}$$

Finally, the average of Eq. (4.11) gives the averaged output over one cycle of motion

$$\bar{y}_m = \frac{1}{T}\int_0^T y_m(t)dt \tag{4.12}$$

4.2.1 Average lift coefficient

The lift coefficient of a two-dimensional airfoil is defined as

$$C_L = \frac{L}{\rho U^2 b} \tag{4.13}$$

Hence, the application of Eq. (4.12) to the lift coefficient leads to

$$\begin{aligned}\overline{C}_L = {} & C_{L,s}\left(\alpha^*\right) - HkC'_{L,s}\left(\alpha^*\right)\sin\phi \\ & + \left[\frac{k_{hf}A_\alpha^2}{4} + \frac{H^2k^2}{2}\left(\frac{1}{2} + \sin^2\phi\right) - \frac{k_{hf}A_\alpha Hk}{2}\sin\phi\right] C''_{L,s}\left(\alpha^*\right) \\ & + \frac{Hkm_v}{\rho U b \tau_v}\cos^2\alpha^*\sin\phi + \mathcal{O}\left(\epsilon^4; m_v, A_\alpha\right)\end{aligned} \tag{4.14}$$

where the series is truncated after $\mathcal{O}\left(\epsilon^2\right)$. The lack of terms of orders $\mathcal{O}\left(\epsilon^2\right)$ and $\mathcal{O}\left(\epsilon^3\right)$ results in a remainder of $\mathcal{O}\left(\epsilon^4\right)$. The parameters $C'_{L,s} = \frac{\partial C_{L,s}}{\partial \alpha}$ and $C''_{L,s} = \frac{\partial^2 C_{L,s}}{\partial \alpha^2}$ are the first and second derivatives of the steady lift coefficient curve as a function of the angle of attack, respectively. The variable $\overline{C}_L$ represents the mean unsteady lift coefficient of a pitching-plunging airfoil over one cycle of motion, whereas $C_{L,s}\left(\alpha^*\right)$ is the steady lift coefficient at the mean angle of attack α^*. Any difference between these two coefficients represents lift enhancement or reduction due to unsteady effects. Therefore, the average dynamics of the lift coefficient are modified due to zero mean, low-amplitude, high-frequency oscillations; Eq. (4.14) points to symmetry breaking in the flow.

In the particular case in which the pitching and plunging motions are in phase, the average lift coefficient is

$$\overline{C}_L = C_{L,s}\left(\alpha^*\right) + \frac{1}{4}\left(k_{hf}A_\alpha^2 + H^2k^2\right) C''_{L,s}\left(\alpha^*\right) + \mathcal{O}\left(\epsilon^4; m_v, A_\alpha\right) \tag{4.15}$$

Eq. (4.15) implies that there may be lift enhancement due to the pitching and plunging

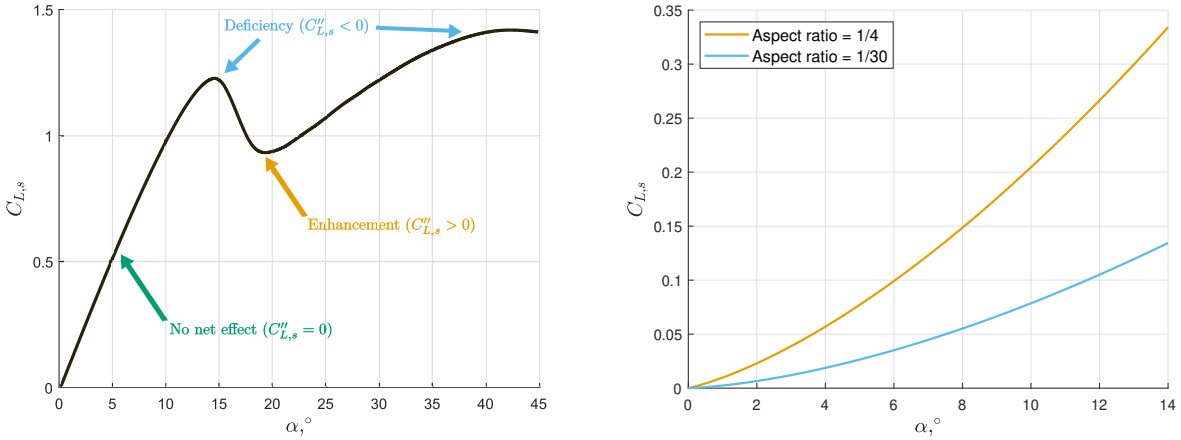

(a) NACA 0012 airfoil, $Re = 500,000$ [81].

(b) Delta wing [13].

Figure 4.1: Steady lift curve for a NACA 0012 airfoil and a three-dimensional delta wing.

motion of the airfoil. Moreover, this increment is proportional to the curvature of the steady lift coefficient curve. The expression also reveals the role of the pitching contribution due to added-mass effects in the higher order contributions, which are proportional to m_v and A_α. Besides, when the pitching and plunging motions are not in phase, Eq. (4.14) hints to possible lift enhancement or deficiency due to the out-of-phase motion of the pitching and plunging oscillations and added mass effects proportional to H.

These results point to the role of the curvature of the steady lift coefficient as the parameter controlling lift enhancement in unsteady conditions. To understand the implications of this finding, one may refer to the steady lift coefficient curve as a function of the angle of attack. On a conventional airfoil, such as the NACA 0012 presented in Fig. 4.1a, the curvature of the lift curve is almost zero in the linear regime at small angles of attack, suggesting that the steady and mean unsteady lift coefficients have similar values. Nonetheless, in the stall region, the curvature becomes negative, pointing to lift deficiency in this regime and, consequently, a decrease in lift due to unsteady motion. More interestingly, in the post-stall regime, the positive curvature suggests an increment in the unsteady lift with respect to its steady counterpart. This behavior may be different for different wings and airfoils. For example, on a delta wing (Fig. 4.1b), the steady lift curve shows a positive curvature even at

	$C_{L,s}$	$\overline{C}_L$	$(\overline{C}_L - C_{L,s})/C_{L,s}$
$\alpha^* = 5°$ (pure-plunging)	0.6371	0.6605	3.67%
$\alpha^* = 8°$ (pure-plunging)	0.8937	0.7029	−21.35%
$\alpha^* = 10°$ (pure-plunging)	1.0097	0.8752	−13.32%
$\alpha^* = 8°$ (pure-pitching)	0.8888	0.6574	−26.04%

Table 4.1: Steady lift coefficient, mean unsteady lift, and percentage of increase in the lift coefficient experienced by a SD7003 airfoil pitching and plunging at $k = 0.1$ and $Re = 60,000$ at different mean angles of attack. Data extracted from [65].

low α due to an attached leading-edge vortex (LEV). As a result, the present theory suggests lift enhancement even in this regime.

The results are verified through experimental and numerical studies available in the literature, such as McCroskey *et al.* [49], Carr [12], Rival and Tropea [65], Cleaver *et al.* [17], and Chiereghin *et al.* [14]. For examle, For example, Rival and Tropea [65] measured the lift force and aerodynamic moment on the SD7003 airfoil oscillating under different pitching and plunging conditions at $Re = 60,000$. Fig. 4a of their work shows the results for a reduced frequency of $k = 0.1$, which have been summarized in Table 4.1. When the airfoil is plunging around $\alpha^* = 5°$ (linear regime), the difference between the average unsteady lift $\overline{C}_L$ and the steady lift at the mean angle of attack $C_{L,s}(\alpha^*)$ is negligible. Nonetheless, when the airfoil oscillates around $\alpha^* = 8, 10°$, near the peak in the stall regime at that Re ($\alpha_s = 10°$), there is a 21% and 13% decrease in the unsteady lift coefficient with respect to its steady value, respectively. For a pitching motion around $\alpha^* = 8°$, there is also a decrease in the unsteady lift of 26%. Similar results are observed in the experimental studies of Carr [12] and McAlister *et al.* [47] for airfoils oscillating at high frequencies and small amplitudes. For an example of lift enhancement, the reader can refer to Chiereghin *et al.* [14], where the average lift force in a periodically plunging NACA 0012 airfoil at $Re = 20,000$ was measured for different ranges of amplitudes of motion, reduced frequencies, and mean angles of attack. In their work, they list the average unsteady lift coefficient as a function of the reduced frequency and the plunging amplitude. Their results for small amplitudes and high

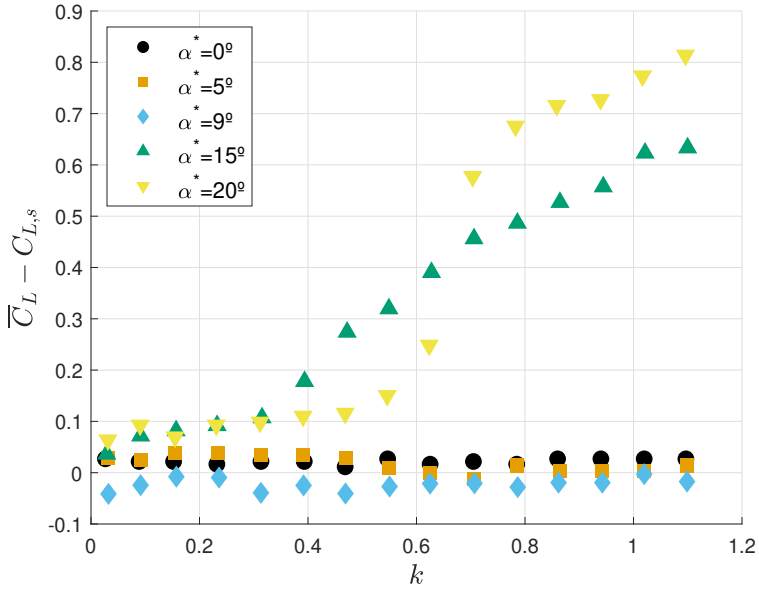

Figure 4.2: Variation of mean unsteady lift enhancement as a function of k for a NACA 0012 airfoil plunging with an amplitude of $H = 0.05$ at $Re = 20,000$. Data extracted from [14].

frequencies (summarized in Fig. 4.2) match the trend discovered in Eq. (4.15); there is a lift decrease when plunging around angles of attack in the stall region ($\alpha^* = 9°$ for $Re = 20,000$) but an increase in lift when plunging in the post-stall region ($\alpha^* = 15, 20°$). No appreciable difference in the lift force is observed in the linear region ($\alpha^* = 0, 5°$).

The previously mentioned studies refer to experimental results for small-amplitude, high-frequency pitching and/or plunging oscillations. The presented averaging results are not applicable to high amplitude oscillations, as the scaling parameters of Eq. (4.5) would not be valid and, consequently, the truncation of $\overline{C}_L$ up to order $\mathcal{O}(\epsilon^2)$ would not be correct. Similarly, the application of the averaging theorem requires oscillations at high frequencies. Otherwise, the theorem may lead to flawed results.

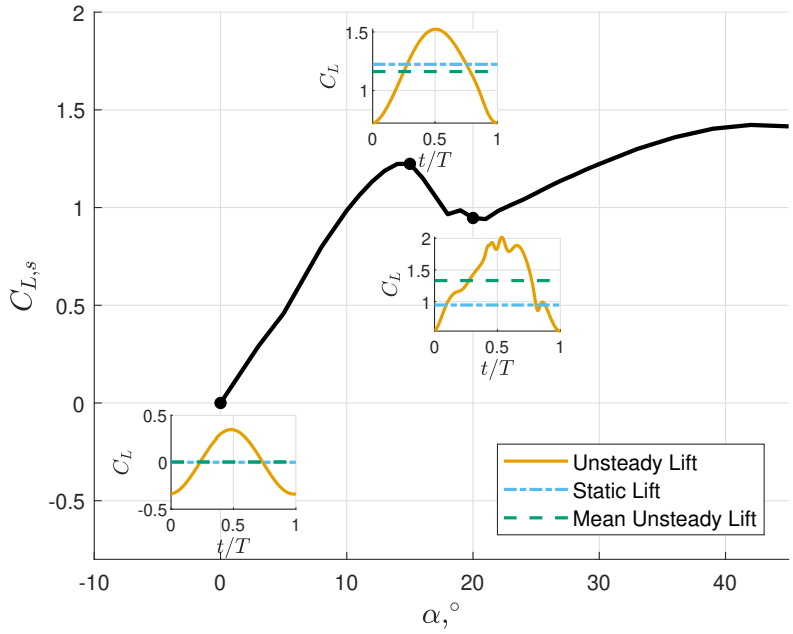

Figure 4.3: Steady $C_{L,s} - \alpha$ curve for a NACA 0012 airfoil at $Re = 500,000$ along with plunging simulations around $\alpha^* = 0, 15, 20°$ for $k = 0.5$ and $\arctan Hk = 5°$ [81].

Computational validation

The presented results are also validated through Unsteady Reynolds-Averaged Navier Stokes (URANS) simulations of a harmonically plunging NACA 0012 airfoil at $Re = 500,000$ [81]. The steady lift coefficient curve at this Re is presented in Fig. 4.1. The theoretical analysis performed above culminated in Eq. (4.15), which suggests that the parameter that controls the lift enhancement or reduction in unsteady conditions is the curvature of the steady lift coefficient curve. Thus, the validation of this finding requires the simulation of pitching and/or plunging motion around angles of attack located in the three different regimes: linear (where the analysis predicts no net effect on the lift), stall (decrease in the lift coefficient), and post-stall regimes (increase in the average lift coefficient). According to Fig. 4.1, the minimum curvature is at the peak of the $C_{L,s} - \alpha$ curve at $\alpha = °15°$, and the maximum curvature is at the trough at around $\alpha = 20°$. Therefore, the simulations are performed around a mean angle of attack of $\alpha^* = 0, 15, 20°$, which covers the three mentioned regions.

The computational simulations are performed at high frequency and small plunging amplitude to satisfy the assumptions made in the theoretical analysis ($\omega = \mathcal{O}(\frac{1}{\epsilon}), H = \mathcal{O}(\epsilon)$). On the other hand, the effective angle of attack $\alpha_{eff} = \alpha^* \pm \arctan Hk$ should stay within the curvature of the range of study. Therefore, a reduced frequency of $k = 0.5$ and a plunging amplitude $\arctan Hk = 5^\circ$ are chosen. For more details on the setup of the URANS simulations refer to Taha *et al.* [81].

The results are summarized in Fig. 4.3. The black line illustrates the steady lift coefficient curve of the NACA 0012 airfoil at $Re = 500,000$, also computed with URANS simulations. The black dots on the curve indicate the angles of attack at which the plunging simulations were performed. The small boxes next to the black dots show the evolution of the unsteady lift coefficient compared with its average value and the steady $C_{L,s}$ at the same angle of attack. At $\alpha^* = 0^\circ$, in the linear regime ($C''_{L,s} = 0$), there is almost no change in the mean lift coefficient. Near the peak of the curve, when plunging around $\alpha^* = 15^\circ$ ($C''_{L,s} < 0$), there is a 5% decrease in the unsteady lift coefficient when compared to its steady value. Finally, at the trough of the lift curve, around $\alpha^* = 20^\circ$ ($C''_{L,s} > 0$), the simulation shows a 40.7% enhancement of the lift coefficient. A more detailed representation of the time evolution of the unsteady lift coefficient when plunging around $\alpha^* = 15, 20^\circ$ can be found in Fig. 4.3. These results support the trends predicted by the geometric control analysis. At the same time, the curvature of the steady lift coefficient is consolidated as the parameter governing the enhancement or deficiency in the lift coefficient resulting from zero-mean, small-amplitude, hihg-frequency plunging oscillations.

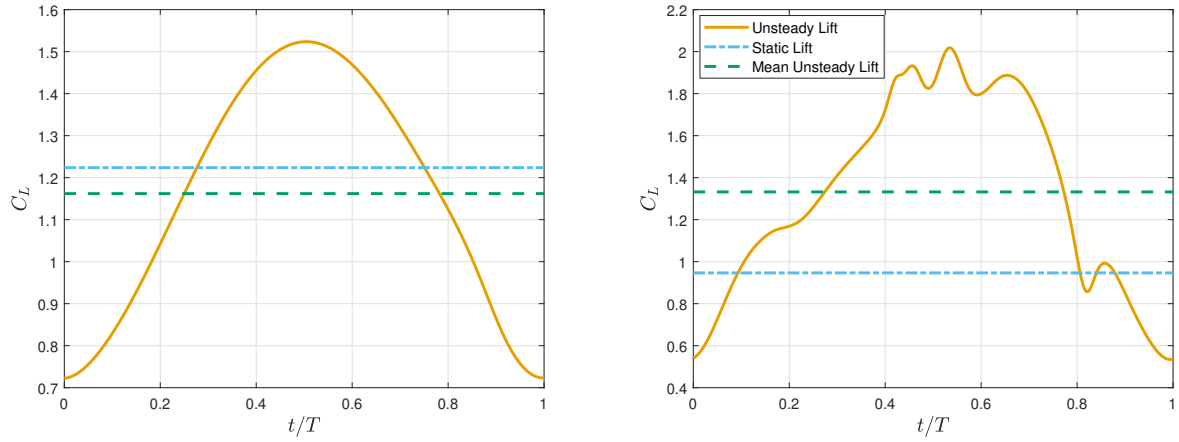

(a) $\alpha^* = 15°$. (b) $\alpha^* = 20°$.

Figure 4.4: Comparison of the unsteady lift coefficient over one plunging cycle with its average and the steady lift coefficient for a NACA 0012 airfoil at $k = 0.5$ and $\arctan Hk = 5°$ at $Re = 500,000$ [81].

4.2.2 Average drag coefficient

The drag coefficient of a two-dimensional airfoil is defined as

$$C_D = \frac{\mathcal{D}}{\rho U^2 b} \tag{4.16}$$

Thus, the application of Eq. (4.12) to the drag coefficient leads to

$$\begin{aligned}
\overline{C}_D &= C_{D,s}(\alpha^*) - Hk\sin\phi C'_{L,s}(\alpha^*)\left[\tan\alpha^* - \frac{k_S}{2\pi^2}C_{L,s}(\alpha^*)\right] \\
&+ \frac{A_\alpha^2}{4}\left\{\frac{2}{\cos^2\alpha^*}\left[C_{L,s}(\alpha^*)\tan\alpha^* + k_{hf}C'_{L,s}(\alpha^*)\right] + k_{hf}C''_{L,s}(\alpha^*)\tan\alpha^*\right. \\
&\left. - \frac{k_S}{2\pi^2}\left[k_{hf}C''_{L,s}(\alpha^*)C_{L,s}(\alpha^*) + k_{hf}^2\left(C'_{L,s}(\alpha^*)\right)^2 + k^2\left[k_{hf}k_{\dot\alpha}\left(k_{hf}k_{\dot\alpha} - 2\pi\right) + \pi^2\right]\right]\right\} \\
&+ \frac{H^2k^2}{4}\left\{\left(1 + 2\sin^2\phi\right)C''_{L,s}(\alpha^*)\tan\alpha^*\right. \\
&\left. - \frac{k_S}{2\pi^2}\left[\left(1 + 2\sin^2\phi\right)C''_{L,s}(\alpha^*)C_{L,s}(\alpha^*) + \left(k_{hf}^2 + 2\sin^2\phi\right)\left(C'_{L,s}(\alpha^*)\right)^2\right]\right\}
\end{aligned}$$

$$- \frac{k_{hf} A_\alpha H k}{2} \Bigg\{ C''_{L,s}(\alpha^*) \tan\alpha^* \sin\phi + \frac{\sin\phi}{\cos^2\alpha^*} C'_{L,s}(\alpha^*)$$
$$- \frac{k_S}{2\pi^2} \left[\left[C_{L,s}(\alpha^*) C''_{L,s}(\alpha^*) + k_{hf} \left(C'_{L,s}(\alpha^*) \right)^2 \right] \sin\phi + k \left(\pi - k_{hf} k_{\dot{\alpha}} \right) C'_{L,s}(\alpha^*) \cos\phi \right] \Bigg\}$$
$$+ \frac{H m_v k}{\rho U b \tau_v} \sin\alpha^* \cos\alpha^* \sin\phi + \mathcal{O}\left(\epsilon^3\right) \quad (4.17)$$

where the series is truncated after $\mathcal{O}(\epsilon^2)$. The variable $\overline{C}_D$ represents the mean unsteady drag coefficient of a pitching-plunging airfoil, and $C_{D,s}(\alpha^*)$ is the steady drag coefficient as a function of the mean angle of attack α^*. A difference between these two coefficients indicates an increase or a reduction in the drag force due to unsteady effects.

In the particular case in which the pitching and plunging motions are in phase

$$\overline{C}_D = C_{D,s}(\alpha^*) + \frac{A_\alpha^2}{4} \Bigg\{ \frac{2}{\cos^2\alpha^*} \left[C_{L,s}(\alpha^*) \tan\alpha^* + k_{hf} C'_{L,s}(\alpha^*) \right] + k_{hf} C''_{L,s}(\alpha^*)$$
$$- \frac{k_S}{2\pi^2} \left[k_{hf} C''_{L,s}(\alpha^*) C_{L,s}(\alpha^*) + k_{hf}^2 \left(C'_{L,s}(\alpha^*) \right)^2 + k^2 \left[k_{hf} k_{\dot{\alpha}} \left(k_{hf} k_{\dot{\alpha}} - 2\pi \right) + \pi^2 \right] \right] \Bigg\}$$
$$+ \frac{H^2 k^2}{4} \left\{ C''_{L,s}(\alpha^*) \tan\alpha^* - \frac{k_S}{2\pi^2} \left[C''_{L,s}(\alpha^*) C_{L,s}(\alpha^*) + k_{hf}^2 \left(C'_{L,s}(\alpha^*) \right)^2 \right] \right\}$$
$$+ \frac{k_S k_{hf} A_\alpha H k^2}{4\pi^2} \left(\pi - k_{hf} k_{\dot{\alpha}} \right) C'_{L,s}(\alpha^*) + \mathcal{O}\left(\epsilon^3\right) \quad (4.18)$$

The contribution to the unsteady drag coefficient due to the pitching appears in the first and second lines of Eq. (4.18). The third line shows the contribution of the plunging motion. And the last line reveals the effect of the combination of both pitching and plunging motions.

Focusing on the effect of the plunging motion, the average drag of a pure-plunging airfoil is given by the expression

$$\overline{C}_D = C_{D,s}(\alpha^*) + \frac{H^2 k^2}{4} \Bigg\{ C''_{L,s}(\alpha^*) \tan\alpha^* - \frac{k_S}{2\pi^2} \left[C''_{L,s}(\alpha^*) C_{L,s}(\alpha^*) + k_{hf}^2 \left(C'_{L,s}(\alpha^*) \right)^2 \right] \Bigg\}$$
$$+ \mathcal{O}\left(\epsilon^3\right) \quad (4.19)$$

The difference between the average unsteady drag coefficient and the steady drag coefficient evaluated at the mean angle of attack is given by a term proportional to the parameters of the plunging motion, the amplitude H and the reduced frequency k. The analytical nature of this work permits a distillation of the parameters causing an increase or decrease in the drag force. For example, the last term $-\frac{k_S k_{hf}^2}{2\pi^2}\left(C'_{L,s}\left(\alpha^*\right)\right)^2$ is negative, indicating thrust production proportional to the lift curve slope. This term represents the thrust production mechanism occurring in the linear regime due to plunging oscillations defined by Garrick [20]. In fact, substituting the parameters of the term for its values in potential flow ($k_S = 2\pi$, $C'_{L,s} = 2\pi$), and recalling that k_{hf} is the frequency gain of the lift transfer function given by Theodorsen's function ($k_{hf} = |C(k)|$), Garrick's result is recovered

$$C_T = \pi H^2 k^2 |C(k)|^2 \tag{4.20}$$

Therefore, Eq. (4.19) is a high-frequency generalization of Garrick's classical result to arbitrary lift dynamics and mechanisms. The model permits any dynamics, lift does not have to be governed by Theodorsen's function $C(k)$; and the lift mechanism may take any form, the analysis is not restricted to a linear steady lift coefficient $2\pi\alpha$.

Eq. (4.18) does not only reveal Garrick's thrust mechanism. The first two terms of the expression are proportional to $C''_{L,s}$, pointing to a nonlinear drag/thrust generation mechanism in the stall and/or post-stall regions. The first term implies an increase in the drag force that occurs due to lift enhancement in the regions with positive curvature, or a decrease in the drag force due to lift deficiency when the curvature is negative. The second term appears from the suction force and generates thrust when $C''_{L,s} > 0$. Both of these terms are competing, one increases the drag force while the other one reduces it; as such, a study is performed to determine their role in the generation of thrust or drag. However, before such study, it is necessary to understand the mechanisms behind the steady drag force.

Fig. 4.5 shows the projection of the static lift coefficient in the direction of the free stream and the static drag coefficient as a function of the angle of attack. The results are obtained from RANS simulation of a NACA 0012 airfoil at $Re = 500,000$. In the absence of leading-edge suction and skin friction, the resultant of the aerodynamic forces is normal to the wing surface [71]. Therefore, with a simple geometric relation, the drag coefficient may be approximated as the projection of the lift coefficient in the direction of the free stream $C_{L,s} \tan \alpha$. Using this definition, the present work defines the suction force coefficient as

$$C_S = C_L \tan \alpha - (C_D - C_{D,f}) \tag{4.21}$$

with $C_{D,f}$ being the skin friction drag coefficient. Fig. 4.5 shows the resulting suction force coefficient obtained from the application of Eq. (4.21) using the lift and drag coefficients obtained from the URANS simulations. The figure shows a significant difference between $C_{L,s} \tan \alpha$ and $C_{D,s}$ at small angles of attack, hinting at the importance of the suction force in the linear regime. However, C_S reaches a maximum value at stall ($\alpha \simeq 15°$) and decreases at higher angles of attack. Defining the relation between the suction force coefficient and the lift coefficient to be the following

$$C_S = \frac{k_S}{4\pi^2} C_L^2 \tag{4.22}$$

one can examine the changes in the suction parameter k_S with the angle of attack. Fig. 4.5 shows an increase of the suction parameter with α followed by a sudden decrease at stall. The significant change in k_S over the studied range, suggests that the calculation of the drag coefficient needs to account for the derivatives of the suction parameter.

The unsteady drag force coefficient experiences similar force mechanisms as those described for the steady drag coefficient. To understand the change in the average drag force due to low-amplitude, high-frequency plunging oscillations, the present study defines the thrust

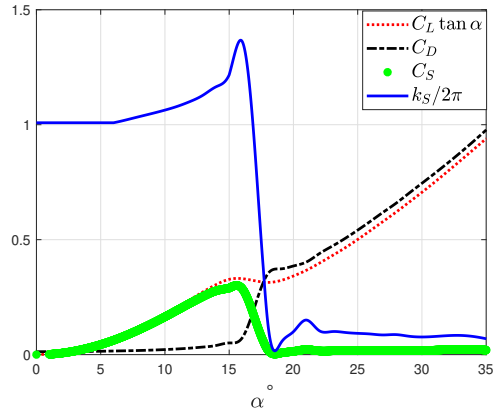

Figure 4.5: Projection of the steady lift, drag and suction force coefficients, and suction parameter for a NACA 0012 airfoil at $Re = 500,000$ [81].

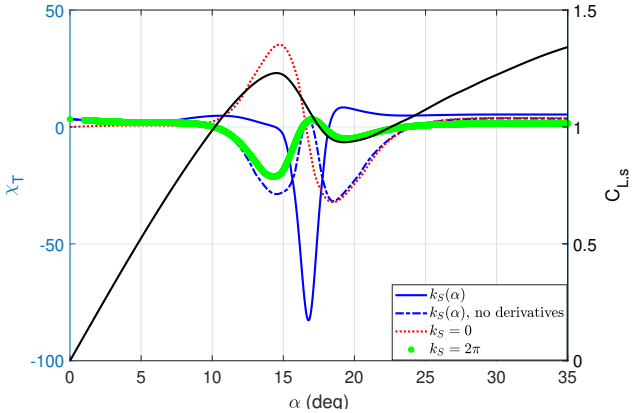

Figure 4.6: Effect of the plunging motion on the thrust parameter χ_T. The solid black line represents the steady lift coefficient curve of a NACA 0012 airfoil at $Re = 500,000$ [81].

generation parameter χ_T as

$$\chi_T = -\frac{\overline{C}_D - C_{D,s}(\alpha^*)}{H^2k^2/4}$$
$$= -C''_{L,s}(\alpha^*)\tan\alpha^* + \frac{k_S}{2\pi^2}\left[C''_{L,s}(\alpha^*)\,C_{L,s}(\alpha^*) + k_{hf}^2\left(C'_{L,s}(\alpha^*)\right)^2\right] \quad (4.23)$$

The thrust generation parameter measures the capacity of the flow to generate thrust. A positive χ_T reveals the production of thrust, and a negative value indicates an increase on the drag force. Fig. 4.6 shows the thrust generation parameter χ_T as a function of the mean angle of attack α^*. The plotted results show the application of Eq. (4.23) using the $C_{L,s}$, $C_{D,s}$, and k_S values obtained from the steady simulations of a NACA 0012 airfoil at $Re = 500,000$. The figure also shows the effect of k_S on the thrust control parameter. The red line shows the value of χ_T with no suction present in the flow ($k_S = 0$). In other words, referring to Eq. (4.23), the red line indicates the effect of the curvature on the average drag coefficient, with χ_T only accounting for the first term, $-C''_{L,s}(\alpha^*)\tan\alpha^*$. The other lines show the difference in the thrust generation parameter when assuming a constant $k_S = 2\pi$, a varying k_S but without accounting for its derivatives (dashed blue line), and a k_S that

changes with the angle of attack, including the effect of its derivatives (solid blue line). The results indicate the importance of the evolution of k_S with α in the determination of the average drag coefficient. Therefore, the average drag coefficient of a plunging airfoil over one cycle of motion, when considering the changing nature of k_S is given by

$$\overline{C}_D = C_{D,s}(\alpha^*) + \frac{H^2k^2}{4}\Bigg\{C''_{L,s}(\alpha^*)\tan\alpha^* - \frac{k_S}{2\pi^2}\left[C_{L,s}(\alpha^*)C''_{L,s}(\alpha^*) + k_{hf}^2\left(C'_{L,s}(\alpha^*)\right)^2\right] - \frac{C_{L,s}(\alpha^*)}{\pi^2}\left[k_{hf}k'_s(\alpha^*)C'_{L,s}(\alpha^*) + \frac{k''_s(\alpha^*)C_{L,s}(\alpha^*)}{4}\right]\Bigg\} + \mathcal{O}\left(\epsilon^3\right) \quad (4.24)$$

where $k'_S = \frac{\partial k_S}{\partial \alpha}$ and $k''_S = \frac{\partial^2 k_S}{\partial \alpha^2}$ are the first and second derivatives of the suction parameter as a function of the angle of attack, respectively. The results of Eq. (4.24) are represented by the solid blue line in Fig. 4.6. At small angles of attack, the thrust generation parameter is positive, predicting generation of thrust. This is the thrust generation mechanism in the linear regime described by Garrick [20], given by the last term in the first line of Eq. (4.24). However, in the stall region the theory shows an increase in the average drag coefficient. The effect can be highly attributed to the first term in brackets of the first line of Eq. (4.24), which accounts for the increase in the drag force due to lift enhancement. Finally, in the post-stall regime, χ_T becomes positive, indicating the generation of thrust due to suction in the nonlinear regime.

The effects of the pitching motion are similar to those of plunging. The average drag coefficient for an airfoil pitching at low amplitudes and high frequencies is

$$\overline{C}_D = C_{D,s}(\alpha^*) + \frac{A_\alpha^2}{4}\Bigg\{\frac{2}{\cos^2\alpha^*}\left[C_{L,s}(\alpha^*)\tan\alpha^* + k_{hf}C'_{L,s}(\alpha^*)\right] + k_{hf}C''_{L,s}(\alpha^*)\tan\alpha^* - \frac{k_S}{2\pi^2}\left[k_{hf}C_{L,s}(\alpha^*)C''_{L,s}(\alpha^*) + k_{hf}^2\left(C'_{L,s}(\alpha^*)\right)^2 + k^2\left(\pi - k_{\dot\alpha}k_{hf}\right)^2\right] - \frac{C_{L,s}(\alpha^*)}{\pi^2}\left[k_{hf}k'_s(\alpha^*)C'_{L,s}(\alpha^*) + \frac{k''_s(\alpha^*)C_{L,s}(\alpha^*)}{4}\right]\Bigg\} + \mathcal{O}\left(\epsilon^3\right) \quad (4.25)$$

Therefore, the thrust generation parameter for a pitching wing becomes

$$\begin{aligned}\chi_T &= -\frac{\overline{C}_D - C_{D,s}(\alpha^*)}{A_\alpha^2/4} \\ &= -\frac{2}{\cos^2\alpha^*}\left[C_{L,s}(\alpha^*)\tan\alpha^* + k_{hf}C'_{L,s}(\alpha^*)\right] - k_{hf}C''_{L,s}(\alpha^*)\tan\alpha^* \\ &+ \frac{k_S}{2\pi^2}\left[k_{hf}C_{L,s}(\alpha^*)C''_{L,s}(\alpha^*) + k_{hf}^2\left(C'_{L,s}(\alpha^*)\right)^2 + k^2\left(\pi - k_{\dot\alpha}k_{hf}\right)^2\right] \\ &+ \frac{C_{L,s}(\alpha^*)}{\pi^2}\left[k_{hf}k'_s(\alpha^*)C'_{L,s}(\alpha^*) + \frac{k''_s(\alpha^*)C_{L,s}(\alpha^*)}{4}\right] \quad (4.26)\end{aligned}$$

Eq. (4.26) shows a higher dependency on the high-frequency gain k_{hf}, when compared to the plunging motion. Another difference is the role of the rotational terms through $k_{\dot\alpha}$. This contribution indicates that, as the reduced frequency k increases and the location of the pitching axis is moved backwards, the capability for thrust generation increases. These results are shown in Fig. 4.7, which plots Eq. (4.26) using the $C_{L,s}$, $C_{D,s}$, and k_S values obtained from the steady simulations of a NACA 0012 airfoil at $Re = 500,000$. In the linear regime, the thrust generation parameter is higher at higher k. In fact, contrary to the plunging motion, pure pitching oscillations only generate thrust at low angles of attack past a certain threshold frequency, as described by Garrick [20]. The increase in chi_T due to the displacement of the pitching axis from the quarter-chord to the mid-chord is negligible in comparison with the effects of the reduced frequency.

As the angle of attack increases, the thrust generation parameter grows, reaching a maximum at stall. There is a sudden decrease in χ_T when oscillating at angles higher than stall, indicating an increase in the unsteady drag coefficient with respect to its steady counterpart. However, after the trough of the steady lift curve, the thrust generation capability is recovered. Nonetheless, at higher angles and once $C''_{L,s} < 0$, the airfoil loses its thrust generation capability.

Eq. (4.17) represents the combined effect of the pitching and plunging motions of the airfoil, but it does not account for the change on k_S with the angle of attack. As such, the average

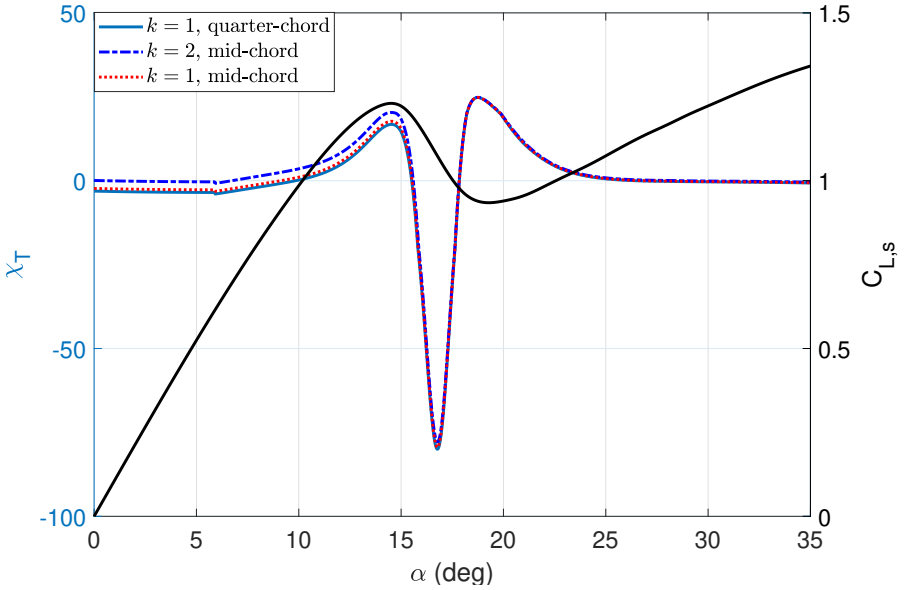

Figure 4.7: Effect of the pitching motion on the thrust parameter χ_T as a function of the mean angle of attack for different reduced frequencies k and locations of the pitching axis. The solid black line represents the steady lift coefficient curve [81].

unsteady drag force on a pitching-plunging airfoil is

$$
\begin{aligned}
\overline{C}_D = {} & C_{D,s}\left(\alpha^*\right) - Hk\left\{C'_{L,s}\left(\alpha^*\right)\left[\tan\alpha^* - \frac{k_S\left(\alpha^*\right)}{2\pi^2}C_{L,s}\left(\alpha^*\right)\right] + \frac{C^2_{L,s}\left(\alpha^*\right)}{4\pi^2}k'_S\left(\alpha^*\right)\right\}\sin\phi \\
& + \frac{Hkm_v}{\rho U b \tau_v}\sin\alpha^*\cos\alpha^*\sin\phi \\
& + \frac{A^2_\alpha}{4}\left\{\frac{2}{\cos^2\alpha^*}\left(C_{L,s}\left(\alpha^*\right)\tan\alpha^* + k_{hf}C'_{L,s}\left(\alpha^*\right)\right) + k_{hf}C''_{L,s}\left(\alpha^*\right)\tan\alpha^*\right. \\
& - \frac{k_S\left(\alpha^*\right)}{2\pi^2}\left[k_{hf}C_{L,s}\left(\alpha^*\right)C''_{L,s}\left(\alpha^*\right) + k^2_{hf}\left(C'_{L,s}\left(\alpha^*\right)\right)^2 + k^2\left(\pi - k_{\dot\alpha}k_{hf}\right)^2\right] \\
& \left. - \frac{C_{L,s}\left(\alpha^*\right)}{\pi^2}\left(k_{hf}k'_S\left(\alpha^*\right)C'_{L,s}\left(\alpha^*\right) + \frac{k''_S\left(\alpha^*\right)C_{L,s}\left(\alpha^*\right)}{4}\right)\right\} \\
& + \frac{H^2k^2}{4}\left\{\left(3 - 2\cos^2\phi\right)C''_{L,s}\left(\alpha^*\right)\tan\alpha^*\right. \\
& - \frac{k_S\left(\alpha^*\right)}{2\pi^2}\left[\left(3 - 2\cos^2\phi\right)C_{L,s}\left(\alpha^*\right)C''_{L,s}\left(\alpha^*\right) + \left(2\left(1 - \cos^2\phi\right) + k^2_{hf}\right)\left(C'_{L,s}\left(\alpha^*\right)\right)^2\right] \\
& - \frac{C_{L,s}\left(\alpha^*\right)}{\pi^2}\left[\left(2\left(1 - \cos^2\phi\right) + k_{hf}\right)k'_S\left(\alpha^*\right)C'_{L,s}\left(\alpha^*\right)\right.
\end{aligned}
$$

$$+\frac{k_S''(\alpha^*)\,C_{L,s}(\alpha^*)}{4}\left(3-2\cos^2\phi\right)\Bigg]\Bigg\}$$
$$-\frac{A_\alpha Hk}{2}\Bigg\{k_{hf}\left(C_{L,s}''(\alpha^*)\tan\alpha^*+\frac{C_{L,s}'(\alpha^*)}{\cos^2\alpha^*}\right)\sin\phi$$
$$-\frac{k_{hf}k_S(\alpha^*)}{2\pi^2}\Big[\left(C_{L,s}(\alpha^*)\,C_{L,s}''(\alpha^*)+k_{hf}\left(C_{L,s}'(\alpha^*)\right)^2\right)\sin\phi$$
$$+k\left(\pi-k_{\dot\alpha}k_{hf}\right)C_{L,s}'(\alpha^*)\cos\phi\Big]-\frac{C_{L,s}(\alpha^*)}{\pi^2}\Bigg[\frac{C_{L,s}(\alpha^*)\,k_S''(\alpha^*)}{4}\sin\phi$$
$$+k_S'(\alpha^*)\left(\frac{k}{2}\left(\pi-k_{\dot\alpha}k_{hf}\right)\cos\phi+k_{hf}C_{L,s}'(\alpha^*)\sin\phi\right)\Bigg]\Bigg\}+\mathcal{O}\left(\epsilon^3;m_v,A_\alpha,H\right)\quad(4.27)$$

In the particular case in which the pitching and plunging motions are in phase

$$\overline{C}_D=C_{D,s}(\alpha^*)+\frac{A_\alpha^2}{4}\Bigg\{\frac{2}{\cos^2\alpha^*}\left(C_{L,s}(\alpha^*)\tan\alpha^*+k_{hf}C_{L,s}'(\alpha^*)\right)+k_{hf}C_{L,s}''(\alpha^*)\tan\alpha^*$$
$$-\frac{k_S(\alpha^*)}{2\pi^2}\left[k_{hf}C_{L,s}(\alpha^*)\,C_{L,s}''(\alpha^*)+k_{hf}^2\left(C_{L,s}'(\alpha^*)\right)^2+k^2\left(\pi-k_{\dot\alpha}k_{hf}\right)^2\right]$$
$$-\frac{C_{L,s}(\alpha^*)}{\pi^2}\left(k_{hf}k_S'(\alpha^*)\,C_{L,s}'(\alpha^*)+\frac{k_S''(\alpha^*)\,C_{L,s}(\alpha^*)}{4}\right)\Bigg\}$$
$$+\frac{H^2k^2}{4}\Bigg\{C_{L,s}''(\alpha^*)\tan\alpha^*-\frac{k_S(\alpha^*)}{2\pi^2}\left[C_{L,s}(\alpha^*)\,C_{L,s}''(\alpha^*)+k_{hf}^2\left(C_{L,s}'(\alpha^*)\right)^2\right]$$
$$-\frac{C_{L,s}(\alpha^*)}{\pi^2}\left[k_{hf}k_S'(\alpha^*)\,C_{L,s}'(\alpha^*)+\frac{k_S''(\alpha^*)\,C_{L,s}(\alpha^*)}{4}\right]\Bigg\}$$
$$+\frac{A_\alpha Hk}{2}\left\{\frac{k_{hf}k_S(\alpha^*)}{2\pi^2}\left[k\left(\pi-k_{\dot\alpha}k_{hf}\right)C_{L,s}'(\alpha^*)\right]-\frac{k_S'(\alpha^*)\,C_{L,s}(\alpha^*)}{\pi^2}\left(\frac{k}{2}\left(\pi-k_{\dot\alpha}k_{hf}\right)\right)\right\}$$
$$+\mathcal{O}\left(\epsilon^3;m_v,A_\alpha,H\right)\quad(4.28)$$

Computational validation

A validation of the analytical results is performed by comparing them to numerical simulations of a plunging NACA 0012 airfoil at $k=0.5$ and $Re=500,000$. The plunging amplitude is defined by the effective amplitude $A_{eff}=\arctan Hk=5°$. The simulations are performed at the mean angles of attack $\alpha^*=0,12,14,15,16,17,18°$. Fig. 4.8 shows

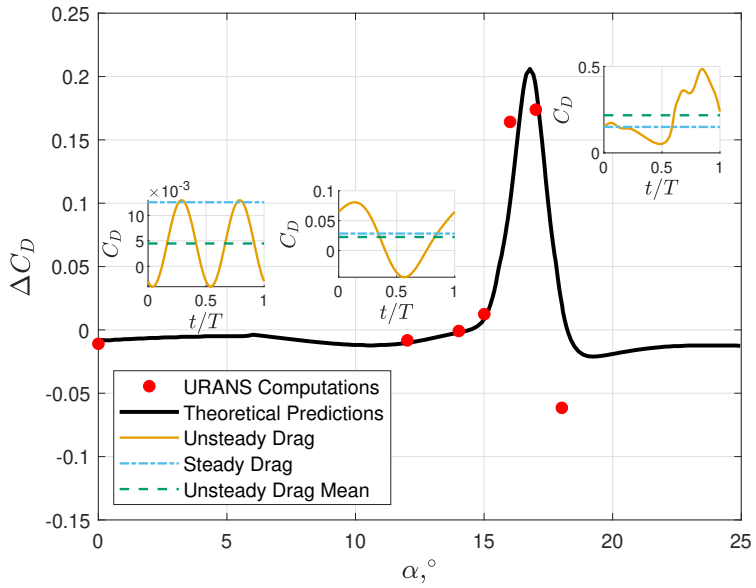

Figure 4.8: Theoretical predictions of the thrust control parameter χ_T against URANS simulations of a plunging NACA 0012 airfoil at $k = 0.5$ and $Re = 500,000$ [81].

the comparison between the theoretical results and the URANS simulations. The figure shows the difference between the mean unsteady drag coefficient and its steady counterpart, $\Delta C_D = \overline{C}_D - C_{D,s}$. Even though this work only provides qualitative trends, the accuracy of the results is satisfactory. The black line shows the theoretical values for ΔC_D, and the red dots indicate the computational results. The small figures show the time evolution of the unsteady C_D and its average over one cycle of motion, and compares it with the steady drag coefficient evaluated at the mean angle of attack for $\alpha^* = 0, 12, 17^\circ$. In the linear regime, the theory predicts a decrease in the drag force, which is observed in the simulation at $\alpha^* = 0^\circ$; the mean unsteady drag coefficient is 64% lower than the steady value. Similarly, at the mean angle of attack $\alpha^* = 12^\circ$, the theoretical results also anticipate a reduction in the drag coefficient, which is validated in the simulation, with $\overline{C}_D$ being 20% lower than $C_{D,s}$. For $\alpha^* = 17^\circ$, after the stall peak in the $C_{L,s} - \alpha$ curve, the theory implies an increase in the drag force, which is captured in the computational results with a 45% increase in drag with respect to the steady case.

4.2.3 Average location of the point of separation

The average location of the separation point over one cycle of motion is

$$\overline{x}_s = x_0\left(\alpha^*\right) + Hkx_0'\left(\alpha^*\right)\sin\phi + \frac{k^2}{4}\left[A_\alpha^2\hat{\tau}_2^2 + H^2\left(1+2\sin^2\phi\right) - 2A_\alpha H\hat{\tau}_2\cos\phi\right]x_0''\left(\alpha^*\right) + \mathcal{O}\left(\epsilon^4\right) \quad (4.29)$$

where the series is truncated after $\mathcal{O}\left(\epsilon^2\right)$. The lack of terms of orders $\mathcal{O}\left(\epsilon^2\right)$ and $\mathcal{O}\left(\epsilon^3\right)$ results in a remainder of $\mathcal{O}\left(\epsilon^4\right)$. The variable $x_0\left(\alpha^*\right)$ is the separation point evaluated at the mean angle of attack, and $\hat{\tau}_2 = \frac{\tau_2 U}{b}$. The parameters $x_0' = \frac{\partial x_0}{\partial \alpha}$ and $x_0'' = \frac{\partial^2 x_0}{\partial \alpha^{\cdot 2}}$ are the first and second derivatives of the steady location of the separation point as a function of the angle of attack, respectively. In the particular case in which the pitching and plunging motions are in phase, the location of the separation point is given by

$$\overline{x}_s = x_0\left(\alpha^*\right) + \frac{k^2}{4}\left[A_\alpha^2\hat{\tau}_2^2 + H^2 - 2A_\alpha H\hat{\tau}_2\right]x_0''\left(\alpha^*\right) + \mathcal{O}\left(\epsilon^4\right) \quad (4.30)$$

The effect of the unsteady motion on the location of the separation point depends on the second derivative of the steady location of the separation point as a function of the angle of attack. For a positive curvature, both pitching and plunging motions move the separation point backwards. Consequently, more surface of the airfoil is under attached flow conditions, which is generally desirable. However, for a negative curvature of x_0, the separation point moves forwards, increasing the surface of the airfoil under separation.

Fig. 4.9 shows the steady lift curve, the steady separation point, and the average unsteady separation point (obtained from Eq. (4.30)) for a plunging NACA 0012 airfoil at $Re = 500,000$. The difference between the steady and unsteady location of the point of separation is negligible in the linear regime. In the stall region ($C_{L,s}'' < 0$), the separation point moves forward, increasing the separated flow region on the airfoil. However, moving to the post-stall

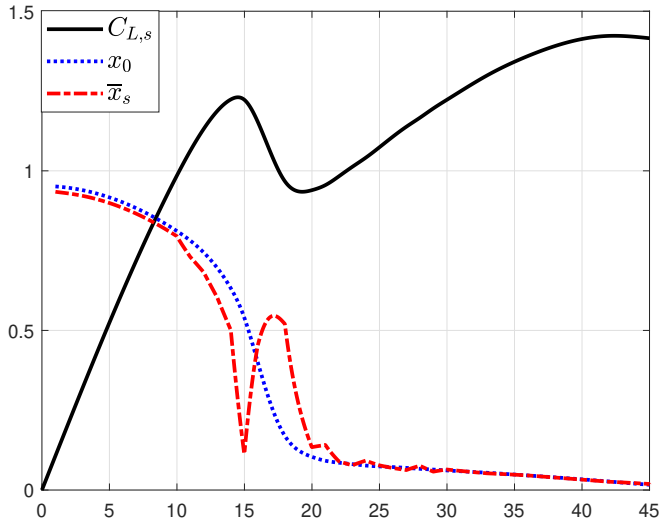

Figure 4.9: Steady lift curve, steady separation point, and average unsteady separation point as a function of the mean angle of attack for a NACA 0012 airfoil at $Re = 500,000$ and $k = 0.5$ plunging with an amplitude of $\arctan Hk = 5°$ [81].

regime ($C''_{L,s} > 0$), the unsteady separation point moves backwards, eventually surpassing the steady location. Near the trough $\overline{x}_s > x_0$, showing a reduction of the separated flow region under unsteady conditions. The difference between the steady and unsteady separation point becomes negligible again after the trough. Eq. (4.29) also points to a displacement of the separation point in the direction opposite to the curvature of x_0 when the airfoil is both performing pitching and plunging.

Chapter 5

Geometric control averaging of the Beddoes-Leishman model

The analysis performed in Chapter 4 demonstrates the capability of geometric control theory as a tool for the intrinsic discovery of force generation mechanisms in unsteady flows. The study of the low-Reynolds aerodynamic loads over a pitching-plunging airfoil in a geometric control framework uncovered unconventional lift enhancement and drag reduction mechanisms induced by the pitching and plunging motions. Similarly, this chapter aims to repeat the geometric control analysis described in Chapter 4 to study the nonlinear behavior of the average lift and drag forces over an oscillating airfoil, but with a focus on the contributions of the leading-edge vortex (LEV) during a harmonic dynamic stall maneuver [62].

The present chapter makes use of the Beddoes-Leishman model [37–39] derived in Section 2.4 to describe the dynamics of dynamic stall. This reduced-order model (ROM) satisfies the conditions required for a geometric control analysis: it reasonably captures the unsteady nonlinear aerodynamics of dynamic stall, and is represented in a state-space form, which is convenient for dynamical systems analysis as well as geometric control and averaging.

The following section describes the reformulation of the model in a geometric control framework. The model is then analyzed with a combination of mathematical tools from the averaging theorem and geometric control theory to derive analytical expressions for the mean lift and drag forces. Finally, these expressions are studied to uncover and identify the causes behind the lift and thrust enhancement mechanisms that may occur due to unsteady effects.

5.1 Reformulation of the Beddoes-Leishman model

The purpose of this section is the application of the Beddoes-Leishman model to the two-dimensional pitching-plunging airfoil introduced in Section 2.3.1. The system is also reformulated in the form of Eq. (2.41) to make it amenable to the geometric control analysis of Section 3.3. The first step is the formulation of all the equations using the state variables of the system instead of the outputs of previous equations

$$\frac{d}{dt}\begin{pmatrix} x_1 \\ x_2 \\ x_3 \\ x_4 \\ x_9 \\ x_{10} \\ x_{11} \\ \alpha \\ \dot{\alpha} \\ \dot{h} \end{pmatrix} = \begin{pmatrix} -b_1\left(\frac{\beta^2 U}{b}\right)x_1 \\ -b_2\left(\frac{\beta^2 U}{b}\right)x_2 \\ -\frac{x_3}{K_\alpha T_I} \\ -\frac{x_4}{K_q T_I} \\ \frac{U/b}{T_P}\left[C_{N_\alpha}\alpha_E - \frac{1}{MT_I}\left(\frac{4x_3}{K_\alpha}+\frac{x_4}{K_q}\right) - x_9\right] \\ \frac{U/b}{T_f}\left[-x_{10} + f'\left(\frac{x_9}{C_{N_\alpha}}\right)\right] \\ \frac{U/b}{T_v}\left[-x_{11} + \dot{C}_v\right] \\ \dot{\alpha} \\ 0 \\ 0 \end{pmatrix} + \begin{pmatrix} 1 \\ 1 \\ 1 \\ 0 \\ \frac{4}{M}\frac{U/b}{T_P} \\ 0 \\ 0 \end{pmatrix} \alpha_{eff} + \begin{pmatrix} 0.5 \\ 0.5 \\ 0 \\ 1 \\ \frac{1}{M}\frac{U/b}{T_P} \\ 0 \\ 0 \end{pmatrix} q \quad (5.1)$$

where $\beta = \sqrt{1-M^2}$ is the compressibility factor, and K_α, K_q, and T_I are parameters that depend on the Mach number M and the characteristics of the airfoil.

Once the relations are formulated in terms of the state variables, the system is rearranged such that the inputs of the state-space model are the pitching and plunging accelerations. To do so, it is worth reminding the reader the definitions of the kinematic effective angle of attack $\alpha_{eff} = \alpha + \arctan\left(\frac{\dot{h}}{U}\right)$, the non-dimensional pitch rate $q = \frac{2\dot{\alpha}b}{U}$, and the equivalent angle of attack $\alpha_E = \beta^2\left(\frac{U}{b}\right)(A_1 b_1 x_1 + A_2 b_2 x_2)$. The resulting control system of the Beddoes-Leishman model for the unsteady nonlinear dynamics of a pitching-plunging airfoil such that it is amenable to geometric control theory is

$$\frac{d}{dt}\begin{pmatrix} x_1 \\ x_2 \\ x_3 \\ x_4 \\ x_9 \\ x_{10} \\ x_{11} \\ \alpha \\ \dot{\alpha} \\ \dot{h} \end{pmatrix} = \begin{pmatrix} -b_1\left(\frac{\beta^2 U}{b}\right)x_1 + \alpha + \arctan\left(\frac{\dot{h}}{U}\right) + \frac{\dot{\alpha}b}{U} \\ -b_2\left(\frac{\beta^2 U}{b}\right)x_2 + \alpha + \arctan\left(\frac{\dot{h}}{U}\right) + \frac{\dot{\alpha}b}{U} \\ -\frac{x_3}{K_\alpha T_I} + \alpha + \arctan\left(\frac{\dot{h}}{U}\right) \\ -\frac{x_4}{K_q T_I} + \frac{2\dot{\alpha}b}{U} \\ \frac{U/b}{T_P}\left[C_{N_\alpha}\alpha_E - \frac{1}{MT_I}\left(\frac{4x_3}{K_\alpha} + \frac{x_4}{K_q}\right) - x_9 + \frac{4\left[\alpha + \arctan\left(\frac{\dot{h}}{U}\right)\right]}{M} + \frac{\dot{\alpha}b}{2UM}\right] \\ \frac{U/b}{T_f}\left[-x_{10} + f'\left(\frac{x_9}{C_{N_\alpha}}\right)\right] \\ \frac{U/b}{T_v}\left[-x_{11} + \dot{C}_v\right] \\ \dot{\alpha} \\ 0 \\ 0 \end{pmatrix} + \begin{pmatrix} 0 \\ 0 \\ 0 \\ 0 \\ 0 \\ 0 \\ 0 \\ 0 \\ 1 \\ 0 \end{pmatrix}\ddot{\alpha} + \begin{pmatrix} 0 \\ 0 \\ 0 \\ 0 \\ 0 \\ 0 \\ 0 \\ 0 \\ 0 \\ 1 \end{pmatrix}\ddot{h} \tag{5.2}$$

The resulting system takes the nonlinear control affine form of Eq. (2.41), repeated here for

clarity

$$\dot{\boldsymbol{x}}(t) = \boldsymbol{f}(\boldsymbol{x}(t)) + \boldsymbol{g}_\alpha(\boldsymbol{x}(t))\ddot{\alpha}(t) + \boldsymbol{g}_h(\boldsymbol{x}(t))\ddot{h}(t) \tag{5.3}$$

where $x = [x_1, x_2, x_3, x_4, x_9, x_{10}, x_{11}, \alpha, \dot{\alpha}, \dot{h}]$ is the state vector, and the control inputs u_α and u_h are the pitching and plunging accelerations $\ddot{\alpha}$ and $\ddot{h}$ respectively. The outputs of the system are the lift and drag coefficients

$$\boldsymbol{y}(t) = [C_L(t) \quad C_D(t)]^T \tag{5.4}$$

The pitching angle α and the plunging displacement h follow the harmonic motion described in Section 4.1. Hence, the accelerations (inputs of the system) take the same form as they did in the previous ROM, repeated here for clarity

$$u_\alpha = \ddot{\alpha} = \omega^2 A_\alpha \cos(\omega t) \text{ and } u_h = \ddot{h} = \omega^2 Hb \cos(\omega t + \phi) \tag{5.5}$$

5.2 Averaging of the Beddoes-Leishman model

Plugging in the definitions of the inputs from Eq. (5.5) and referring to the scaling in Eq. (4.5), the dynamical system takes the form

$$\dot{\boldsymbol{x}}(t) = \boldsymbol{f}(\boldsymbol{x}(t)) + [A_\alpha \boldsymbol{g}_\alpha(\boldsymbol{x}(t)) \cos(\omega t) + Hb\boldsymbol{g}_h(\boldsymbol{x}(t)) \cos(\omega t + \phi)] \tag{5.6}$$

As a high-frequency, high-amplitude, time-periodic system, Eq. (5.6) is not amenable to direct averaging [46]. Besides, since the cosine signal has zero mean, the typical averaging procedure would neglect the effect of the pitching-plunging oscillations. Thus, a more rigorous averaging technique is required, such as the one presented in Section 3.3, which is

particularly fitting for this problem.

The application of the Variation of Constants formula to the system in Eq. (5.2) leads to the average dynamics

$$\frac{d}{dt}\begin{pmatrix} \overline{x}_1 \\ \overline{x}_2 \\ \overline{x}_3 \\ \overline{x}_4 \\ \overline{x}_9 \\ \overline{x}_{10} \\ \overline{x}_{11} \\ \overline{\alpha} \\ \dot{\overline{\alpha}} \\ \dot{\overline{h}} \end{pmatrix} = \begin{pmatrix} -b_1\left(\frac{\beta^2 U}{b}\right)\overline{x}_1 + \overline{\alpha} + \arctan\left(\frac{\dot{\overline{h}}}{U}\right) + \frac{\dot{\overline{\alpha}} b}{U} \\ -b_2\left(\frac{\beta^2 U}{b}\right)\overline{x}_2 + \overline{\alpha} + \arctan\left(\frac{\dot{\overline{h}}}{U}\right) + \frac{\dot{\overline{\alpha}} b}{U} \\ -\frac{\overline{x}_3}{K_\alpha T_I} + \overline{\alpha} + \arctan\left(\frac{\dot{\overline{h}}}{U}\right) \\ -\frac{\overline{x}_4}{K_q T_I} + \frac{2\dot{\overline{\alpha}} b}{U} \\ \frac{U/b}{T_P}\left[C_{N_\alpha}\overline{\alpha}_E - \frac{1}{MT_I}\left(\frac{4\overline{x}_3}{K_\alpha} + \frac{\overline{x}_4}{K_q}\right) - \overline{x}_9 + \frac{4\left(\overline{\alpha} + \arctan\left(\frac{\dot{\overline{h}}}{U}\right)\right)}{M} + \frac{2\dot{\overline{\alpha}} b}{UM}\right] \\ \frac{U/b}{T_f}\left[-\overline{x}_{10} + f'\left(\frac{\overline{x}_9}{C_{N_\alpha}}\right)\right] \\ \frac{U/b}{T_v}\left[-\overline{x}_{11} + \dot{C}_v\right] \\ \dot{\overline{\alpha}} \\ 0 \\ 0 \end{pmatrix} + \begin{pmatrix} \overline{\mathcal{G}}_1(\overline{\boldsymbol{x}}) \\ \overline{\mathcal{G}}_2(\overline{\boldsymbol{x}}) \\ \overline{\mathcal{G}}_3(\overline{\boldsymbol{x}}) \\ 0 \\ \overline{\mathcal{G}}_5(\overline{\boldsymbol{x}}) \\ 0 \\ 0 \\ 0 \\ 0 \\ 0 \end{pmatrix} + \mathcal{O}\left(\epsilon^3\right) \tag{5.7}$$

where the infinite series of the pullback (Eq. (3.10)) is truncated after order $\mathcal{O}(\epsilon^2)$. $\overline{\mathcal{G}}_i$ denotes the i component of the vector $\overline{\boldsymbol{\mathcal{G}}}$, which depends on the states of the system. The indicated entries are the only components of $\overline{\boldsymbol{\mathcal{G}}}$ that don't vanish after performing the proposed

averaging analysis, and their values are

$$
\begin{aligned}
\overline{\mathcal{G}}_1 &= -\frac{HUb\omega}{2\left(U^2+\overline{\dot{h}}^2\right)^2}\left[2\left(U^2+\overline{\dot{h}}^2\right)\sin\phi + Hb\overline{\dot{h}}\omega\left(1+2\sin^2\phi\right)\right] \\
\overline{\mathcal{G}}_2 &= -\frac{HUb\omega}{2\left(U^2+\overline{\dot{h}}^2\right)^2}\left[2\left(U^2+\overline{\dot{h}}^2\right)\sin\phi + Hb\overline{\dot{h}}\omega\left(1+2\sin^2\phi\right)\right] \\
\overline{\mathcal{G}}_3 &= -\frac{HUb\omega}{2\left(U^2+\overline{\dot{h}}^2\right)^2}\left[2\left(U^2+\overline{\dot{h}}^2\right)\sin\phi + Hb\overline{\dot{h}}\omega\left(1+2\sin^2\phi\right)\right] \\
\overline{\mathcal{G}}_5 &= -\frac{2HU^2\omega}{MT_p\left(U^2+\overline{\dot{h}}^2\right)^2}\left[2\left(U^2+\overline{\dot{h}}^2\right)\sin\phi + Hb\overline{\dot{h}}\omega\left(1+2\sin^2\phi\right)\right]
\end{aligned}
\tag{5.8}
$$

The averaging theorem relates the properties of a nonlinear time-periodic system, such as Eq. (5.2), to those of its average dynamics. In other words, stability of some periodic orbit solution of the original nonlinear dynamical system may be inferred from the stability properties of the corresponding equilibrium points of the averaged system in Eq. (5.7). Its equilibrium is obtained by setting the left hand side to zero, and solving for the fixed point $\boldsymbol{x}^*$ that satisfies the equation

$$
\mathbf{0} = \boldsymbol{f}\left(\boldsymbol{x}^*\right) + \overline{\boldsymbol{\mathcal{G}}}\left(\boldsymbol{x}^*\right) \tag{5.9}
$$

The last two equations of the average dynamics in Eq. (5.7) imply that the equilibrium of the states $\dot{\alpha}$ and $\dot{h}$ is automatically satisfied, and the $\overline{\alpha}$ equation indicates that $\dot{\alpha}^* = 0$. Taking the averaged plunging speed $\dot{h}^*$ to be zero (otherwise, there will be a net drift upward or downward, which is non-physical) but keeping α^* at an arbitrary value to study the effect of the mean angle of attack on the results, the following equilibrium values for the internal

aerodynamic states are obtained

$$\begin{aligned} x_1^* &= \frac{b}{b_1 \beta^2 U} \left(\alpha^* - Hk \sin\phi\right) \\ x_2^* &= \frac{b}{b_2 \beta^2 U} \left(\alpha^* - Hk \sin\phi\right) \\ x_3^* &= K_\alpha T_I \left(\alpha^* - Hk \sin\phi\right) \\ x_4^* &= 0 \\ x_9^* &= C_{N_\alpha} \left(\alpha^* - Hk \sin\phi\right) \\ x_{10}^* &= x_0 \left(\alpha^* - Hk \sin\phi\right) \\ x_{11}^* &= \dot{C}_v^* \end{aligned} \tag{5.10}$$

where the results have been simplified with the definition of the reduced frequency $k = \frac{\omega b}{U}$.

The equilibrium $\boldsymbol{x}^*$ of the average dynamics affects the average value of the lift and drag force coefficients. However, since the force coefficients are not linearly dependent on the states, their average are not simply $C_L(\boldsymbol{x}^*)$ and $C_D(\boldsymbol{x}^*)$. Instead, each state is approximated with the first order expression $x_i(t) = x_i^* + A_{x_i} \cos(\omega t + \phi_i)$, and substituted into a multi-variable Taylor series expansion of the lift and drag coefficients around $\boldsymbol{x}^*$

$$\begin{aligned} y_m &= \sum_{n_1=0}^{\infty} \cdots \sum_{n_d=0}^{\infty} \frac{\left(x_1 - x_1^*\right)^{n_1} \ldots \left(x_d - x_d^*\right)^{n_d}}{n_1! \ldots n_d!} \left(\frac{\partial^{n_1+\cdots+n_d} y_m}{\partial x_1^{n_1} \ldots \partial x_d^{n_d}} \right) (\boldsymbol{x}^*) \\ &= y_m(\boldsymbol{x}^*) + \sum_{i=1}^{n+5} \frac{\partial y_m(\boldsymbol{x}^*)}{\partial x_i} \left(x_i - x_i^*\right) + \frac{1}{2!} \sum_{i=1}^{n+5} \sum_{q=1}^{n+5} \frac{\partial^2 y_m(\boldsymbol{x}^*)}{\partial x_i \partial x_q} \left(x_i - x_i^*\right) \left(x_q - x_q^*\right) + \ldots \end{aligned} \tag{5.11}$$

where $y_m(\boldsymbol{x}), m \in (C_L, C_D)$. Finally, the average of the outputs over a cycle of motion of the inputs is

$$\overline{y}_m = \frac{1}{T} \int_0^T y_m(t) dt \tag{5.12}$$

5.2.1 Average lift coefficient

The average of the lift coefficient over one cycle of motion is found to be

$$\overline{C}_L = \frac{C_{N_\alpha}}{2}\left(\alpha^* - Hk\sin\phi\right)\left[\frac{\left(1+\sqrt{x_0^*}\right)^2}{2}\cos\alpha^* + 2\eta\left(\alpha^* - Hk\sin\phi\right)\sqrt{x_0^*}\sin\alpha^*\right]$$
$$+\dot{C}_v^*\cos\alpha^* - \frac{A_\alpha^2}{4}\left\{\frac{C_{N_\alpha}\alpha^*}{2}\left[\frac{\left(1+\sqrt{x_0^*}\right)^2}{2}\cos\alpha^* + 2\eta\alpha^*\sqrt{x_0^*}\sin\alpha^*\right] + \dot{C}_v^*\cos\alpha^* + \frac{8\sin\alpha^*}{M}\right\}$$
$$+\frac{2A_\alpha Hk}{M}\sin\alpha^*\sin\phi + \mathcal{O}\left(\epsilon^3\right) \quad (5.13)$$

with the infinite series being truncated at the order $\mathcal{O}\left(\epsilon^2\right)$. The average lift coefficient is a function of the mean angle of attack α^*, the motion parameters (reduced frequency k and pitching and plunging amplitudes A_α and H, respectively), and the airfoil characteristics. There is also a dependency on the equilibrium values of the average dynamics of the states $x_{10}^* = x_0^*$ and $x_{11}^* = \dot{C}_v^*$, listed in Eq. (5.10). The equilibrium state x_{10}^* is the point of separation evaluated at an equivalent angle of attack $(\alpha^* - Hbk\sin\phi)$, and it can be directly calculated with Eq. (2.76).

The equilibrium state $x_{11}^* = \dot{C}_v^*$ represents the mean value of the time derivative of Eq. (2.83), which is obtained by numerical simulation of the Beddoes-Leishman model at different combinations of A_α, H, and k. These data are then used to mathematically represent the relation $\dot{C}_v^* = \dot{C}_v^*\left(\alpha^*, A_\alpha, H, k, M\right)$ in a smooth way.

The analytical expression of the average lift coefficient in Eq. (5.13) permits a distillation of the role of each variable in the generation of lift. In fact, one might expect the average lift coefficient $\overline{C}_L$ to be equal to the steady lift coefficient evaluated at the mean angle of attack α^*. However, Eq. (5.13) uncovers more complex force due to behind the oscillatory motion of the airfoil. The first line of the equation is simply the expression of the lift coefficient given by the Beddoes-Leishman model evaluated at the equilibrium points of the averaged

dynamics; the first term in brackets is the projection of the normal force coefficient given by Kirchhoff's model in the direction perpendicular to the free stream, and the second term in brackets is the projection of the chord force. Both expressions account for the effect of trailing edge separation. In fact, these two terms in the first line present the average lift coefficient if direct averaging were to be performed on the system without accounting for higher-order effects. Roughly speaking, a deviation of $\overline{C}_L$ from this term may indicate lift enhancement or deficiency and, in essence, the appearance of the symmetry breaking phenomenon. In the following discussion the two terms in the first line are referred to as the effects of the normal and the tangential forces, respectively.

The second line in Eq. (5.13) lists two contributions. The first one indicates a clear dependence of the average lift force on the strength of the leading-edge vortex represented by $\dot{C}_v^*$, which is one of the key parameters capturing dynamic stall in the Beddoes-Leishman model. As such, this term implies that the circulation of the leading-edge vortex, which only forms in unsteady conditions, generates a net resulting force even when the airfoil motion is harmonic with zero-mean, and plays a role in breaking symmetry and shifting the average lift force from the steady value. However, given its high dependence on the mean angle of attack and the motion parameters, its contribution to $\overline{C}_L$ can be positive or negative depending on the flight conditions, inducing either lift enhancement or deficiency, respectively.

The second contribution groups all the terms that depend explicitly on the pitching motion. The first and second terms are the projections of the normal and the chord forces in the direction perpendicular to the free stream, and they account for the effect of trailing edge separation. Given their positive nature, the role of these terms through the pitching motion is to decrease the average lift coefficient. However, the third term in brackets lists the contribution of the leading-edge vortex due to the pitching motion, and it may take positive or negative values. As such, it may generate a force that increases or decreases $\overline{C}_L$ as a function of the angle of attack and the flight conditions. Lastly, the fourth term in brackets

represents the effect of the Mach number on the average lift coefficient, which hints at a decrease in the lift force that is attenuated as the Mach number increases. Due to its non-circulatory nature, this term can also be understood as an expression of the added mass effects. Nonetheless, since $\dot{C}_v^*$ also depends on M, the dependence of the average lift coefficient on the free stream Mach number is more complex than the term suggests.

Finally, the third and last line in Eq. (5.13) reveals the effect of the interaction between the pitching and plunging motions. The contribution of this combination is unimportant when both movements are in phase. However, the expression suggests a lift enhancement mechanism when the pitching motion lags behind the plunging displacement, and lift deficiency when the motion is otherwise. This interactive mechanism diminishes as compressibility effects become more important.

Eq. (5.13) does not contain any terms that depend solely and directly on the amplitude of the plunging motion, as some terms do on A_α. Nonetheless, the influence of the plunging speed on the average lift coefficient occurs through the leading-edge vortex $\dot{C}_v^*$, whose value is determined by A_α, H, k, and the Mach number M. Thus, the effect of the pitching and plunging motions on the average lift coefficient is highly determined by their influence on the rate of change of the leading-edge vortex strength, which is one of the key parameters in the study of dynamic stall behavior.

Before studying the effects of unsteadiness in the lift and drag coefficients, it is necessary to understand their behavior under steady conditions. Fig. 5.1 shows the steady C_L and C_D as a function of the angle of attack for a NACA 0012 airfoil at $Re = 500,000$. For this conventional airfoil, the steady lift coefficient increases linearly at low angles of attack until we reach the stall angle (approximately 15°), where lift decreases again until it reaches a minimum point at around 20°. After this trough, lift keeps increasing at a lower rate reaching another maximum at 42°. On the other hand, at low angles of attack, the drag coefficient increases slowly with α. However, there is a sudden raise in $C_{D,s}$ at stall. At higher angles of

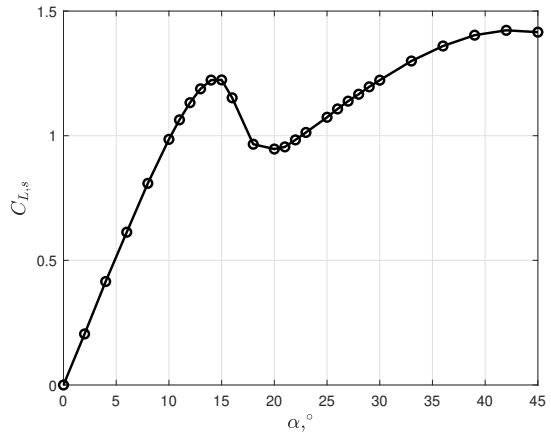

(a) Steady lift coefficient vs. angle of attack

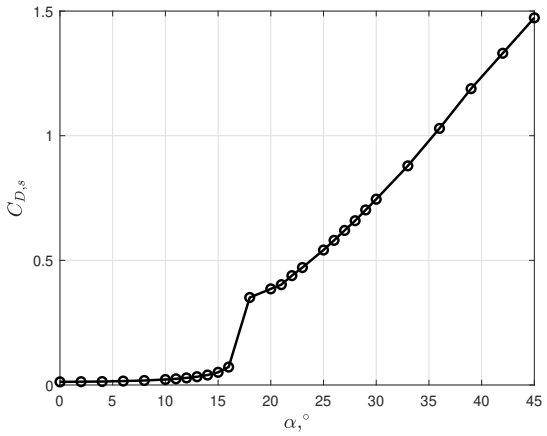

(b) Steady lift coefficient vs. angle of attack

Figure 5.1: Steady lift and drag coefficients as a function of the angle of attack for a NACA 0012 airfoil at $Re = 500,000$.

attack, the steady drag coefficient keeps increasing significantly. The results presented in this section are performed on the presented NACA 0012 airfoil. The conclusions are believed to be analogous for other conventional airfoils. Delta wings and other unconventional airfoils, which are outside of the scope of this work, may present dissimilar results.

Fig. 5.2 shows the value of each of the terms in Eq. (5.13) when compared to their counterparts under steady conditions for a NACA 0012 airfoil pitching with an amplitude of $A_\alpha = 5^\circ$ at a reduced frequency of $k = 0.5$ for different mean angles of attack and Mach numbers. To do this comparison, the static values have been subtracted from the corresponding terms in Eq. (5.13) and normalized by the maximum value of $\dot{C}_v^*$ at the amplitude of study, $A_\alpha = 5^\circ$. At low Mach numbers, the resulting unsteady lift coefficient seems to be dominated by the added mass term (solid blue line), showing the effects of the Mach number, and whose magnitude increases with the mean angle of attack. This contribution actually results in a decrease in $\overline{C}_L$, which diminishes as the Mach number increases. The second most dominant contribution is due to the leading-edge vortex through $\dot{C}_v^*$ (solid orange line), which becomes more pronounced at higher M. This term contributes positively to the average lift force when oscillating about mean angles of attack close to the stall angle ($\alpha^* = 15^\circ$). In

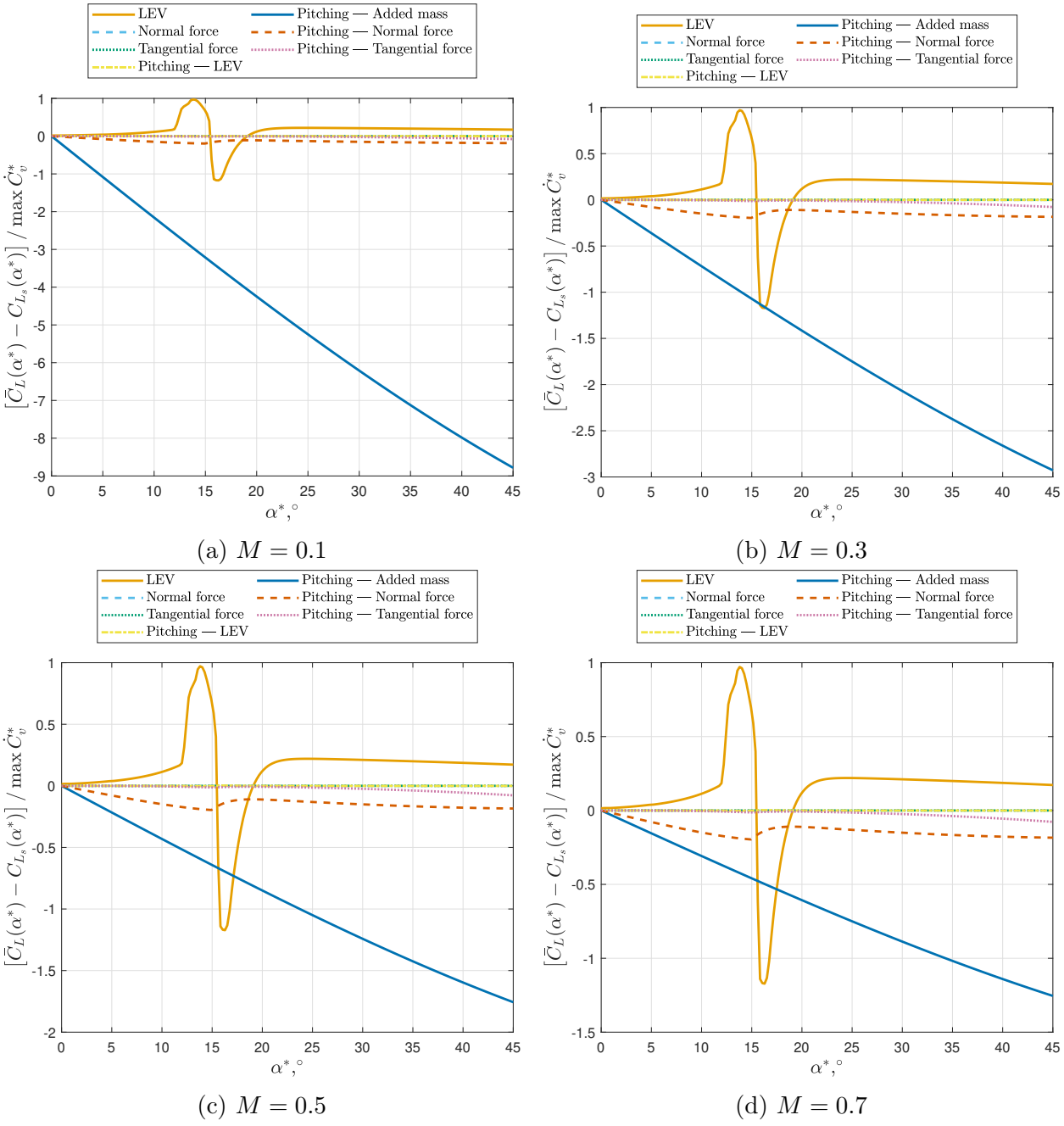

(a) $M = 0.1$ (b) $M = 0.3$

(c) $M = 0.5$ (d) $M = 0.7$

Figure 5.2: Terms of the average lift coefficient $\overline{C}_L$ minus the same terms for static conditions vs. mean angle of attack α^* for a pitching amplitude of $A_\alpha = 5°$ and a reduced frequency of $k = 0.5$ for different Mach numbers (NACA 0012 airfoil, $Re = 500,000$, $H = 0$).

fact, at high free stream Mach numbers, the positive effect of $\dot{C}_v^*$ counteracts the negative contribution of M, suggesting a lift enhancement in this regime. In contrast, oscillation around a mean angle of attack with a negative steady lift curve slope ($\alpha^* = 15° - 20°$), the leading-edge vortex has a negative impact on the average $\overline{C}_L$. Interestingly, the terms showing a direct dependence on the pitching amplitude are negligible, especially at low Mach numbers. This behavior is to be expected because these terms are proportional to the square of the pitching amplitude; and we focus here on small-amplitude oscillations. These terms, however, acquire more importance at higher Mach numbers, especially the component of the normal force (dashed red line), which results in a decrease in lift with a maximum value when oscillating at mean angles of attack slightly higher than the stall angle.

Fig. 5.3 shows the value of each of the terms in Eq. (5.13) when compared to their steady counterparts for a NACA 0012 airfoil plunging at a reduced frequency of $k = 0.5$ for different mean angles of attack and Mach numbers. The amplitude of the plunging motion is determined by the effective amplitude $A_{\alpha_{\text{eff}}} = \arctan Hk = 5°$, such that the results are comparable to those of the pitching motion. In this case, the leading-edge vortex takes a major role in the enhancement or reduction of the lift force. Similarly to the pitching case, the $\dot{C}_v^*$ term (solid orange line) suggests a positive contribution to the average lift force at mean angles of attack close to the stall angle, but a decrease in $\overline{C}_L$ when plunging at post-stall angles of attack where the steady lift curve slope is negative. In the pitching motion, however, the positive and negative contributions of the leading-edge vortex to the lift force were of similar magnitude than in the plunging motion, with the negative effect at post-stall being more pronounced than the positive one at stall. The other terms of Eq. (5.13) are negligible in the studied cases. Interestingly, no considerable dependence on the Mach number is observed in the case of plunging, in contrast to pitching.

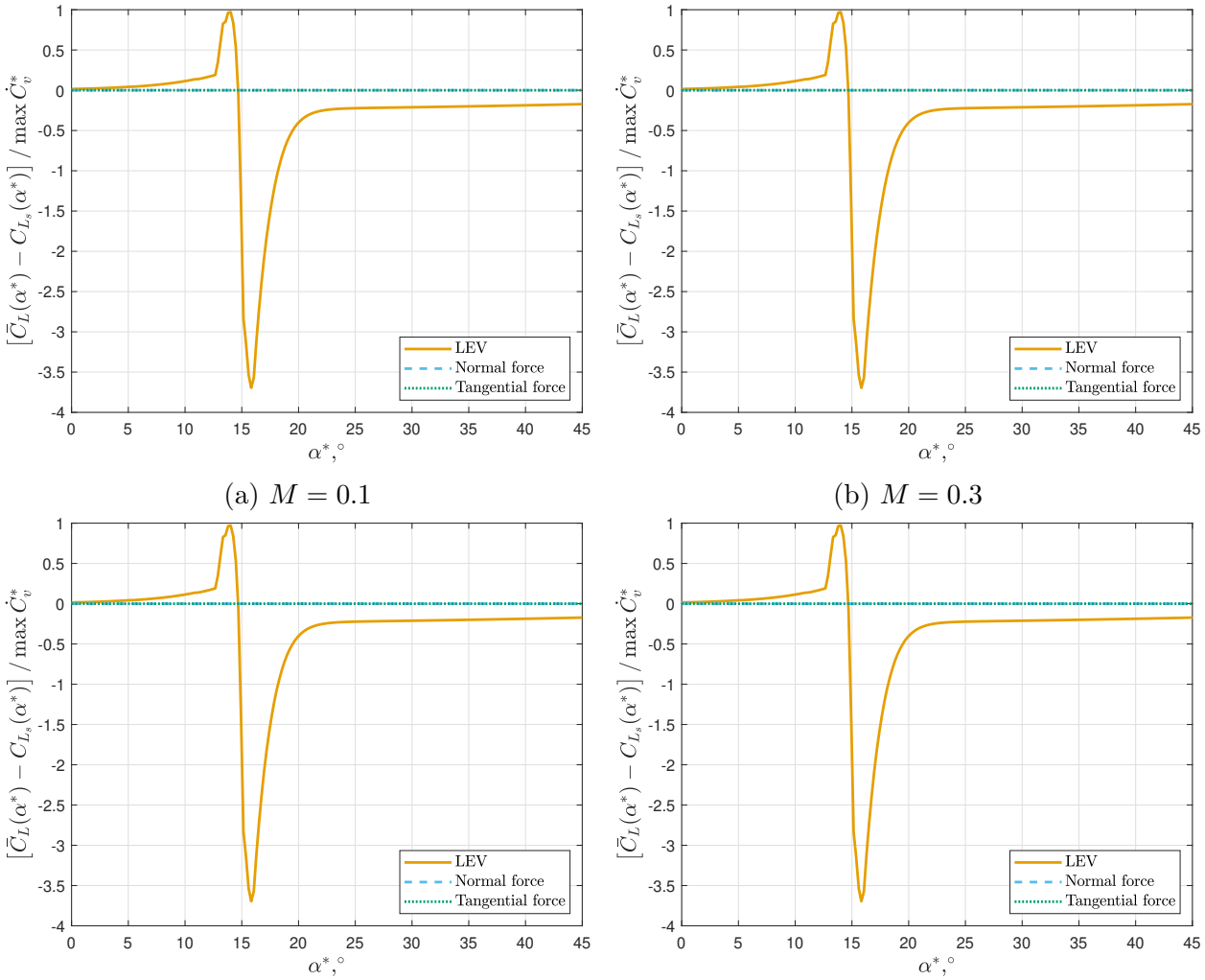

(a) $M = 0.1$

(b) $M = 0.3$

(c) $M = 0.5$

(d) $M = 0.7$

Figure 5.3: Terms of the average lift coefficient $\overline{C}_L$ minus the same terms for static conditions vs. mean angle of attack α^* for a plunging motion of effective amplitude $A_{\alpha,eff} = \arctan Hk = 5^\circ$ and a reduced frequency of $k = 0.5$ for different Mach numbers (NACA 0012 airfoil, $Re = 500,000$, $A_\alpha = 0^\circ$).

5.2.2 Average drag coefficient

The average of the drag coefficient over one cycle of motion is derived to be

$$\overline{C}_D(\alpha^*) = \frac{C_{N_\alpha}}{2}(\alpha^* - Hk\sin\phi)\left[\frac{\left(1+\sqrt{x_0^*}\right)^2}{2}\sin\alpha^* - 2\eta(\alpha^* - Hk\sin\phi)\sqrt{x_0^*}\cos\alpha^*\right]$$
$$+\dot{C}_v^*\sin\alpha^* - \frac{A_\alpha^2}{4}\left\{\frac{C_{N_\alpha}\alpha^*}{2}\left[\frac{\left(1+\sqrt{x_0^*}\right)^2}{2}\sin\alpha^* - 2\eta\alpha^*\sqrt{x_0^*}\cos\alpha^*\right] + \dot{C}_v^*\sin\alpha^* - \frac{8\cos\alpha^*}{M}\right\}$$
$$- \frac{2A_\alpha Hk}{M}\cos\alpha^*\sin\phi + \mathcal{O}\left(\epsilon^3\right) \quad (5.14)$$

with the infinite series being truncated at the order $\mathcal{O}(\epsilon^2)$.

The average unsteady drag coefficient $\overline{C}_D$ depends on the mean angle of attack α^*, the motion parameters (A_α, H, and k), the airfoil characteristics such as the slope of the normal force curve C_{N_α} and the separation point x_0^*, and the equilibrium value of the derivative of the vortex strength $\dot{C}_v^*$. Similar to the average lift coefficient, the first line in Eq. (5.14) is simply the expression of the drag coefficient as given by the Beddoes-Leishman model in Eq. (2.85) evaluated at the equilibrium points of the averaged dynamics. For instance, the first and second terms represent the components of the normal and tangential force coefficients, respectively, in the direction of the free stream. Therefore, as it occurred with the lift coefficient, roughly speaking, a deviation of $\overline{C}_D$ from this expression may entail drag reduction or augmentation as a result of unsteady motion.

The first term in the second line of Eq. (5.14) shows the effect of the leading-edge vortex on the average drag coefficient. However, since $\dot{C}_v^*$ is highly dependent on the mean angle of attack and the motion parameters, its net effect on the average drag force is intricate and needs some scrutiny, as demonstrated in the discussions of Fig. 5.4, 5.5 below. The next term in the second line (the bracketed terms) collects all the terms that depend directly on the amplitude of the pitching motion A_α. The last term in brackets notes the dependence

of $\overline{C}_D$ on the Mach number through added mass effects, which decreases as compressibility effects become more important. Interestingly, some of the terms in brackets contribute to a reduction in the drag force, hinting at a possible thrust generation mechanism.

Lastly, the final line of Eq. (5.14) shows the impact of the combination of both pitching and plunging motions, which also vanishes if both oscillations are in phase. Of particular interest is the case when the plunging motion lags behind the pitching oscillations; in this case, the interactive term becomes negative, pointing to a possible drag reduction mechanism. However, the effect of this interactive mechanism decreases as the Mach number increases.

As it occurred with $\overline{C}_L$, the average drag coefficient does not contain any terms that depend solely and explicitly on the plunging amplitude. However, the dependence of $\overline{C}_D$ on the plunging motion takes place through the average value of the leading-edge vortex strength $\dot{C}_v^*$, which heavily depends on the motion parameters A_α, H and k, as well as the Mach number M. Fig. 5.4 shows the value of each of the terms in Eq. (5.14) in comparison to their steady counterparts for a NACA 0012 airfoil pitching with an amplitude of $A_\alpha = 5°$ at a reduced frequency of $k = 0.5$ for different mean angles of attack and Mach numbers. As it occurred with the lift coefficient, the added mass term (solid blue line) dominates over the others. However, contrary to $\overline{C}_L$, even though this contribution decreases with M, its effect is prevalent even at the highest Mach numbers. This relevance implies an increase of the drag force in all flight conditions, although this increment is lower when pitching at higher angles of attack. Nonetheless, Fig. 5.4 also shows a decrease in the drag force due to a negative contribution of the leading-edge vortex decreasing the drag force when oscillating at angles of attack in the post-stall regime. Similarly, the normal force contributes negatively to $\overline{C}_D$ as the airfoil pitches at higher α^*. However, such effects are negligible when compared to the added mass term.

Fig. 5.5 shows the value of each of the terms in Eq. (5.14) when compared to the same terms under steady conditions for a NACA 0012 airfoil plunging at a reduced frequency of $k = 0.5$

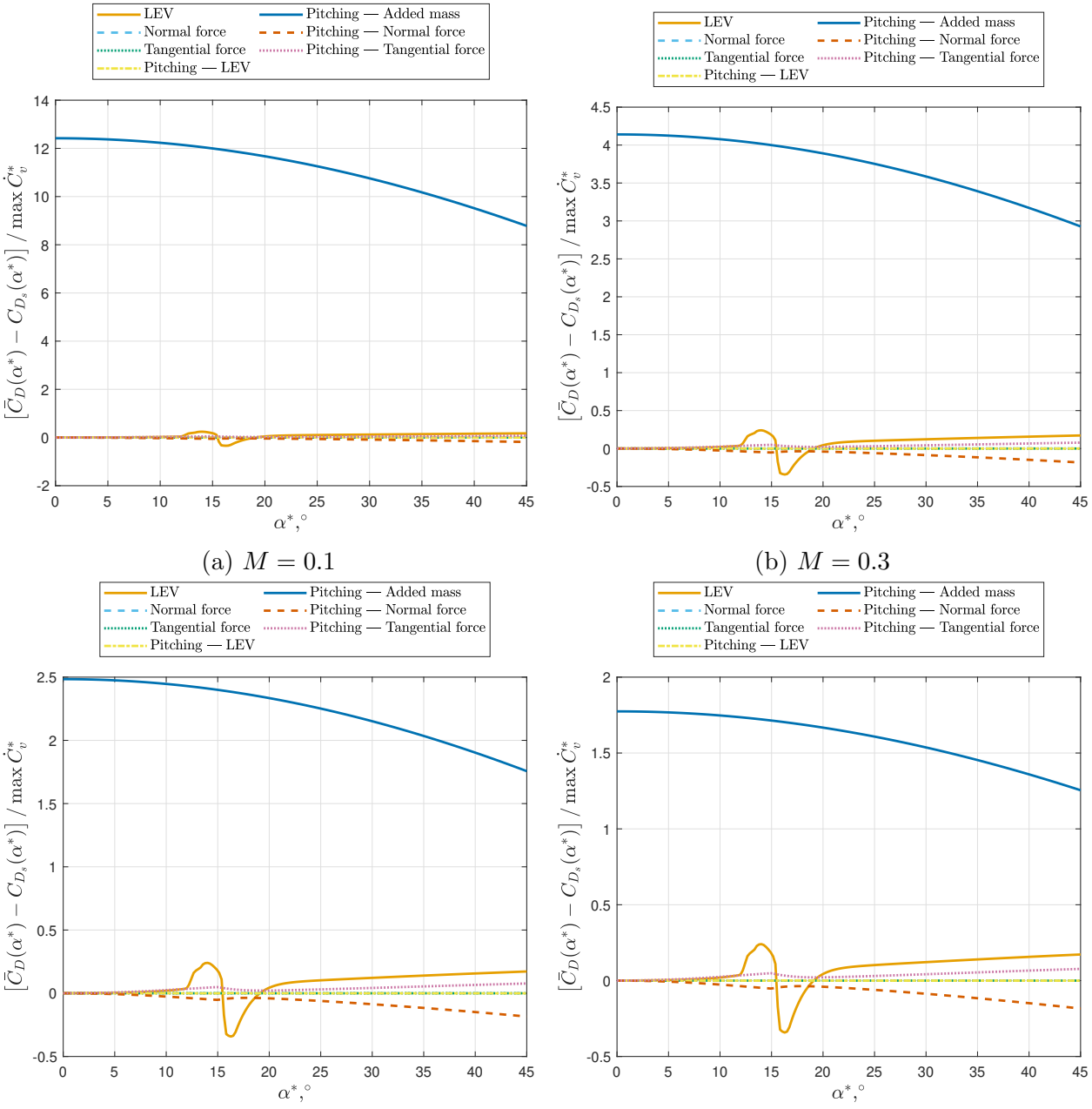

(a) $M = 0.1$ (b) $M = 0.3$

(c) $M = 0.5$ (d) $M = 0.7$

Figure 5.4: Terms of the average drag coefficient $\overline{C}_D$ minus the same terms for static conditions vs. mean angle of attack α^* for a pitching amplitude of $A_\alpha = 5°$ and a reduced frequency of $k = 0.5$ for different Mach numbers (NACA 0012 airfoil, $Re = 500,000$, $H = 0$).

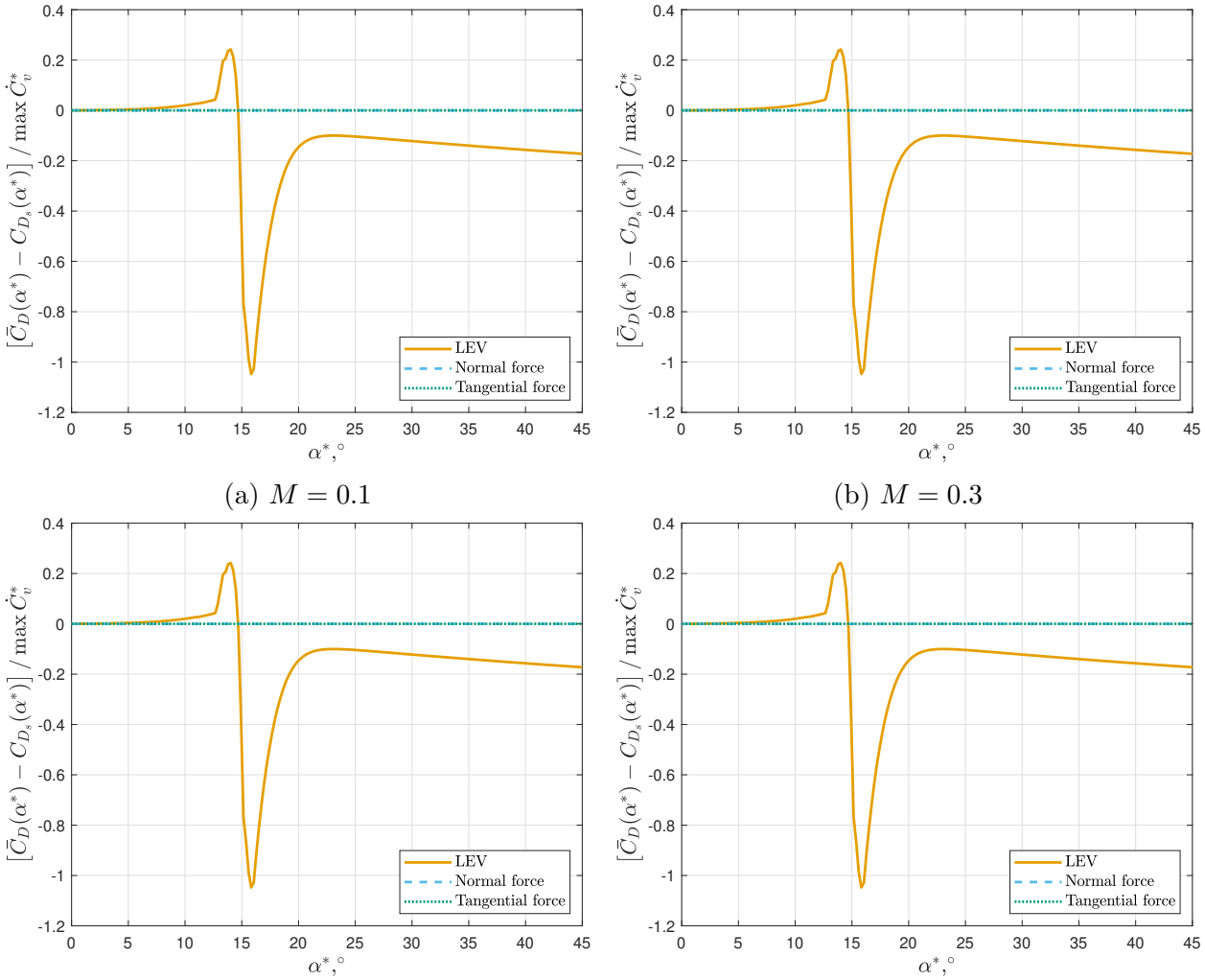

(a) $M = 0.1$ (b) $M = 0.3$

(c) $M = 0.5$ (d) $M = 0.7$

Figure 5.5: Terms of the average drag coefficient $\overline{C}_D$ minus the same terms for static conditions vs. mean angle of attack α^* for a plunging motion with an effective amplitude $A_{\alpha,eff} = \arctan Hk = 5^\circ$ and a reduced frequency of $k = 0.5$ for different Mach numbers (NACA 0012 airfoil, $Re = 500,000$, $A_\alpha = 0^\circ$).

with an effective amplitude of $A_{\alpha_{\text{eff}}} = \arctan Hk = 5^\circ$ for different mean angles of attack and Mach numbers. Similar to the lift coefficient, in the case of the plunging motion the leading-edge vortex seems to be the dominant factor in controlling the average drag coefficient. In fact, the depicted trends are similar to the lift case, which indicates that lift and drag are just two components of the resultant aerodynamic force. Drag increases right before stall, and decreases between the stall angle and the trough of the steady lift curve, with the drag reduction being more pronounced than the increase. As shown for $\overline{C}_L$, this increase and decline in the drag coefficient is not considerably dependent on the Mach number. The rest of the terms in Eq. (5.14) are also negligible, as they were for the lift coefficient.

Chapter 6

Surging-induced symmetry breaking

The previous chapters studied the effect of pitching and plunging oscillations on a wing, uncovering force generation mechanisms that intensify and reduce the aerodynamic forces. However, these motions are by some means equivalent; both pitching and plunging induce a change in the effective angle of attack of the wing. Therefore, one might expect the enhancement or deficiency to be governed by the same parameter in both cases; as derived in previous chapters, the curvature of the steady lift curve in low-Reynolds unsteady applications, and the leading-edge vortex (LEV) in dynamic stall.

The present chapter investigates the effect of the surging motion on an oscillating wing. This motion, of different nature when compared to pitching-plunging oscillations, might present different force enhancement and reduction characteristics than those obtained for a pitching-plunging wing. The study of low-amplitude, high-frequency surging oscillations is performed by extending the reduced-order model (ROM) in Section 2.3.2 to include a surging input. The model is then analyzed with a combination of averaging and geometric control theory to find the average unsteady lift and drag forces on the wing. The comparison of the resulting mean unsteady forces with their steady counterparts may uncover the appearance of force

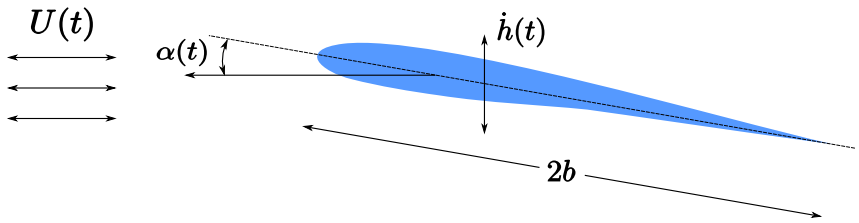

Figure 6.1: Schematic diagram of a pitching-plunging airfoil in a time-varying free stream.

enhancement or reduction mechanisms prompted by the surging motion. Finally, the average forces are further studied to reveal the causes behind these force generation mechanisms.

6.1 Problem statement

The current chapter is concerned with a problem similar to that presented in Section 4.1, which introduced a ROM for a pitching and plunging wing in a constant free stream. Similarly, in this case the wing of study is also pitching and plunging. However, the wing is in a time-varying free stream or, equivalently, the wing moves back and forth following the surging motion presented in Fig. 6.1.

The objective is the definition of a physics-based dynamical system capable of representing the unsteady lift and drag forces over the airfoil. The model needs to be sufficiently rich to capture the main physical aspects of the flow, including the nonlinearities of unsteady flows, but also compact to permit a geometric control analysis. The model in Section 2.3.2 was developed following these characteristics. As such, the ROM presented in this chapter builds upon the work introduced in the aforementioned section. The dynamical system of a pitching-plunging-surging wing will be derived to take the following form

$$\begin{aligned} \dot{\boldsymbol{x}}(t) &= \boldsymbol{f}(\boldsymbol{x}(t)) + \boldsymbol{g}_\alpha(\boldsymbol{x}(t))\ddot{\alpha}(t) + \boldsymbol{g}_h(\boldsymbol{x}(t))\ddot{h}(t) + \boldsymbol{g}_U(\boldsymbol{x}(t))\dot{U}(t) \\ \boldsymbol{y}(t) &= [L(t) \quad \mathcal{D}(t)]^T \end{aligned} \tag{6.1}$$

where $\boldsymbol{x}$ is the vector containing all the states of the system, and $\boldsymbol{y}$ is the vector of output variables; in this case, the lift and drag forces. The vectors $\boldsymbol{g}_\alpha$, $\boldsymbol{g}_h$ and $\boldsymbol{g}_U$ are the control vector fields associated with the pitching, plunging and surging inputs. The control inputs of the system are $\ddot{\alpha}$, $\ddot{h}$ and $\dot{U}$, the pitching, plunging and surging accelerations, respectively.

6.2 System development

The present section follows the derivation of the ROM presented in Section 2.3.2 but accounting for a time-varying free stream velocity U. The formulation is changed, when needed, to add the surging effect on the wing to the dynamical representation of the lift force. The dynamics of the drag force are represented by the same output equation and do not require new formulation.

6.2.1 Circulatory lift

Although Section 2.3.2 is concerned with a wing in a constant free stream, the dynamics of the circulatory lift are derived for a time-varying free stream to develop a model for any arbitrary wing motion ($\alpha(t)$, $h(t)$, $U(t)$). As such, the dynamics of the circulatory lift for a pitching-plunging wing in a time-varying free stream are defined by

$$\begin{aligned} \dot{\boldsymbol{x}}_C(t) &= [\boldsymbol{A}]_{nxn} U(t) \boldsymbol{x}_c(t) + [\boldsymbol{B}]_{nx1} U(t) \Gamma_0(t) \\ L_C(t) &= \rho U(t) \left([\boldsymbol{C}]_{1xn} \boldsymbol{x}_c(t) + [D]_{1x1} \Gamma_0(t) \right) \end{aligned} \tag{6.2}$$

where $\boldsymbol{x}_c \in \mathbb{R}^n$ represents all the internal aerodynamic states that model the lift dynamics, and the matrices $\boldsymbol{A}$, $\boldsymbol{B}$ and $\boldsymbol{C}$ depend on the characteristics of the wing and the flow. The parameter $D = k_{hf}$ is the high-frequency gain of the system (the magnitude of the output at infinite frequency, the instantaneous response of the system), and the quasi-steady

circulation Γ_0 is the input of the system.

The resulting circulatory dynamics are similar to those presented in the final ROM of Section 2.3.2. However, in that model, since the free stream does change with time, the $U(t)$ terms multiplying the coefficients of $\dot{\boldsymbol{x}}_C$ in Eq. (6.2) are absorbed into the $\boldsymbol{A}$ and $\boldsymbol{B}$ matrices. In this surging model, $U(t)$ is separated from these coefficients to show the dependence of $\dot{\boldsymbol{x}}_C$ on the time-varying state U.

6.2.2 Non-circulatory lift

Although the non-circulatory lift is classically represented by an arithmetic multiplication of a virtual mass and the normal acceleration of the wing at the mid-point, Section 2.3.2 defines this lift contribution using the state x_v. This formulation accounts for the phase lag between the normal acceleration and the non-circulatory lift induced by viscosity effects. As such, the dynamics of the non-circulatory lift are described by the system

$$\begin{aligned} \dot{x}_v(t) &= -\frac{x_v(t)}{\tau_v} + \frac{a_{\perp_{1/2}}(t)}{\tau_v} \\ L_{NC}(t) &= m_v x_v(t) \cos\alpha(t) \end{aligned} \tag{6.3}$$

where τ_v is the time constant governing the dynamics of the non-circulatory lift.

6.2.3 Reduced-order model for a pitching-plunging-surging wing

The dynamical representation of a pitching-plunging-surging wing is constructed with the combination of the systems derived in the previous sections. The final resulting system for

a pitching-plunging-surging wing is given by

$$\frac{d}{dt}\begin{pmatrix} \boldsymbol{x}_c \\ x_v \\ x_s \\ \alpha \\ \dot{\alpha} \\ \dot{h} \\ U \end{pmatrix} = \begin{pmatrix} \boldsymbol{A}U\boldsymbol{x}_c + \boldsymbol{B}U\Gamma_0\left(\alpha, \dot{\alpha}, \dot{h}, U\right) \\ -\frac{1}{\tau_v}\left[x_v - \left(U(t)\cos\alpha - \dot{h}(t)\sin\alpha\right)\dot{\alpha}\right] \\ -\frac{1}{\tau_1}\left[x_s - x_0\left(\alpha + \arctan\frac{\dot{h}}{U} - \tau_2\dot{\alpha}\right)\right] \\ \dot{\alpha} \\ \dot{\alpha} \\ 0 \\ 0 \\ 0 \end{pmatrix} + \begin{pmatrix} \mathbf{0}_{nx1} \\ -\frac{ab}{\tau_v} \\ 0 \\ 0 \\ 1 \\ 0 \\ 0 \end{pmatrix}\ddot{\alpha} + \begin{pmatrix} \mathbf{0}_{nx1} \\ \frac{\cos\alpha}{\tau_v} \\ 0 \\ 0 \\ 0 \\ 1 \\ 0 \end{pmatrix}\ddot{h} + \begin{pmatrix} \mathbf{0}_{nx1} \\ \frac{\sin\alpha}{\tau_v} \\ 0 \\ 0 \\ 0 \\ 0 \\ 1 \end{pmatrix}\dot{U} \tag{6.4}$$

where the indication of time dependence on $\alpha(t)$, $h(t)$, $U(t)$ and their derivatives has been dropped for clarity. The model is similar to the originally derived ROM of Section 2.3.2, but includes an input for the surging motion. This model defines the state x_s for the point of separation, as the previous model did. The calculation of the average unsteady point of separation is outside the scope of this work and will not be included in the results. However, the state is kept in the calculations to exemplify the possible calculation of the mean dynamics of x_s.

6.2.4 Inputs

The inputs of the system are assumed to be high-frequency, small-amplitude oscillations at arbitrary angles of attack. The pitching angle α (positive pitching up), the plunging

displacement h (positive downward), and the surging velocity U are defined by

$$\begin{aligned} \alpha &= \alpha^* - A_\alpha \cos(\omega t) \\ h &= Hb \cos(\omega t + \phi) \\ U &= U^* (1 - \sigma \cos(\omega t + \phi_U)) \end{aligned} \tag{6.5}$$

where ω is the oscillation frequency, α^* is the mean pitching angle, H is the amplitude of the plunging displacement normalized by the half-chord length b, and σ is the amplitude of the surging motion normalized by the mean free stream velocity U^*. The angles ϕ and ϕ_U represent the phase difference between the pitching and plunging motions, and the pitching and surging motions, respectively. Since the inputs of the system are the accelerations, they are obtained by differentiating Eq. (6.5) twice

$$\begin{aligned} u_\alpha &= \ddot{\alpha} = \omega^2 A_\alpha \cos(\omega t) \\ u_h &= \ddot{h} = \omega^2 Hb \cos(\omega t + \phi) \\ u_U &= \dot{U} = -\omega U^* \sigma \sin(\omega t + \phi_U) \end{aligned} \tag{6.6}$$

In the case of the pitching and plunging motions, the input is given by the second derivative of the motion. However, for the surging motion, the input is defined by the first derivative of the motion. Consequently, even though the pitching and plunging inputs are determined by a cosine function, the surging motion is described with a sine function, which is equivalent to a cosine function with a phase shift. The order of the inputs is the same for all three motions

$$\begin{aligned} u_\alpha &= \omega^2 A_\alpha = \mathcal{O}\left(\frac{1}{\epsilon^2}\epsilon\right) = \mathcal{O}\left(\frac{1}{\epsilon}\right) \\ u_h &= \omega^2 Hb = \mathcal{O}\left(\frac{1}{\epsilon^2}\epsilon\right) = \mathcal{O}\left(\frac{1}{\epsilon}\right) \\ u_U &= \dot{U} = \omega U^* \sigma = \mathcal{O}\left(\frac{1}{\epsilon}\frac{1}{\epsilon}\epsilon\right) = \mathcal{O}\left(\frac{1}{\epsilon}\right) \end{aligned} \tag{6.7}$$

Consequently, the definition of the surging motion should be adequate for a geometric control analysis of the model.

6.2.5 Outputs

The outputs of the system are the lift and drag forces, as defined in Section 2.3.2

$$\begin{aligned} L(t) &= \Psi_L\left(\boldsymbol{x}(t)\right) = \rho U\left(\boldsymbol{C}\boldsymbol{x}_c(t) + D\Gamma_0\left(\alpha, \dot{\alpha}, \dot{h}, U\right)\right) + m_v x_v(t)\cos\alpha(t) \\ D(t) &= \Psi_D\left(\boldsymbol{x}(t)\right) = L(t)\tan\alpha(t) - k_s\rho b\left(\frac{\boldsymbol{C}\boldsymbol{x}_c(t) + D\Gamma_0\left(\alpha, \dot{\alpha}, \dot{h}, U\right)}{2\pi b} - \frac{b}{2}\dot{\alpha}(t)\right)^2 \end{aligned} \tag{6.8}$$

6.3 Average dynamics

The application of averaging in combination with chronological calculus leads to the average dynamics of the system

$$\frac{d}{dt}\begin{pmatrix} \overline{\boldsymbol{x}}_c \\ \overline{x}_v \\ \overline{x}_s \\ \overline{\alpha} \\ \overline{\dot{\alpha}} \\ \overline{\dot{h}} \\ \overline{U} \end{pmatrix} = \begin{pmatrix} \boldsymbol{A}\overline{U}\overline{\boldsymbol{x}}_c + \boldsymbol{B}\overline{U}\Gamma_0\left(\overline{\alpha}, \overline{\dot{\alpha}}, \overline{\dot{h}}, \overline{U}\right) \\ -\frac{1}{\tau_v}\left[\overline{x}_v - \left(\overline{U}\cos\overline{\alpha} - \overline{\dot{h}}\sin\overline{\alpha}\right)\overline{\dot{\alpha}}\right] \\ -\frac{1}{\tau_1}\left[\overline{x}_s - x_0\left(\overline{\alpha} + \arctan\frac{\overline{\dot{h}}}{\overline{U}} - \tau_2\overline{\dot{\alpha}}\right)\right] \\ \overline{\dot{\alpha}} \\ 0 \\ 0 \\ 0 \end{pmatrix} + \begin{pmatrix} \overline{\boldsymbol{\mathcal{G}}}_{1\to n}\left(\overline{\alpha}, \overline{U}\right) \\ \overline{\mathcal{G}}_{n+1}\left(\overline{\alpha}, \overline{U}\right) \\ \overline{\mathcal{G}}_{n+2}\left(\overline{\alpha}, \overline{U}\right) \\ 0 \\ 0 \\ 0 \\ 0 \end{pmatrix} \tag{6.9}$$

where $\overline{\mathcal{G}}_i$ are the only non-zero entries of the averaged vector field $\boldsymbol{\mathcal{G}}$ and depend only on $\overline{\alpha}$ and $\overline{U}$.

The averaging theorem relates the properties of a nonlinear time-periodic system, such as the ROM (6.4), to those of its average dynamics in Eq. (6.9). In other words, stability of some periodic orbit solution of the original nonlinear dynamical system may be inferred from the stability properties of the corresponding equilibrium points of the averaged system. The equilibrium of the average dynamics of the system is obtained by setting the left-hand side of the average dynamics to zero and solving for $\boldsymbol{x}^*$ that satisfies the equation

$$\mathbf{0} = \boldsymbol{f}\left(\boldsymbol{x}^*\right) + \overline{\boldsymbol{\mathcal{G}}}\left(\boldsymbol{x}^*\right) \tag{6.10}$$

From this equation, one can infer that the equilibrium of the states $\left(\dot{\alpha}^*, \dot{h}^*, U^*\right)$ is automatically satisfied because the equations are already equal to zero. However, the $\overline{\alpha}$ equation reveals the equilibrium value of the pitching speed to be $\dot{\alpha}^* = 0$. Since the equilibrium for $\dot{h}^*$ is satisfied for any value of $\dot{h}$, calculations are simplified by setting $\dot{h}^* = 0$. The angle of attack of equilibrium α^* and the wind speed U^* are taken as arbitrary values to study their effect on the force dynamics. The equilibrium of the rest of the states of the system is given by

$$\boldsymbol{x}_c^* = -\boldsymbol{A}^{-1}\left(\overline{\boldsymbol{\mathcal{G}}}_{1\to n}\left(\alpha^*, U^*\right) + \overline{U} b C_{L,s}\left(\alpha^*\right)\boldsymbol{B}\right) \tag{6.11}$$

$$x_v = \frac{1}{\tau_v}\left(Hb\omega\cos\alpha^*\sin\phi - \sigma U^*\sin\alpha^*\cos\phi_U\right) \tag{6.12}$$

$$x_s = x_0\left(\alpha^*, U^*\right) + \tau_1\overline{\mathcal{G}}_{n+2}\left(\alpha^*, U^*\right) \tag{6.13}$$

The equilibrium $\boldsymbol{x}^*$ of the average dynamics affects the average value of the lift and drag force coefficients. However, since the force coefficients are not linearly dependent on the states, their average is not simply $C_L\left(\boldsymbol{x}^*\right)$ and $C_D\left(\boldsymbol{x}^*\right)$. Instead, each state is approximated with the first order expression $x_i(t) = x_i^* + A_{x_i}\cos\left(\omega t + \phi_i\right)$ and substituted into a multi-variable

Taylor series expansion of the lift and drag coefficients around $\boldsymbol{x}^*$

$$\begin{aligned} y_m &= \sum_{n_1=0}^{\infty} \cdots \sum_{n_d=0}^{\infty} \frac{\left(x_1 - x_1^*\right)^{n_1} \ldots \left(x_d - x_d^*\right)^{n_d}}{n_1! \ldots n_d!} \left(\frac{\partial^{n_1+\cdots+n_d} y_m}{\partial x_1^{n_1} \ldots \partial x_d^{n_d}} \right) (\boldsymbol{x}^*) \\ &= y_m(\boldsymbol{x}^*) + \sum_{i=1}^{n+5} \frac{\partial y_m(\boldsymbol{x}^*)}{\partial x_i} \left(x_i - x_i^*\right) + \frac{1}{2!} \sum_{i=1}^{n+5} \sum_{q=1}^{n+5} \frac{\partial^2 y_m(\boldsymbol{x}^*)}{\partial x_i \partial x_q} \left(x_i - x_i^*\right) \left(x_q - x_q^*\right) + \ldots \end{aligned} \tag{6.14}$$

where $y_m(\boldsymbol{x}), m \in (C_L, C_D)$.

Finally, the average of the force coefficients over one cycle of motion of the inputs is

$$\overline{y}_m = \frac{1}{T} \int_0^T y_m(t) dt \tag{6.15}$$

6.3.1 Average lift coefficient

The average lift coefficient of a pitching-plunging-surging wing over one cycle of motion is

$$\begin{aligned} \overline{C}_L &= C_{L,s}(\alpha^*) + \sigma(1 - k_{hf}) C_{L,s}(\alpha^*) \left(\cos\phi_U + \sigma \sin^2\phi_U\right) \\ &- Hk \left[\sin\phi + \sigma \left(\frac{1}{2} - k_{hf} \right) \sin(\phi - \phi_U) \right] C'_{L,s}(\alpha^*) \\ &+ \left[\frac{A_\alpha^2 k_{hf}}{4} + \frac{H^2 k^2}{4} \left(1 + 2\sin^2\phi\right) - \frac{A_\alpha H k k_{hf}}{2} \sin\phi \right] C''_{L,s}(\alpha^*) \\ &+ \frac{\sigma A_\alpha k_{\dot{\alpha}} k (1 - k_{hf})}{2b^2} \sin\phi_U + \frac{\pi \cos\alpha^*}{\tau_v U^*} \left(Hk \cos\alpha^* \sin\phi - \sigma b \cos\phi_U \sin\alpha^* \right) \\ &+ \mathcal{O}\left(\epsilon^3; m_v, A_\alpha, H, \sigma\right) \end{aligned} \tag{6.16}$$

with the infinite series being truncated at the order $\mathcal{O}(\epsilon^2)$. The variable $\overline{C}_L$ represents the mean unsteady lift coefficient, and $C_{L,s}(\alpha^*)$ is the steady lift coefficient at the mean angle of attack α^*. Therefore, any difference between these two variables indicates the generation of forces due to unsteady motion. The parameters $C'_{L,s} = \frac{\partial C_{L,s}}{\partial \alpha}$ and $C''_{L,s} = \frac{\partial^2 C_{L,s}}{\partial \alpha^2}$ are the

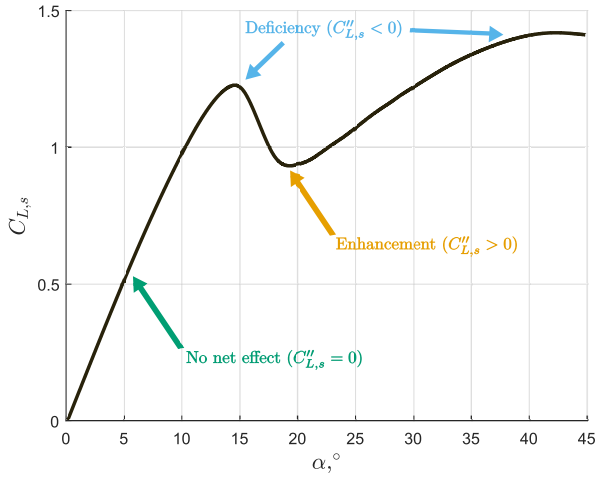

Figure 6.2: Steady lift curve for a NACA 0012 airfoil at $Re = 500,000$ [81].

first and second derivatives of the steady lift coefficient curve as a function of the angle of attack, respectively.

In the particular case in which the surging, pitching and plunging motions are in phase, the average lift coefficient over one cycle of motion is

$$\overline{C}_L = C_{L,s}\left(\alpha^*\right) + \sigma\left(1 - k_{hf}\right) C_{L,s}\left(\alpha^*\right) + \left(\frac{k_{hf} A_\alpha^2}{4} + \frac{H^2 k^2}{4}\right) C''_{L,s}\left(\alpha^*\right) + \mathcal{O}\left(\epsilon^3; m_v, A_\alpha, H, \sigma\right) \quad (6.17)$$

The analysis recovers the results in Eq. (4.14) of Section 4, in which the curvature of the steady lift curve governs the lift enhancement and deficiency due to the pitching and plunging motions. In that case and for a conventional airfoil, the theory predicted no unsteady effects in the linear region of the steady lift curve, at low angles of attack; a decrease in the lift force at stall, where the curvature is negative; lift enhancement in the post-stall regime, where the curvature of the steady lift curve is positive, as pictured in Fig. 6.2.

However, in the case of the surging motion, the force generation mechanisms are not proportional to the second derivative of the steady lift curve. The surging effects are proportional

to the value of the steady lift curve. Recalling that k_{hf} is the high-frequency gain, which is always lower than one, the term $(1 - k_{hf})$ is always positive. Therefore, for a conventional airfoil, the analysis predicts lift enhancement at all angles of attack, with the increase in force being proportional to σ, the amplitude of the surging motion normalized by the free stream velocity U^*.

Eq. (6.16) shows the combined effect of pitching, plunging, and surging oscillations when the motions are not in phase. The second line in Eq. (6.16) indicates the possibility of force generation when the plunging and surging motions are delayed with respect to the pitching oscillations. The possible force mechanism is proportional to the first derivative of the steady lift curve, predicting lift deficiency in the linear region but an increment in the force after stall and before the trough of the curve. A similar effect appears in the last line, with the first term predicting the occurrence of force generation mechanisms when the pitching and surging motions are not in phase. Finally, the last term uncovers the effect of the added mass, which only appears through the interaction between the different motions when they are not in phase.

6.3.2 Average drag coefficient

The average drag coefficient of a surging wing over one cycle of motion is

$$\begin{aligned}\overline{C}_D = C_{D,s}\left(\alpha^*\right) + \sigma\left(1 - k_{hf}\right)\left[C_{L,s}\left(\alpha^*\right)\tan\alpha^* - \frac{k_S\left(\alpha^*\right)}{2\pi^2}C_{L,s}^2\left(\alpha^*\right) - \frac{m_v}{U^* b\rho\tau_v}\sin^2\alpha^*\right] \\ + \sigma^2\left(1 - k_{hf}\right)\left[C_{L,s}\left(\alpha^*\right)\tan\alpha^* - \frac{k_S\left(\alpha^*\right)}{2\pi^2}\frac{3\left(7 - 3k_{hf}\right)}{4}C_{L,s}^2\left(\alpha^*\right)\right] \\ + \mathcal{O}\left(\epsilon^3; m_v, A_\alpha, H, \sigma\right) \quad (6.18)\end{aligned}$$

with the infinite series being truncated at the order $\mathcal{O}\left(\epsilon^2\right)$. The variable $\overline{C}_D$ represents the mean unsteady drag coefficient, and $C_{D,s}\left(\alpha^*\right)$ is the steady drag coefficient at the mean angle

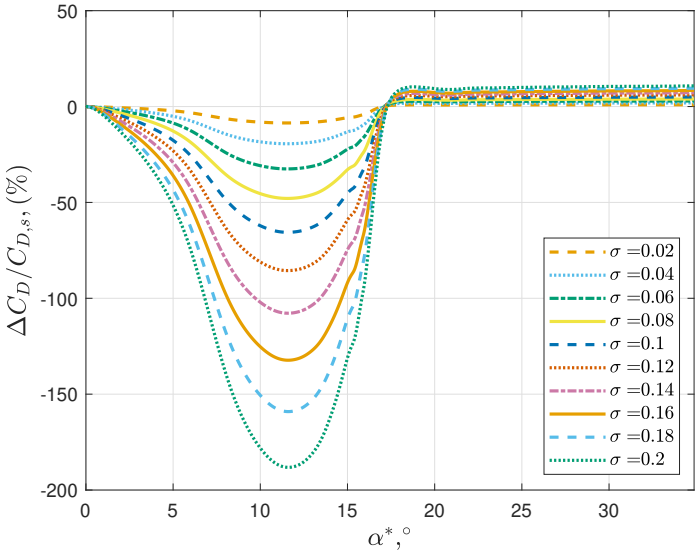

Figure 6.3: Percentage of increase in the drag force due to the surging motion for different amplitudes of oscillation for a NACA 0012 airfoil at $Re = 500,000$.

of attack α^*. Therefore, any difference between these two variables indicates the generation of forces due to unsteady motion. The variable k_s is the suction parameter, used in the definition of the suction force.

Eq. (6.18) reveals the role of the projection of the lift force in the direction of the free stream, the suction force, and the added mass effects in the reduction or increase of the unsteady drag force. The term $C_{L,s}(\alpha^*)\tan\alpha^*$ is responsible for the increase in drag due to nonlinear lift occurring in the post-stall regime, as pictured in Fig. 6.3. The figure plots Eq. (6.18) using the $C_{L,s}$, $C_{D,s}$, and k_S values obtained from steady simulations of a NACA 0012 airfoil at $Re = 500,000$. More interestingly, Fig. 6.3 shows a significant reduction in the drag force in the linear and stall regimes, indicating the production of thrust. In fact, the theory predicts the generation of a thrust force overcoming drag when oscillating between $\alpha^* = 7, 15°$ (where $\Delta C_D/C_{D,s} < -100\%$), leading to forward motion. The thrust production and drag increase mechanisms are proportional to the amplitude of motion, with the effect of σ being more pronounced in the thrust production regime.

The average drag coefficient of a pitching-plunging-surging airfoil over one cycle of motion is

$$
\begin{aligned}
\overline{C}_D &= C_{D,s}\left(\alpha^*\right) + \sigma\left(1-k_{hf}\right)\left(\sigma+\cos\phi_U\right)C_{L,s}\left(\alpha^*\right)\tan\alpha^* \\
&- \frac{k_S\left(\alpha^*\right)}{2\pi^2}C_{L,s}^2\left(\alpha^*\right)\left[\frac{1}{2}+\sigma\left(1-k_{hf}\right)\cos\phi_U\right] \\
&+ \frac{m_v}{U^* b\rho\tau_v}\left(Hk\cos\alpha^*\sin\phi-\sigma\sin\alpha^*\cos\phi_U\right)\sin\alpha^* \\
&- Hk\left\{C'_{L,s}\left(\alpha^*\right)\left[\tan\alpha^*-\frac{k_S\left(\alpha^*\right)}{2\pi^2}C_{L,s}\left(\alpha^*\right)\right]+\frac{C_{L,s}^2\left(\alpha^*\right)}{4\pi^2}k'_S\left(\alpha^*\right)\right\}\sin\phi \\
&- \frac{\sigma^2 k_S\left(\alpha^*\right)}{2\pi^2}\left(1-k_{hf}\right)\left[\frac{1+k_{hf}}{4}+2\left(2-k_{hf}\right)\left(\frac{1}{4}+\cos^2\phi_U\right)\right]C_{L,s}^2\left(\alpha^*\right) \\
&+ \frac{A_\alpha^2}{4}\left\{\frac{2}{\cos^2\alpha^*}\left(C_{L,s}\left(\alpha^*\right)\tan\alpha^*+k_{hf}C'_{L,s}\left(\alpha^*\right)\right)+k_{hf}C''_{L,s}\left(\alpha^*\right)\tan\alpha^*\right. \\
&- \frac{k_S\left(\alpha^*\right)}{2\pi^2}\left[k_{hf}C_{L,s}\left(\alpha^*\right)C''_{L,s}\left(\alpha^*\right)+k_{hf}^2\left(C'_{L,s}\left(\alpha^*\right)\right)^2+k^2\left(\pi-k_{\dot\alpha}k_{hf}\right)^2\right] \\
&\left.- \frac{C_{L,s}\left(\alpha^*\right)}{\pi^2}\left(k_{hf}k'_S\left(\alpha^*\right)C'_{L,s}\left(\alpha^*\right)+\frac{k''_S\left(\alpha^*\right)C_{L,s}\left(\alpha^*\right)}{4}\right)\right\} \\
&+ \frac{H^2k^2}{4}\left\{\left(3-2\cos^2\phi\right)C''_{L,s}\left(\alpha^*\right)\tan\alpha^*\right. \\
&- \frac{k_S\left(\alpha^*\right)}{2\pi^2}\left[\left(3-2\cos^2\phi\right)C_{L,s}\left(\alpha^*\right)C''_{L,s}\left(\alpha^*\right)+\left(2\left(1-\cos^2\phi\right)+k_{hf}^2\right)\left(C'_{L,s}\left(\alpha^*\right)\right)^2\right] \\
&- \frac{C_{L,s}\left(\alpha^*\right)}{\pi^2}\left[\left(2\left(1-\cos^2\phi\right)+k_{hf}\right)k'_S\left(\alpha^*\right)C'_{L,s}\left(\alpha^*\right)\right. \\
&\left.\left.+\frac{k''_S\left(\alpha^*\right)C_{L,s}\left(\alpha^*\right)}{4}\left(3-2\cos^2\phi\right)\right]\right\} \\
&- \frac{A_\alpha Hk}{2}\left\{k_{hf}\left(C''_{L,s}\left(\alpha^*\right)\tan\alpha^*+\frac{C'_{L,s}\left(\alpha^*\right)}{\cos^2\alpha^*}\right)\sin\phi\right. \\
&- \frac{k_{hf}k_S\left(\alpha^*\right)}{2\pi^2}\left[k\left(\pi-k_{\dot\alpha}k_{hf}\right)C'_{L,s}\left(\alpha^*\right)\cos\phi+k_{hf}\left(C'_{L,s}\left(\alpha^*\right)\right)^2\sin\phi\right. \\
&+ C_{L,s}\left(\alpha^*\right)C''_{L,s}\left(\alpha^*\right)\sin\phi\left.\right] - \frac{C_{L,s}\left(\alpha^*\right)}{\pi^2}\left[\frac{C_{L,s}\left(\alpha^*\right)k''_S\left(\alpha^*\right)}{4}\sin\phi\right. \\
&\left.\left.+k'_S\left(\alpha^*\right)\left(\frac{k}{2}\left(\pi-k_{\dot\alpha}k_{hf}\right)\cos\phi+k_{hf}C'_{L,s}\left(\alpha^*\right)\sin\phi\right)\right]\right\}
\end{aligned}
$$

$$
\begin{aligned}
&- \frac{A_\alpha \sigma}{2}\Bigg\{ \frac{1}{\cos^2\alpha^*}\left(1-k_{hf}\right)C_{L,s}\left(\alpha^*\right)\cos\phi_U - 2k_{\dot\alpha}k\left(\frac{1}{2}+k_{hf}\right)\tan\alpha^*\sin\phi_U \\
&- \frac{k_S\left(\alpha^*\right)C_{L,s}\left(\alpha^*\right)}{2\pi^2}\Bigg[k_{hf}\left(1-k_{hf}\right)C'_{L,s}\left(\alpha^*\right)\cos\phi_U + k\big[k_{\dot\alpha}\left(1-k_{hf}^2+3k_{hf}\right) \\
&- \pi\left(2+k_{hf}\right)\big]\sin\phi_U\Bigg] - \frac{C_{L,s}^2\left(\alpha^*\right)}{2\pi^2}\left(1-k_{hf}\right)k'_S\left(\alpha^*\right)\cos\phi_U\Bigg\} \\
&+ \frac{Hk\sigma}{2}\Bigg\{ \left(2k_{hf}-1\right)C'_{L,s}\left(\alpha^*\right)\tan\alpha^*\sin\left(\phi-\phi_U\right) \\
&- \frac{k_S\left(\alpha^*\right)}{2\pi^2}C_{L,s}\left(\alpha^*\right)C'_{L,s}\left(\alpha^*\right)\left[\left(5\left(k_{hf}-1\right)-k_{hf}^2\right)\sin\left(\phi-\phi_U\right) - 2\left(2-k_{hf}\right)\sin\left(\phi+\phi_U\right)\right] \\
&+ \frac{C_{L,s}^2\left(\alpha^*\right)}{2\pi^2}k'_S\left(\alpha^*\right)\left[\left(\frac{1}{2}-k_{hf}\right)\sin\left(\phi-\phi_U\right) + 2\left(1-k_{hf}\right)\sin\left(\phi+\phi_U\right)\right]\Bigg\} \\
&\qquad + \mathcal{O}\left(\epsilon^3; m_v, A_\alpha, H, \sigma\right) \quad (6.19)
\end{aligned}
$$

where $k'_S = \frac{\partial k_S}{\partial \alpha}$ and $k''_S = \frac{\partial^2 k_S}{\partial \alpha^2}$ are the first and second derivatives of the suction parameter as a function of the angle of attack, respectively.

In the particular case in which the pitching, plunging, and surging motions are in phase

$$
\begin{aligned}
&\overline{C}_D = C_{D,s}\left(\alpha^*\right) + \sigma^2\left(1+\sigma\right)\left(1-k_{hf}\right)C_{L,s}\left(\alpha^*\right)\tan\alpha^* \\
&- \frac{k_S\left(\alpha^*\right)}{2\pi^2}C_{L,s}^2\left(\alpha^*\right)\left[\frac{1}{2}+\sigma\left(1-k_{hf}\right)\right] - \frac{\sigma m_v}{U^* b\rho\tau_v}\sin^2\alpha^* \\
&- \frac{\sigma^2 k_S\left(\alpha^*\right)}{2\pi^2}\left(1-k_{hf}\right)\frac{3\left(7-3k_{hf}\right)}{4}C_{L,s}^2\left(\alpha^*\right) \\
&+ \frac{A_\alpha^2}{4}\Bigg\{ \frac{2}{\cos^2\alpha^*}\left(C_{L,s}\left(\alpha^*\right)\tan\alpha^* + k_{hf}C'_{L,s}\left(\alpha^*\right)\right) + k_{hf}C''_{L,s}\left(\alpha^*\right)\tan\alpha^* \\
&- \frac{k_S\left(\alpha^*\right)}{2\pi^2}\left[k_{hf}C_{L,s}\left(\alpha^*\right)C''_{L,s}\left(\alpha^*\right) + k_{hf}^2\left(C'_{L,s}\left(\alpha^*\right)\right)^2 + k^2\left(\pi - k_{\dot\alpha}k_{hf}\right)^2\right] \\
&- \frac{C_{L,s}\left(\alpha^*\right)}{\pi^2}\left(k_{hf}k'_S\left(\alpha^*\right)C'_{L,s}\left(\alpha^*\right) + \frac{k''_S\left(\alpha^*\right)C_{L,s}\left(\alpha^*\right)}{4}\right)\Bigg\} \\
&+ \frac{H^2k^2}{4}\Bigg\{ C''_{L,s}\left(\alpha^*\right)\tan\alpha^* - \frac{k_S\left(\alpha^*\right)}{2\pi^2}\left[C_{L,s}\left(\alpha^*\right)C''_{L,s}\left(\alpha^*\right) + k_{hf}^2\left(C'_{L,s}\left(\alpha^*\right)\right)^2\right] \\
&- \frac{C_{L,s}\left(\alpha^*\right)}{\pi^2}\left[k_{hf}k'_S\left(\alpha^*\right)C'_{L,s}\left(\alpha^*\right) + \frac{k''_S\left(\alpha^*\right)C_{L,s}\left(\alpha^*\right)}{4}\right]\Bigg\}
\end{aligned}
$$

$$+\frac{A_\alpha Hk}{4\pi^2}\left[kk_{hf}^2\left(\pi-k_{\dot{\alpha}}\right)k_S\left(\alpha^*\right)C'_{L,s}\left(\alpha^*\right)+k\left(\pi-k_{\dot{\alpha}}k_{hf}\right)k'_S\left(\alpha^*\right)C_{L,s}\left(\alpha^*\right)\right]$$
$$-\frac{A_\alpha\sigma}{2}\left(1-k_{hf}\right)\left\{\frac{C_{L,s}\left(\alpha^*\right)}{\cos^2\alpha^*}-\frac{C_{L,s}\left(\alpha^*\right)}{2\pi^2}\left[k_{hf}k_S\left(\alpha^*\right)C'_{L,s}\left(\alpha^*\right)-C_{L,s}\left(\alpha^*\right)k'_S\left(\alpha^*\right)\right]\right\}$$
$$+\mathcal{O}\left(\epsilon^3;m_v,A_\alpha,H,\sigma\right) \quad (6.20)$$

Eq. (6.19) and Eq. (6.20) show the combined effect of the pitching, plunging, and surging motions on the average aerodynamic forces on the wing.

Chapter 7

Conclusions and future work

7.1 Summary of work completed

This work explores the application of geometric control theory to the study of unsteady fluid flows. The objective of this research is the development of an analysis tool allowing a systematic discovery of force generation mechanisms in unsteady flows and capable of distilling the physics behind them. The study focuses on the prediction of the average aerodynamic forces in a harmonically pitching-plunging wing.

After the introduction of the fundamental theories of unsteady aerodynamics, the work follows with the derivation of a new reduced-order model (ROM) for a wing in harmonic pitching-plunging motion. The modeling of the lift dynamics respects Theodorsen's initial division of the unsteady lift contributions: circulatory lift and non-circulatory lift. The representation of the circulatory contribution relies on the quasi-steady circulation (the equivalent circulation for a static airfoil) as the input of the state-space model, instead of the angle of attack, as it usually is. The dynamics of the non-circulatory lift include the effect of the viscosity, which induces lag to the non-circulatory force. This viscous addition changes the

nature of the non-circulatory lift from an algebraic expression to a state-space model with dynamics, similar to the circulatory lift. The drag dynamics are modeled with the projection of the normal force and with the suction force proposed by Garrick. The latter is a pressure force whose total contribution amounts to a net force in the left direction. Hence, the inclusion of this force, which only occurs in unsteady motion, shows the possibility of drag reduction or even thrust generation in certain unsteady regimes. Finally, the model includes the dynamics of the location of the separation point, derived from a combination of Kirchoff's theory for steady flows and Goman-Khrabrov's model for pitching airfoils. The combination of all these dynamics yields a reduced-order model capable of capturing the main physical aspects of unsteady flows in a compact format. The conciseness of the model permits an analytical study of the dynamics in a geometric control framework.

The application of averaging in combination with geometric control theory to the developed ROM for small-amplitude, high-frequency oscillations reveals symmetry breaking in the lift and drag dynamics. The results point to possible enhancement or reduction of the lift force in certain flight regimes, with this generation of forces being governed by the curvature of the steady lift coefficient curve as a function of the angle of attack. When oscillating in regions of positive curvature (near the trough in the post-stall regime), lift enhancement occurs. In contrast, oscillations in regions of negative curvature (around the peak of the stall regime) lead to a decrease in the average lift coefficient with respect to its steady counterpart. A literature review of experimental and computational studies of pitching-plunging airfoils shows good agreement with the results. Further validation is performed with URANS simulations of a NACA0012 airfoil, confirming the theoretical findings. The results confirm the potential of geometric control theory as a tool for the discovery of unintuitive symmetry breaking phenomena in unsteady flows. The aforementioned analysis is of qualitative nature and does not provide accurate quantitative results. Instead, the study points to regimes inducing nonlinear force generation flow mechanisms.

The analysis of the drag force for small-amplitude high-frequency oscillations captures the suction force effect described by Garrick, which occurs to airfoils plunging in the linear region of the steady lift coefficient curve. The results also predict a drop in the suction force after the lift stall, leading to a big increase in the average drag force coefficient with respect to the steady drag. However, the post-stall regime presents another decrease in the drag force, pointing to a thrust generation mechanism. The outcomes are also validated with URANS simulations, showing similar results.

Given the promising results achieved in the analysis of the developed ROM using a geometric control framework, the same study is applied to the well-established Beddoes-Leishman model for dynamic stall. This ROM focuses on the effect of the leading-edge vortex (LEV) that appears when the airfoil is undergoing dynamic stall. The analysis of the Beddoes-Leishman model reveals symmetry breaking in both lift and drag forces. Moreover, the rate of change in the strength of the leading-edge vortex is the main parameter governing these force generation mechanisms. The positive contribution of the vortex when oscillating around stall leads to lift enhancement, or an increase in the average lift force when compared to its steady value. When the oscillation occurs in the post-stall region, the negative rate of change in the vortex strength reduces the average lift on the airfoil. Both pitching and plunging motions depict the aforementioned results, with the enhancement/reduction being controlled by the reduced frequency and the amplitude of motion. However, compressibility also plays a major role for pitching airfoils in this lift enhancement process. That is, pitching oscillations need to occur at high Mach numbers to induce substantial lift enhancement.

Although leading-edge vortex effects are observed in the unsteady drag coefficient of pitching airfoils, their contribution is negligible with respect to the added mass effects. This Mach-dependent contribution, which is dominant over the other effects, suggests an increase in the drag force due to the pitching motion at all mean angles of attack. However, the effect is mitigated at higher angles of attack and high Mach numbers.

On the other hand, the leading-edge vortex dictates the increment and reduction in the drag force of plunging airfoils. The positive rate of change in the vortex strength at stall increases the average drag force of a plunging airfoil when compared to a steady wing. Nonetheless, in the post-stall regime, the leading-edge vortex yields a significant reduction in drag. In fact, the present analysis suggests the generation of a thrust force that overcomes the aerodynamic drag, propelling the airfoil forward. However, this thrust mechanism only occurs when the airfoil is plunging above the stall angle.

Finally, this research studied the dynamics of the lift force on a wing performing harmonic surging oscillations. Using the previously developed ROM, the averaging analysis determined a force generation mechanism due to the surging motion that is proportional to the value of the steady lift. This mechanism, of different nature than the ones observed in the pitching and plunging motions, suggests an enhancement of the lift force at all angles of attack. At the same time, the surging motion also changes the dynamics of the drag force. The analysis reveals an increase and reduction of the drag coefficient in different flight regimes. More interestingly, surging oscillations close to stall may produce thrust capable of overcoming the drag force, leading to forward motion of the wing.

7.2 Recommendations for future work

The work completed shows the potential of geometric control theory as a tool for the analysis of force generation phenomena in fluid mechanics. The ROM developed for this analysis, formulated in Section 2.3.2 captures the main physical aspects of the flow in a compact form. As such, it can expanded to include more inputs to the current pitching-plunging wing. Of particular interest would be those inputs related to flight control dynamics. In other words, one could perform the same geometric control analysis for the control surfaces of the wing. In this case, the focus would not be on a wing but on the whole airplane. The objective would

be to study the effect of oscillations of the control surfaces on the overall flight dynamics of the aircraft. The resulting ROM would include the effect of the ailerons, the elevator, and other flow control systems. A proposed formulation would be

$$\dot{\boldsymbol{x}}(t) = \boldsymbol{f}(\boldsymbol{x}(t)) + \boldsymbol{g}_{\delta_a}(\boldsymbol{x}(t))\delta_a(t) + \boldsymbol{g}_{\delta_e}(\boldsymbol{x}(t))\delta_e(t) + \boldsymbol{g}_{\delta_{AFC_1}}(\boldsymbol{x}(t))\delta_{AFC_1}(t) + +\boldsymbol{g}_{\delta_{AFC_2}}(\boldsymbol{x}(t))\delta_{AFC_2}(t) + \dots \quad (7.1)$$

where g_{δ_a} and g_{δ_e} are the aileron and elevator control vector fields, which correspond to the aileron deflection δ_a and elevator deflection δ_e inputs. The second line of the equation describes other longitudinal control inputs that may be associated to the aircraft, such as synthetic jets, suction/blowing mechanisms, or plasma actuators.

Another field that could benefit from geometric control theory is the study of the flight mechanics of a rigid body, i.e. an insect, a bird, or an aircraft. In the recent years, there has been a major development of flapping-wing microair vehicles (FWMAVs), and an increase in the study of bio-flight. These multi-scale, nonlinear, time-varying systems rely on higher-order interactions between the periodic aerodynamic forces and the body motion to generate some stabilizing mechanisms [78, 85]. However, the majority of the studies on the flight dynamics of FWMAVs average the dynamics of the aerodynamic forces over the flapping cycle. This assumption has been shown to be deficient [78, 85]. In fact, there is a strong interaction between the rapid-scale dynamics of the aerodynamic forces and the slow-scale dynamics of the body, which is not captured when the forces are averaged over the flapping cycle. The method described in this work, which applies a combination of averaging and geometric control theory could analyze these higher-order effects. The application of geometric control theory to the study of vibrational stabilization due to the flight dynamics of a rigid body has been performed in the longitudinal direction [78, 80, 86]. However, lateral vibrational stabilization mechanisms, with considerably richer dynamics, lack any similar study in a geometric control framework. As such, the community could benefit of some work

in this regard.

Bibliography

[1] A. A. Agračev and R. V. Gamkrelidze. The exponential representation of flows and the chronological calculus. *Matematicheskii Sbornik*, 149(4):467–532, 1978.

[2] J. D. Anderson Jr. *Introduction to Flight*. McGraw-Hill, 3 edition, 1989.

[3] P. Ansell. The onset of dynamic stall: Understanding flowfield unsteadiness to enable closed-loop control. Technical report, University of Illinois, 2019.

[4] T. S. Beddoes. Practical computation of unsteady lift. In *Eight European Rotorcraft Forum*, number 2, Aix-en-Provence, France, 1982.

[5] R. Brockett. The early days of geometric nonlinear control. *Automatica*, 50(9):2203–2224, 2014.

[6] R. W. Brockett. System theory on group manifolds and coset spaces. *SIAM Journal on Control and Optimization*, 10(2):265–284, 1972.

[7] R. W. Brockett. Nonlinear systems and differential geometry. *Proceedings of the IEEE*, 64(1):61–72, 1976.

[8] R. W. Brockett. Control theory and singular Riemannian geometry. In P. J. Hilton and G. S. Young, editors, *New directions in applied mathematics*, pages 11–27. Springer New York, New York, NY, 1982.

[9] R. W. Brockett. Asymptotic stability and feedback stabilization. In *Differential geometric control theory*, pages 181–191. Birkhauser, 1983.

[10] F. Bullo. Averaging and vibrational control of mechanical systems. *SIAM Journal on Control and Optimization*, 41(2):542–562, 2003.

[11] F. Bullo and A. D. Lewis. *Geometric control of mechanical systems: modeling, analysis and design for symple mechanical control systems*, volume 49. Springer, New York, 2004.

[12] L. W. Carr. Progress in analysis and prediction of dynamic stall. *Journal of Aircraft*, 25(1):6–17, 1988.

[13] H. K. Cheng. Remarks on nonlinear lift and vortex separation. *Journal of the Aeronautical Sciences*, 3(21):212–214, 1954.

[14] N. Chiereghin, D. J. Cleaver, and I. Gursul. Unsteady lift and moment of a periodically plunging airfoil. *AIAA Journal*, 57(1):208–222, 2019.

[15] D. J. Cleaver, Z. Wang, and I. Gursul. Bifurcating flows of plunging aerofoils at high Strouhal numbers. *Journal of Fluid Mechanics*, 708:349–376, 2012.

[16] D. J. Cleaver, Z. Wang, and I. Gursul. Investigation of high-lift mechanisms for a flat-plate airfoil undergoing small-amplitude plunging oscillations. *AIAA Journal*, 51(4):968–980, 2013.

[17] D. J. Cleaver, Z. Wang, I. Gursul, and M. R. Visbal. Lift enhancement by means of small-amplitude airfoil oscillations at low Reynolds numbers. *AIAA Journal*, 49(9):2018–2033, 2011.

[18] P. E. Crouch. Spacecraft attitude control and stabilization: Applications of geometric control theory to rigid body models. *IEEE Transactions on Automatic Control*, 29(4):321–331, 1984.

[19] S. Deng, M. Percin, B. van Oudheusden, B. Remes, and H. Bijl. Experimental investigation on the aerodynamics of a bio-inspired flexible flapping wing micro air vehicle. *International Journal of Micro Air Vehicles*, 6(2):105–115, 2014.

[20] I. E. Garrick. Propulsion of a flapping and oscillating airfoil. Technical Report NACA-TR-567, National Advisory Committee for Aeronautics, Hampton, 1936.

[21] I. E. Garrick. On some reciprocal relations in the theory of nonstationary flows. Technical Report NACA-TR-629, National Advisory Committee for Aeronautics, Langley Field, VA, 1938.

[22] M. Goman and A. Khrabrov. State-space representation of aerodynamic characteristics of an aircraft at high angles of attack. *Journal of Aircraft*, 31(5):1109–1115, 1994.

[23] L. Gray and J. Liiva. Two-dimensional tests of airfoils oscillating near stall. Volume II: Data report. Technical report, The Boeing Company, Fort Eustis, Virginia, 1968.

[24] I. Gursul and D. Cleaver. Plunging oscillations of airfoils and wings: Progress, opportunities, and challenges. *AIAA Journal*, 57(9):3648–3665, 2019.

[25] J. Han, Z. Hui, F. Tian, and G. Chen. Review on bio-inspired flight systems and bionic aerodynamics. *Chinese Journal of Aeronautics*, 34(7):170–186, 2021.

[26] A. M. Hassan and H. E. Taha. Geometric control formulation and nonlinear controllability of airplane flight dynamics. *Nonlinear Dynamics*, 88(4):2651–2669, 2017.

[27] A. M. Hassan and H. E. Taha. Differential-geometric-control formulation of flapping flight multi-body dynamics. *Journal of Nonlinear Science*, 29(4):1379–1417, 2019.

[28] A. M. Hassan and H. E. Taha. Design of a nonlinear roll mechanism for airplanes using Lie Brackets for high alpha operation. *IEEE Transactions on Aerospace and Electronic Systems*, 57(1):462–475, 2020.

[29] R. T. Jones. Operational treatment of the nonuniform-lift theory in airplane dynamics. Technical Report NACA-TR-667, National Advisory Committee for Aeronautics, Washington, D.C., 1938.

[30] W. P. Jones. Aerodynamic forces on wings in non-uniform motion. Technical Report 2117, British Aeronautical Research Council, 1945.

[31] M. Keennon, K. Klingebiel, H. Won, and A. Andriukov. Development of the Nano Hummingbird: A tailless flapping wing micro air vehicle. In *50th AIAA Aerospace Sciences Meeting including the New Horizons Forum and Aerospace Exposition*, number January, pages 1–24, Nashville, 2012.

[32] N. M. Khalifa, A. Rezaei, and H. E. Taha. On computational simulations of dynamic stall and its three-dimensional nature. *Physics of Fluids*, 35(10), 2023.

[33] M. Kiani, B. Davis, F. P. Quevedo, N. Cabezut, S. Hince, M. Balta, and H. Taha. A new bio-inspired flying concept: The quadflapper. *AIAA Scitech 2019 Forum*, (January):1–12, 2019.

[34] H. G. Küssner. Zusammenfassender Bericht über den instationären Auftrieb von Flügeln. *Luftfahrtforschung*, 13(12):410–424, 1936.

[35] T. Lee and P. Gerontakos. Investigation of flow over an oscillating airfoil. *Journal of Fluid Mechanics*, 512:313–341, 2004.

[36] J. G. Leishman. *Contributions to the mathematical modelling of unsteady aerodynamics and aeroacoustics using indicial theory*. PhD thesis, University of Glassgow, 2002.

[37] J. G. Leishman. *Principles of helicopter aerodynamics*. Cambridge University Press, 2nd ed. edition, 2006.

[38] J. G. Leishman and T. S. Beddoes. A semi-empirical model for dynamic stall. *Journal of the American Helicopter Society*, 34(3):3–17, 1989.

[39] J. G. Leishman and G. L. Crouse. State-space model for unsteady airfoil behavior and dynamic stall. In *30th Structures, Structural Dynamics and Materials Conference*, page 1319, 1989.

[40] J. G. Leishman and K. Q. Nguyen. State-space representation of unsteady airfoil behavior. *AIAA Journal*, 28(5):836–844, 1990.

[41] J. Lighthill. Aerodynamic aspects of animal flight. In T. Y.-T. Wu, C. J. Brokaw, and C. Brennen, editors, *Swimming and Flying in Nature*, pages 423–491. Springer, Boston, MA, 1 edition, 1975.

[42] W. Liu. An approximation algorithm for nonholonomic systems. *SIAM Journal on Control and Optimization*, 35(4):1328–1365, 1997.

[43] W. Liu. Averaging theorems for highly oscillatory differential equations and iterated Lie brackets. *SIAM Journal on Control and Optimization*, 35(6):1989–2020, 1997.

[44] L. Loumes. *Multilayer impedance pump: A bio-inspired valveless pump with medical applications*. PhD thesis, California Institute of Technology, 2007.

[45] K. Y. Ma, P. Chirarattananon, S. B. Fuller, and R. J. Wood. Controlled flight of a biologically inspired, insect-scale robot. *Science*, 340(6132):603–607, 2013.

[46] M. Maggia, S. A. Eisa, and H. E. Taha. On higher-order averaging of time-periodic systems: reconciliation of two averaging techniques. *Nonlinear Dynamics*, 99(1):813–836, 2020.

[47] K. W. McAlister, S. L. Pucci, W. J. McCroskey, and L. W. Carr. An experimental study of dynamic stall on advanced airfoil sections - Volume 2. Pressure and force data. Technical report, NASA, Moffett Field, California, 1982.

[48] W. J. McCroskey. Some current research in unsteady fluid dynamics. *Journal of Fluids Engineering*, 99(1):8–39, 1977.

[49] W. J. McCroskey. The Phenomenon of Dynamic Stall. Technical report, National Aeronautics and Space Administration, Moffett Field, California, 1981.

[50] I. Mir, H. Taha, S. A. Eisa, and A. Maqsood. A controllability perspective of dynamic soaring. *Nonlinear Dynamics*, 94(4):2347–2362, 2018.

[51] R. M. Murray, Z. Li, and S. S. Sastry. *A mathematical introduction to robotic manipulation*, volume 29. CRC Press, 1994.

[52] R. M. Murray and S. S. Sastry. Nonholonomic motion planning. Steering using sinusoids. *IEEE Transactions on Automatic Control*, 38(5):700–716, 1993.

[53] S. Narsipur, P. Hosangadi, A. Gopalarathnam, and J. R. Edwards. Variation of leading-edge suction during stall for unsteady aerofoil motions. *Journal of Fluid Mechanics*, 2020.

[54] A. H. Nayfeh. *Perturbation methods*. John Wiley & Sons, 1973.

[55] A. H. Nayfeh. *Introduction to perturbation techniques*. John Wiley & Sons, 1981.

[56] A. H. Nayfeh and B. Balachandran. *Applied nonlinear dynamics: analyical, computational, and experimental methods*. John Wiley & Sons, 1995.

[57] A. H. Nayfeh and D. T. Mook. *Nonlinear oscillations*. John Wiley & Sons, 1979.

[58] J. L. Palmer, M. B. Jones, and J. Drobik. Design elements of a bio-inspired micro air vehicle. In *IFAC Intelligent Autonomous Vehicles Symposium*, volume 8, pages 235–241, Gold Coast, Australia, 2013. IFAC.

[59] D. A. Peters. Two-dimensional incompressible unsteady airfoil theory-An overview. *Journal of Fluids and Structures*, 24(3):295–312, 2008.

[60] L. Pla Olea. *Geometric control theoretic formulation applied to the analysis of pitching and plunging airfoils*. Master's thesis, University of California, Irvine, 2019.

[61] L. Pla Olea, N. M. Khalifa, and H. E. Taha. Geometric Control Study of the Beddoes-Leishman Model in a Pitching-Plunging Airfoil. *AIAA SciTech Forum 2022*, pages 1–14, 2022.

[62] L. Pla Olea and H. E. Taha. Geometric control analysis of the unsteady aerodynamics of a pitching-plunging airfoil in dynamic stall [Manuscript submitted for publication]. 2023.

[63] T. N. Pornsin-Sirirak, Y.-C. Tai, C.-M. Ho, and M. Keennon. Microbat: A palm-sized electrically powered ornithopter. *Proceedings of NASA/JPL Workshop on Biomorphic Robotics*, 14:14 – 17, 2001.

[64] K. Ramesh, A. Gopalarathnam, K. Granlund, M. V. Ol, and J. R. Edwards. Discrete-vortex method with novel shedding criterion for unsteady aerofoil flows with intermittent leading-edge vortex shedding. *Journal of Fluid Mechanics*, 751:500–538, 2014.

[65] D. Rival and C. Tropea. Characteristics of pitching and plunging airfoils under dynamic-stall conditions. *Journal of Aircraft*, 47(1):80–86, 2010.

[66] D. E. Rival, J. Kriegseis, P. Schaub, A. Widmann, and C. Tropea. Characteristic length scales for vortex detachment on plunging profiles with varying leading-edge geometry. *Experiments in Fluids*, 55(1):1–8, 2014.

[67] K. V. Rozhdestvensky and V. A. Ryzhov. Aerohydrodynamics of flapping-wing propulsors. *Progress in Aerospace Sciences*, 39(8):585–633, 2003.

[68] A. Saini, S. Narsipur, and A. Gopalarathnam. Leading-edge flow sensing for detection of vortex shedding from airfoils in unsteady flows. *Physics of Fluids*, 33(8), 2021.

[69] J. A. Sanders and F. Verhulst. *Averaging methods in nonlinear dynamical systems*. Springer, New York, 1985.

[70] S. S. Sastry. *Nonlinear systems: Analysis, stability, and control*, volume 10 of *Interdisciplinary Applied Mathematics*. Springer-Verlag New York, New York, NY, 1999.

[71] H. Schlichting and E. Truckenbrodt. *Aerodynamics of the Airplane*. McGraw-Hill, 1979.

[72] L. Schwarz. Berechnung der druckverteilung siner harmonisch sich verformungen tragfläche in ebener stromung. *Luftfahrtforschungr*, 17:379–386, 1940.

[73] H. J. Sussmann. Orbits of families of vector fields and integrability of distributions. *Transactions of the American Mathematical Society*, 180:171–188, 1973.

[74] H. J. Sussmann. A general theorem on local controllability. *SIAM Journal on Control and Optimization*, 25(1):158–194, 1987.

[75] H. J. Sussmann and V. Jurdjevic. Controllability of nonlinear systems. *Journal of Differential Equations*, 12(1):95–116, 1972.

[76] H. E. Taha. Geometric nonlinear control of the lift dynamics of a pitching-plunging wing. In *AIAA Scitech 2020 Forum*, number January, pages 1–13, 2020.

[77] H. E. Taha, M. R. Hajj, and P. S. Beran. State-space representation of the unsteady aerodynamics of flapping flight. *Aerospace Science and Technology*, 34(1):1–11, 2014.

[78] H. E. Taha, M. R. Hajj, and A. H. Nayfeh. Longitudinal flight dynamics of hovering MAVs/Insects. *Journal of Guidance, Control, and Dynamics*, 37(3):970–978, 2014.

[79] H. E. Taha, A. Hassan, and M. Fouda. Nonlinear flight physics of the Lie Bracket roll mechanism. *Nonlinear Dynamics*, 106(3):1627–1646, 2021.

[80] H. E. Taha, M. Kiani, T. L. Hedrick, and J. S. Greeter. Vibrational control: A hidden stabilization mechanism in insect flight. *Science Robotics*, 5(46):1–12, 2020.

[81] H. E. Taha, L. Pla Olea, N. Khalifa, C. Gonzalez, and A. S. Rezaei. Geometric-control formulation and averaging analysis of the unsteady aerodynamics of a wing with oscillatory controls. *Journal of Fluid Mechanics*, 928(A30), 2021.

[82] H. E. Taha and A. S. Rezaei. On the dynamics of unsteady lift and circulation and the circulatory-non-circulatory classification. In *AIAA Scitech 2019 Forum*, pages 1–13. American Institute of Aeronautics and Astronautics, Inc., 2019.

[83] H. E. Taha and A. S. Rezaei. Viscous extension of potential-flow unsteady aerodynamics: The lift frequency response problem. *Journal of Fluid Mechanics*, 868:141–175, 2019.

[84] H. E. Taha and A. S. Rezaei. On the high-frequency response of unsteady lift and circulation: A dynamical systems perspective. *Journal of Fluids and Structures*, 93:102868, 2020.

[85] H. E. Taha, S. Tahmasian, C. A. Woolsey, A. H. Nayfeh, and M. R. Hajj. The need for higher-order averaging in the stability analysis of hovering, flapping-wing flight. *Bioinspiration and Biomimetics*, 10(1), 2015.

[86] H. E. Taha, C. A. Woolsey, and M. R. Hajj. Geometric control approach to longitudinal stability of flapping flight. *Journal of Guidance, Control, and Dynamics*, 39(2):214–226, 2016.

[87] S. Tahmasian and C. A. Woolsey. Flight control of biomimetic air vehicles using vibrational control and averaging. *Journal of Nonlinear Science*, 27(4):1193–1214, 2017.

[88] T. Theodorsen. General theory of aerodynamic instability and the mechanism of flutter. Technical Report NACA-TR-496, National Advisory Committe for Aeronautics, Hampton, 1935.

[89] N. Vandenberghe, J. Zhang, and S. Childress. Symmetry breaking leads to forward flapping flight. *Journal of Fluid Mechanics*, 506(506):147–155, 2004.

[90] P. A. Vela, K. A. Morgansen, and J. W. Burdick. Underwater locomotion from oscillatory shape deformations. In *Proceedings of the IEEE Conference on Decision and Control*, volume 2, pages 2074–2080, Las Vegas, Nevada USA, 2002.

[91] M. R. Visbal. Control of dynamic stall on a pitching airfoil using high-frequency actuation. *53rd AIAA Aerospace Sciences Meeting*, (January), 2015.

[92] M. R. Visbal and D. J. Garmann. Dynamic stall of a finite-aspect-ratio wing. *AIAA Journal*, 57(3):962–977, 2019.

[93] T. von Kármán and W. R. Sears. Airfoil theory for non-uniform motion. *Journal of the Aeronautical Sciences*, 5(10):379–390, 1938.

[94] H. Wagner. Über die Entstehung des dynamischen Auftriebes von Tragflügeln. *Mathematica*, 5:17–35, 1925.

[95] G. C. Walsh and S. Sastry. On reorienting linked rigid bodies using internal motions. In *Proceedings on the 30th Conference on Decision and Control*, pages 1190–1195, Brighton, England, 1991.

[96] G. C. Walsh and S. S. Sastry. On reorienting linked rigid bodies using internal motions. *IEEE Transactions on Robotics and Automation*, 11(1):139–146, 1995.

Appendix A

Study on the average rate of change in the strength of the leading-edge vortex $\dot{C}_v^*$

The results in Chapter 5 demonstrate the importance of the rate of change in the strength of the leading-edge vortex (LEV) $\dot{C}_v^*$ in the calculation of the average lift and drag forces on an airfoil. These parameter, of ultimate importance in the representation of dynamic stall in the Beddoes-Leishman model, acts as the governing variable in the determination of lift or drag enhancement or deficiency in most of the studied cases. Therefore, a proper understanding of the behavior of $\dot{C}_v^*$ is needed to evaluate its effect on the force coefficients.

Nonetheless, the rate of change in the strength of the LEV has a complex nonlinear dependence on the parameters of motion of the wing: the amplitude of the pitching oscillations A_α, the amplitude of the plunging oscillations H, and the reduced frequency k. The prediction of the relations between these variables is not trivial and requires a numerical approach. In this section, the Beddoes-Leishman model is simulated at different values of A_α, H, and k

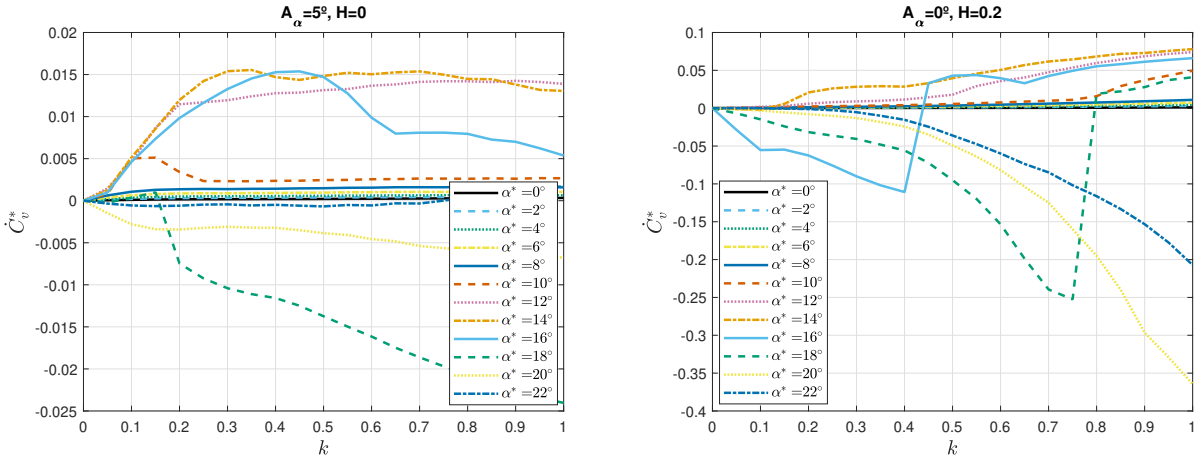

(a) Airfoil pitching at $A_\alpha = 5°$.

(b) Airfoil plunging at $H = 0.2$.

Figure A.1: Effect of the reduced frequency k on the time-derivative of the vortex strength $\dot{C}_v^*$ for different mean angles of attack α^* in an oscillating NACA 0012 airfoil at $Re = 500,000$ and $M = 0.3$.

to obtain the value of $\dot{C}_v^*$ at different flight conditions. The results are presented below for a NACA 0012 airfoil at $Re = 5 \cdot 10^5$, with a summary of the conclusions at the end of the section.

However, before studying the effect of the parameters of motion on $\dot{C}_v^*$, it may be of interest to clarify the forces on the airfoil under steady conditions. Fig. 5.1 displays the steady lift and drag coefficients C_L and C_D, respectively, as a function of the angle of attack for a NACA 0012 airfoil at $Re = 5 \cdot 10^5$. The steady lift coefficient shows a linear increase at low angles of attack until reaching the stall angle at $\alpha \simeq 15°$, indicated by a decrease in lift. At higher angles of attack, the loss in lift reaches a minimum at $\alpha \simeq 20°$, and the lift coefficient increases again, although at a lower rate. The drag coefficient grows slowly with α at low angles of attack, with a sharp increment when the airfoil experiments stall. At higher angles of attack, the steady drag coefficient keeps increasing with *alpha* at a higher rate.

A.1 Effect of the reduced frequency

Fig. A.1a shows the effect of the reduced frequency on $\dot{C}_v^*$ for an airfoil pitching at different mean angles of attack with an amplitude of $A_\alpha = 5°$. At low α^*, the rate of change of the strength of the leading-edge vortex is positive and presents an asymptotic behavior past a reduced frequency of approximately $k = 0.2$, with the asymptotic value increasing with the mean angle of attack. However, as the mean angle of attack approaches the stall angle, the evolution of the strength of the leading-edge vortex with the reduced frequency becomes more complex. When α^* enters the nonlinear region of the steady lift curve at $\alpha^* = 10°$, $\dot{C}_v^*$ rapidly increases with the reduced frequency, reaching a maximum at $k = 0.12$, and then decreasing. After this parabolic behavior, at a reduced frequency of $k = 0.25$, the rate of change of the leading-edge vortex shows the same asymptotic behavior obtained when pitching the airfoil at mean angles of attack in the nonlinear region. As α^* approaches the stall angle ($12° \leq \alpha^* \leq 16°$), the rise and reduction in $\dot{C}_v^*$ is accentuated, with the maximum value occurring at higher reduced frequencies as the mean angle of attack increases. At these angles of attack, however, an asymptotic behavior does not follow the decrease in $\dot{C}_v^*$. When pitching at the trough of the steady lift curve ($\alpha^* = 18°$), the rate of change in the strength of the leading-edge vortex becomes negative and diverges as the reduced frequency increases, with $\dot{C}_v^*$ becoming more negative with k. Nonetheless, at higher mean angles of attack, even though $\dot{C}_v^*$ is still negative, its value is smaller in magnitude. As α^* increases, the behavior of the time derivative of the strength of the leading-edge vortex becomes more similar to that observed in the linear region but in the negative semi-plane.

Fig. A.1b shows the effect of the reduced frequency on $\dot{C}_v^*$ for an airfoil plunging at different mean angles of attack with an amplitude of $H = 0.2$. In this case, the rate of change of the strength of the leading-edge vortex is positive and increases exponentially with k when oscillating at angles of attack in the linear region of the steady lift curve, reaching higher $\dot{C}_v^*$ as α^* increases. At these angles of attack, the rate of change of the strength of the

leading-edge vortex is an order of magnitude higher than that obtained for a pitching airfoil. However, as the mean angle of attack approaches the nonlinear region ($\alpha^* = 10°$), a sudden increase in $\dot{C}_v^*$ is observed at high reduced frequencies. This behavior is consistent throughout the nonlinear pre-stall region ($10° \leq \alpha^* \leq 14°$), with the rapid rise in $\dot{C}_v^*$ occurring at lower reduced frequencies as the mean angle of attack increases. The trend is reversed when plunging past the stall angle ($\alpha^* \geq 16°$). The rate of change of the strength of the leading-edge vortex starts off as negative and decreases with k, until it reaches a given reduced frequency where it abruptly switches signs, becoming positive and growing as k increases.

Examining Figures A.1a and A.1b, one can observe $\dot{C}_v^*$ being an order of magnitude higher for a plunging airfoil when compared to a pitching airfoil. This difference implies the plunging motion has a higher capacity to affect $\dot{C}_v^*$ and, consequently, modify the average dynamics of the lift force than the pitching motion. At the same time, both figures show positive values of $\dot{C}_v^*$ in the linear region of the steady lift curve and the section of negative curvature, and negative values of $\dot{C}_v^*$ when the curvature is positive.

A.2 Effect of the mean angle of attack

Fig. A.2a plots the time-derivative of the strength of the leading-edge vortex as a function of the mean angle of attack α^* for different pitching amplitudes A_α. At low mean angles of attack, $\dot{C}_v^*$ is positive and increases exponentially with α^*. As the mean angle of attack enters the nonlinear region of the stall regime ($10° \leq \alpha^* \leq 16°$), there is an abrupt increment in the time-derivative of the vortex strength, with the parabola reaching its maximum value when pitching at mean angles of attack close to the stall angle. In the post-stall regime, $\dot{C}_v^*$ decreases with α^*, crossing the zero line and becoming negative. The rate of change of the leading-edge vortex reaches a minimum value when the airfoil oscillates between the peak and the trough of the steady lift curve, after which $\dot{C}_v^*$ increases asymptotically

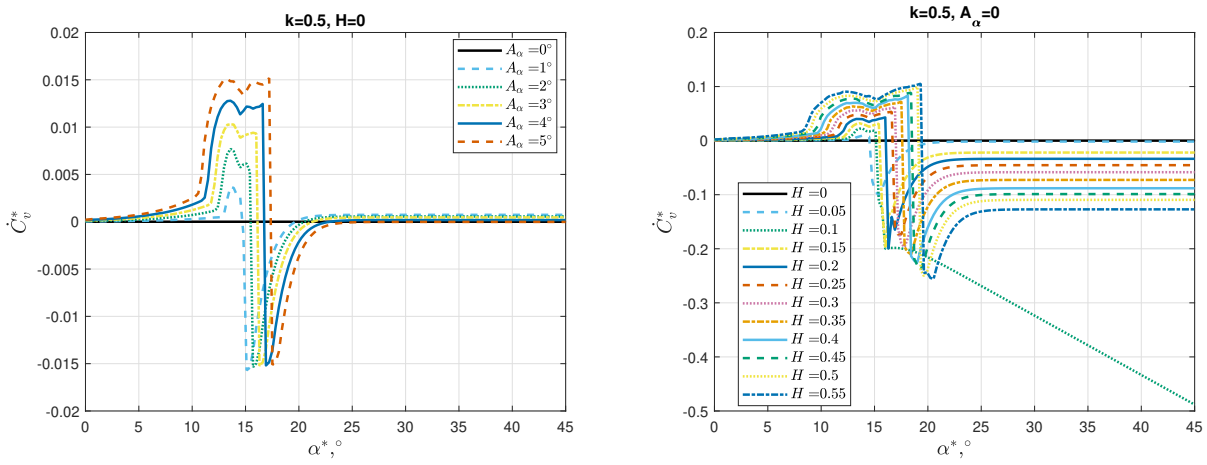

(a) Pitching airfoil.

(b) Plunging airfoil.

Figure A.2: Effect of the angle of attack α^* on the time-derivative of the vortex strength $\dot{C}_v^*$ on a NACA 0012 airfoil oscillating at a reduced frequency of $k = 0.5$, $Re = 500,000$, and $M = 0.3$ for different (a) pitching amplitudes A_α and (b) plunging amplitudes H.

towards zero. This trend, consistent with Fig. A.1a, is observed for all simulated amplitudes. Nonetheless, even though the maximum time-derivative of the strength of the leading-edge vortex is always obtained at the same mean angle of attack of $\alpha^* \approx 12°$, the range of α^* at which the maximum $\dot{C}_v^*$ is attained increases with the pitching amplitude as well as its value. In contrast, the minimum value of $\dot{C}_v^*$ is the same for all pitching amplitudes, but as A_α increases, it occurs at a higher mean angle of attack.

Similarly, Fig. A.2b plots the time-derivative of the strength of the leading-edge vortex as a function of the mean angle of attack α^* for different plunging amplitudes H. The trend is similar to that observed in Fig. A.2a. A slow increment in $\dot{C}_v^*$ in the linear region as the mean angle of attack grows and an abrupt parabolic surge when oscillating close to the stall angle with a sudden decrease to negative values. Nonetheless, after reaching a minimum when plunging at a mean angle of attack close to the trough, $\dot{C}_v^*$ tends asymptotically towards a negative value, instead of the zero limit observed for the pitching motion. Even though the maximum rate of change of the strength of the leading-edge vortex occurs when plunging at an angle of attack close to the stall angle, the actual α^* at which this maximum happens

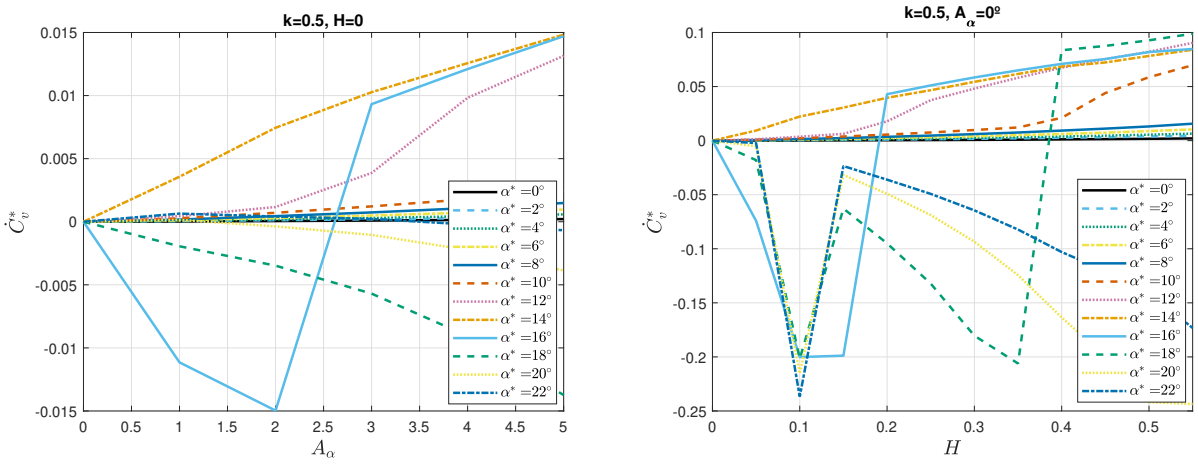

(a) Pitching airfoil.

(b) Plunging airfoil.

Figure A.3: Effect of the (a) pitching amplitude A_α and (b) plunging amplitude H on the time-derivative of the vortex strength $\dot{C}_v^*$ for different mean angles of attack α^* and a reduced frequency of $k = 0.5$ in a NACA 0012 airfoil at $Re = 500,000$ and $M = 0.3$.

increases slightly as the plunging amplitude grows. Similarly, the maximum value of $\dot{C}_v^*$ heightens with H, as well as its minimum value. The minimum rate of change is displaced towards higher angles of attack as the plunging amplitude increases. Fig. A.2b presents a diverging $\dot{C}_v^*$ for $H = 0.1$, which may be attributed to numerical errors.

A.3 Effect of the amplitude of oscillation

Lastly, Fig. A.3a illustrates the effect of the pitching amplitude A_α on the time-derivative of the vortex strength for different mean angles of attack. At low α^*, $\dot{C}_v^*$ is positive and increases exponentially with A_α, reaching higher values as the mean angle of attack increases. Nonetheless, the rate of change of the strength of the leading-edge vortex becomes an order of magnitude higher and presents a more linear trend when pitching at mean angles of attack close to the stall angle. The trend is reversed in the post-stall regime. When the airfoil pitches at a mean angle of attack close to the trough of the steady lift curve ($\alpha^* = 16°$), $\dot{C}_v^*$ is negative and decreases with the pitching amplitude, until at a given A_α, where the

time-derivative abruptly becomes positive and keeps increasing as the pitching amplitude grows. As α^* is further incremented, $\dot{C}_v^*$ decreases with A_α towards more negative values.

Fig. A.3b shows the effect of the plunging amplitude H on the time-derivative of the vortex strength for different mean angles of attack. The same trend is observed as for the pitching airfoil. In this case, however, some of the angles of attack present unintuitive results for a plunging amplitude of $H = 0.1$. As mentioned previously, the results at $H = 0.1$ diverge for angles of attack in the post-stall regime due to numerical errors. Therefore, those points may be neglected.

A.4 Summary of the results

As a summary, one can conclude the following about the rate of change of the strength of the leading-edge vortex:

1. $\dot{C}_v^*$ is an order of magnitude higher when oscillating at mean angles of attack in the stall or post-stall regime when compared to angles of attack in the linear region of the steady lift curve.

2. $\dot{C}_v^*$ is almost an order of magnitude higher for a plunging airfoil when compared to a pitching airfoil.

3. $\dot{C}_v^*$ vs. k: $\dot{C}_v^*$ is positive and increases with the reduced frequency at low mean angles of attack. When pitching close to the stall angle, $\dot{C}_v^*$ reaches a maximum value at a given reduced frequency, whereas in plunging airfoils the rate of change keeps increasing. In both cases, when oscillating in the post-stall regime, $\dot{C}_v^*$ is negative and decreases further with k. Nonetheless, in the limiting case of plunging at the stall angle, $\dot{C}_v^*$ is negative and decreasing until an abrupt upsurge at a given k, where it becomes positive and increasing.

4. $\dot{C}_v^*$ vs. α^*: In both pitching and plunging motions, $\dot{C}_v^*$ increases with the mean angle of attack, reaching a maximum value when oscillating close to the stall angle. In the post-stall regime, $\dot{C}_v^*$ drops, becoming negative and attaining its minimum value when oscillating at the trough of the steady lift curve.

5. $\dot{C}_v^*$ vs. A_α and H: In the pre-stall regime, $\dot{C}_v^*$ is positive and intensifies with the amplitude of oscillation. This trend is reversed after the trough, where $\dot{C}_v^*$ becomes negative and decreasing. Between the peak and the trough of the steady lift curve, $\dot{C}_v^*$ diminishes until it reaches a minimum value at a given amplitude. An abrupt reversal in sign leads to a positive contribution of $\dot{C}_v^*$, which keeps growing with the amplitude.